Iso-electronic compounds and elements under high pressure

John R. Maclean

A thesis submitted in fulfilment of the requirements

for the degree of Doctor of Philosophy

to the

University of Edinburgh

1998

Abstract

High pressure directly affects inter-atomic distances, offering a method of studying inter-atomic potentials, and the differing factors governing structural adoption. Using a combination of angle-dispersive x-ray powder diffraction and total energy quantum mechanical calculations, high pressure phase transitions and structures of iso-electronic materials have been investigated. Synchrotron radiation and image-plate area detectors were used to collect data on high pressure phases of Si, Sb, Bi, PbS, PbSe and PbTe. A new method of extracting information, employing Monte-Carlo techniques from powder diffraction data was developed and employed in some of the structural solutions. Full-potential *ab-initio* total energy calculations have been used to compute electronic and structural properties of experimentally observed phases of CuCl.

From the results of these calculations and experiments, a new high pressure phase of silicon (Si-XII or R8) has been observed, existing between the high pressure metallic β-tin structure and the metastable ambient pressure structure Si-III, known as BC8. The pressure dependence of and transition routes to this, the most complex tetrahedral structure of silicon, and other high pressure phases have been studied.

Calculations were performed on structures adopted by the copper halide compound, CuCl. The results of these calculations agree with previous experimental results, showing the existence of the binary analogue of the BC8 structure observed in Si. Electronic properties of the high pressure phases of CuCl were also computed.

Experiments and calculations performed on the group V elements Sb and Bi show

evidence that a monoclinic structure, obtained by distorting a previously proposed tetragonal structure, is adopted by both under high pressure. Rietveld refinements of a further monoclinic high pressure form of Bi are given, supporting earlier experimental analysis.

Finally, results of experiments are given on the high pressure phases adopted by the group IV-VI lead chalcogenides PbX(X=S,Se,Te), existing between the ambient pressure NaCl-type structure, and the high pressure CsCl-type structure. Conflicting results in earlier work are resolved, and possible reasons why these structures are adopted are also explored.

Declaration

This thesis has been composed by myself and it has not been submitted in any previous application for a degree. The work reported within was executed by me, unless otherwise stated.

John Maclean

March 1998

Acknowledgements

To thank everyone involved in the preparation of this thesis would require a separate chapter in itself. However, I would like to mention the following people, whose courage under fire deserves praise:

Mum and Dad, for their support...especially financially!

Gail, for her love and encouragement

Pete Hatton, for his invaluable help and advice

Jason Crain, for his unbounded enthusiasm and knowledge

Stuart Clark, for knowing almost everything about almost everything!

....and finally, James Hsueh, Michele Warren, Stuart Pawley, Guang-Yu Guo, Bob Cernik, and a whole host of others for sharing their pearls of wisdom over the years.

Contents

Chapter 1

Introduction

One of the most intriguing and studied subjects in solid state physics must be that of phase transitions. Despite the centuries of research afforded to this topic, the mechanisms driving transitions and the states of matter between different phases is still under contention. As well as the more commonly assumed transitions between states of matter, such as that of water (H_2O) from a gaseous state, to a liquid, and then to a solid under increasing pressure or reducing temperature, many other single states of matter contain phase transitions. Magnetic ordering of dipoles in ferro-magnetic materials below a critical temperature, or electrical transitions from metals to insulators beyond a certain nearest-neighbour separation, are just two alternative examples of phase transitions.

Among the many types of phase transitions, structural and electronic transitions in solids has provided strong links between academic research and industrial application in recent years. All materials go through at least one solid-to-solid-type transition under increasing pressure, while almost all undergo a solid-solid transition before melting under high temperature. The mechanisms and conditions for any such transitions play a very important role in determining a materials' suitability in extreme environments, such as those experienced in space.

Modern fabrication techniques of semiconductors typically involve deposition of thin

layers of one material onto another. The electrical junctions created in such materials have been used for many decades in transitors, and other electrical switching devices. Lattice strains between the atomic arrangement of the substrate and the deposited material can have the same effect of high pressure on both materials. Transitions into high pressure phases have been observed to occur in the locality of the boundary between the substrate and the deposited material [1], which can alter the electrical properties of the device enormously.

Upon applying pressure to a stable crystalline lattice, the atomic arrangement will change, according to the ease at which the solid deforms with pressure. This is measured by the compessibility of the solid. Typical compressibilities lie between soft substances, such as caesium at $6.25 \times 10^{-2} \text{kbar}^{-1}$, to something as hard as tungsten, with a compressibility of $3.22 \times 10^{-3} \text{kbar}^{-1}$. The most obvious effect of applied pressure on a crystal is a decrease in the inter-atomic spacing. As a consequence of lattice compression, atomic bonding within a material plays a very important role in the re-arrangement of atoms with increasing pressure. The delicate balance between attractive and repulsive forces existing in any crystal structure dictates structural adoption and transition routes, which can only be obtained from a knowledge of the electronic states.

A knowledge of temperature effects in solids is also vital to certain sectors of industry. One obvious area would be that of metal casting. The temperature at which metals melt must be precisely known, as well as the effects impurities have on the melting temperature, especially when fabricating alloys like hardened steel. Too low a temperature, and the material either does not melt, or the molten substance is too viscous to work with. Conversely, if the temperature is too high, material may be lost through vapours, which may also be hazardous to health. As well as this, the cost of heating bulk materials is very expensive, so overheating would result in excess overheads.

When heat is applied to a solid, the already present thermal motion of the atoms is increased. As the thermal energy rises, the kinetic energy imparted to the ions will

eventually be enough to break and reform bonds between neighbouring ions. New solid crystalline phases are formed in this way, but the scope for structural adoption is limited by the fact that the structure must be flexible enough to allow the ions enough mobility, whilst still retaining a periodic crystalline arrangement. For this reason, only one solid-solid phase transition is usually observed in most elements prior to melting.

In following chapters, high pressure was used instead of temperature to study solid-solid phase changes. High pressures allow greater changes on crystal unit cell volumes (around 10-20%), whereas temperature only causes a volume change of a few percent. Increased thermal motion also hinders crystal structure refinement, making it difficult to accurately locate atomic positions. There is also a limit to the maximum temperature that can be used to study solid-solid phase changes, as the material will eventually melt. Pressure, on the other hand, may be increased as high as the experimental apparatus will allow, which in some cases may be in the megabar region.

Although x-ray and neutron experiments are the most direct way to probe the structure of materials, another method is becoming increasingly popular, which can be used to probe structures under conditions unattainable by current experimental techniques. With the advent of the near exponential increase in computational capabilities over recent years, total energy calculations are proving to be an inexpensive way to probe the structural, electrical and magnetic properties of matter. Previously intractable problems are being solved, using new and more accurate methods of approximation, such as Density Functional Theory and the Local Density Approximation [2]. The sheer processing power of modern computers, both serial and parallel, are also more sympathetic to solutions found through brute-force approaches.

Subjecting materials to extremes of pressure and temperature to study phase stability is expensive, not to mention difficult to achieve, without some form of experimental error or contamination. Successfully winning time on the already over-subscribed central research facilities is also becoming more like a lottery. The themes of proposals are often being massaged to comply with subject classifications which currently gain

the approval of selection committees.

Compared with these economic difficulties, computational experiments are very efficient. Structural adoption, phase stability, electrical properties, magnetic properties, and optical properties can all be probed in a relatively short space of time on many materials. There are still limitations on the type of materials that can be modelled, but the number of these "problem materials" are almost the same, if not less, than those materials that are currently not able to be studied experimentally (due to hazardous reactions, for example).

Ab-initio calculations can also be used to show the importance of inter-atomic potentials on structural adoption. Electron density distributions within solids indicate the degree of ionicity or covalency, which plays an integral part on the type of structures that a material may adopt. In a simplistic way, the structures that materials adopt depends on their crystal classifications, *i.e.* whether they are insulators, semi-conductors, semi-metals or metals. This classification in-turn depends on the electronic configuration of the atomic orbitals in the crystal system.

Insulators and semi-conductors are composed of filled valence electron bands and empty conduction bands separated by an energy gap, which results in localised regions of electrons in real-space. Metals, however, have overlapping energy bands, delocalising the valence electrons throughout the entire crystal. Metallic crystal structures can be viewed as being akin to charged ion spheres in a sea of electrons. Therefore, space-filling criteria can be used to determine which type of structures metallic elements and compounds will adopt, by maximising the amount of space filled by hard spheres. Hence, common metallic crystal structures are based upon face-centred cubic and body-centred cubic arrangements, which have packing fractions of 74% and 68% respectively, for crystals with only one atomic species. Metallic compounds with at least two different atom types tend to adopt structures which are modifications of these basic cubic arrangements.

Amongst semi-conductors and insulators, the types of structures adopted depends

on the bonding configuration. The degree of ionicity and covalency in compounds affects the electron distribution around the ions, and hence determines bond directionality. The different types of structures adopted by iso-electronic compounds and elements, as well as related properties exhibited by each material, have been determined based upon relative amounts of ionicity and covalency by Phillips [3] and Van Vechten [4] for the $A^N B^{8-N}$ compounds, and for the group V elements and IV-VI compounds by Littlewood [5].

Ionic compounds, such as the group I-VII and II-VI materials, have electrons localised around the ion sites. In these compounds, as in the metallic materials, space filling criteria determine the different structures adopted, but relative atomic size also has an effect on the atomic arrangement. Local charge neutrality forces anions to surround cations, which places constraints on structural adoption. Purely covalent elements have appreciable electron densities in the interstitial areas, hence structures which favour bond directionality are adopted. For instance, in the group IV elements (such as Si and Ge) the diamond structure is stable, which allows tetrahedral bonding imposed by the sp^3 hybridisation. The structures adopted by mixed ionic and covalent compounds depend upon a delicate balance between nearest-neighbour contact distance and topology. Rules governing structural adoption in these materials are complicated, but the types of structures which can be adopted have been compiled [6].

The basic distinction between covalent and ionic materials becomes less clear when pressure is applied. The separation between atoms is reduced, which alters the width of electronic energy bands, making band overlap possible. This observation is substantiated by the fact that all materials eventually become conducting under extreme pressures. However, below such pressure, structural adoption is dictated solely by the changing degree of ionicity and covalency in the crystal. Space-filling also becomes very important under high pressure, even in purely covalent elements. Despite the obvious complexity in determining stable high pressure structures, similarities in solid-solid phase transition sequences can still be seen in iso-electronic materials. This is

to be expected, since increasing pressure on a compound alters the ionic and covalent content of the atomic bond. This is equivalent to stepping through the Periodic Table from, say, a group V element to a group IV-VI compound. Therefore, by studying high pressure polymorphism in iso-electronic materials, an insight into the role that ionicity and covalency has on structural adoption may be gained.

Chapter 2

Experimental techniques

There are a number of ways to examine the structural arrangement of atoms within a crystal structure. These methods may involve long range interactions, allowing the structure of the crystal unit-cell to be studied (x-ray and neutron diffraction), while others can probe the location of nearest and next-nearest neighbours (Extended X-ray Absorption Fine Structure,(EXAFS)). X-ray and neutron diffraction may be used with single-crystal or powdered samples, and with either a fixed or variable wavelength in the case of x-ray diffraction. Each technique has its own merits, but the method used throughout chapters 4, 6 and 7 was x-ray powder diffraction with a fixed wavelength (angle-dispersive mode).

2.1 Angle-dispersive x-ray powder diffraction

The experiments performed in chapters 4, 6 and 7 were all undertaken at pressures ranging between 0kbar and 200kbar. Studying the crystal structures of each sample at such high pressures warranted the use of powder diffraction, as any single-crystal samples would have broken up after going through several structural changes under near-hydrostatic conditions.

X-ray and neutron diffraction experiments rely on the same underlying principle

that incoming radiation of wavelength λ is diffracted by planar layers of atoms in a crystal structure (with inter-layer spacing, d) at an angle θ to the plane. These values may be related by the familiar Bragg's Law for diffraction

$$\lambda = 2dsin(\theta) \tag{2.1}$$

This equation is shown schematically in figure 2.1. For a reflection to be observed, the reflected rays must be re-combined constructively (*i.e.* the extra path-length travelled by the same ray must equal one complete wavelength), which thus implies equation (2.1).
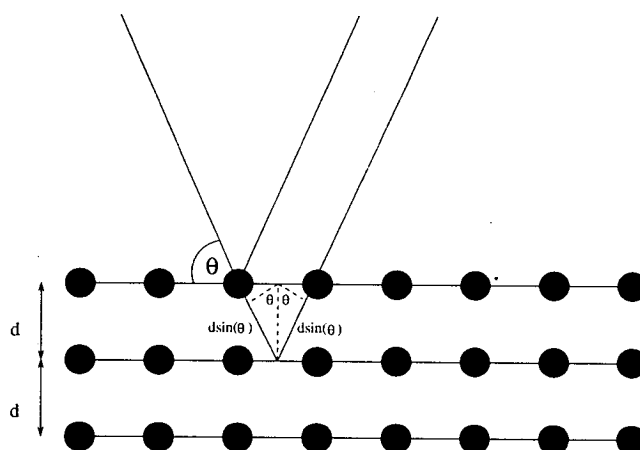
Figure 2.1. Schematic diagram of crystal diffraction. Incoming radiation interferes constructively when the extra distance travelled by the same ray is one complete wavelength.

Bragg's Law may be formulated in another way, which is mathematically more appropriate for the rest of this section. In the von-Laue formulation, the crystal is assumed to be composed of separate objects, placed on the sites **R** of a Bravais lattice,

which can re-radiate incoming radiation in all directions.
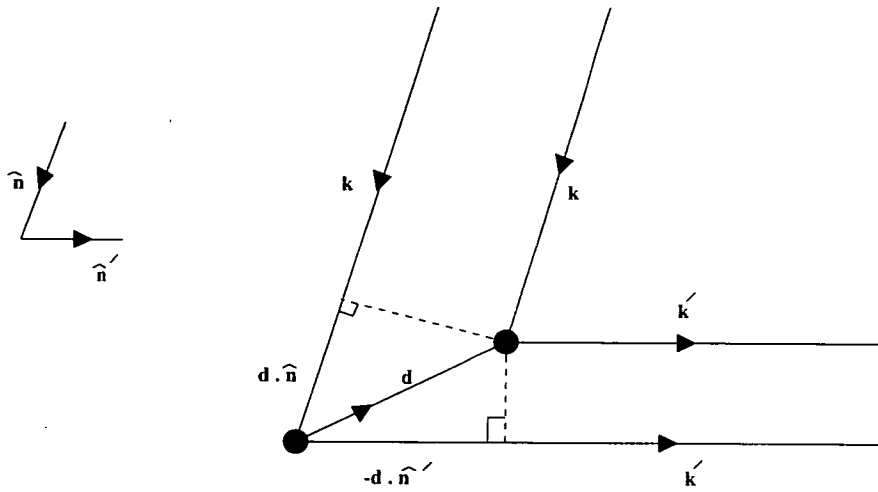
Figure 2.2. Schematic diagram of von Laue diffraction. Incoming radiation, wave vector **k**, interferes constructively when the extra distance travelled by the same ray $(\mathbf{d} \cdot \hat{\mathbf{n}} - \mathbf{d} \cdot \hat{\mathbf{n}}')$ is one complete wavelength.

In order for a scattered intensity to be observed from the crystal in a certain direction and at a certain wavelength, all elastically scattered rays from each object must re-combine constructively. If two scattering objects in the crystal are to satisfy this condition, then from figure 2.2 it can be seen that

$$\mathbf{d} \cdot (\hat{\mathbf{n}} - \hat{\mathbf{n}}') = m\lambda \qquad (2.2)$$

where **d** is the displacement vector between the scattering objects, **n** and **n'** are the direction vectors of the incident and scattered rays respectively, λ is the wavelength and m is an integer. If all objects in the crystal are now considered, the requirement for constructive interference is satisfied if equation 2.2 holds simultaneously for all values of d that are Bravais lattice vectors, *i.e*

$$\mathbf{R} \cdot (\mathbf{k} - \mathbf{k}') = 2\pi m \qquad (2.3)$$

or equivalently,

$$e^{i(\mathbf{k'}-\mathbf{k})\cdot\mathbf{R}} = 1, \tag{2.4}$$

where we have multiplied equation (2.2) throughout by $\frac{2\pi}{\lambda}$ to replace the direction vectors of the incident and scattered rays, $\mathbf{n}$ and $\mathbf{n'}$, by wave vectors $\mathbf{k}$ and $\mathbf{k'}$ respectively. From equation 2.3 it can be seen that, by definition, $\mathbf{k} - \mathbf{k'}$ must equal a reciprocal lattice vector, $\mathbf{G}$ [7]. Thus, the change in wave vector of the incident ray, after being scattered within the crystal, must equal a reciprocal lattice vector to be observed as a reflection.

The incoming radiation may be in the x-ray region of the electromagnetic spectrum (to probe Ångstrom length-scales), or equal to the deBroglie wavelength of high energy neutrons. To examine the various inter-atomic distances within the crystal, the incident wavelength may be altered while keeping the detection source at a fixed angle from the sample (energy-dispersive), or the wavelength may be fixed, and the angle between the sample and detector may be scanned (angle-dispersive). Single-crystal samples may be used in different orientations (or by scanning the wavelength) to collect scattered radiation from different planes of atoms within the crystal, or a powdered sample may be used, which combines all the one-dimensional information from a single-crystal experiment onto a three-dimensional diagram, since the sample crystallites act like small single-crystals orientated randomly. The type of scattering pattern observed from a powder diffraction experiment appears as a set of concentric rings of intensity, centred around the straight-through position of the incident beam (see figure 2.3). These rings are the Debye-Scherrer rings, formed from the cones of diffracted rays from the randomly orientated crystallites in the samples, with semi-angle ϕ. The semi-angle is the actual scattering angle of the reflection, *i.e* it is the angle between the incident beam and the scattered beam. On inspection of figure 2.3, it can be seen that $\phi = 2\theta$. Hence, positions of reflections are often quoted in terms of 2θ, in reference to Bragg's

Law.
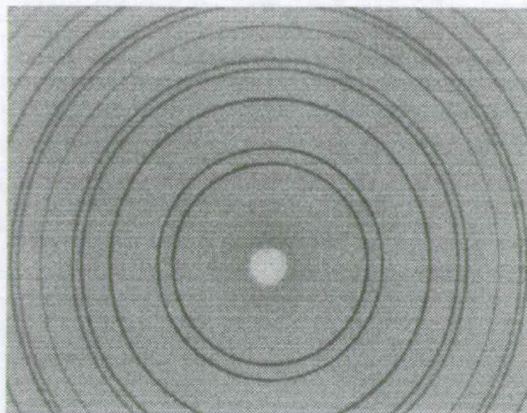
Figure 2.3. An example of the type of diffraction pattern obtained from a powder sample. PbS at ambient pressure was used in this case, and the pattern was recorded on an image-plate.

The intensity of each reflection depends on both the geometrical and physical arrangement of the diffraction experiment. The position and multiplicity of the reflection is given by the symmetry and shape of the crystal unit-cell, while the intensity is a fraction of the primary beam's intensity, scaled by a number of factors. The basic form of this intensity variation [8] is given by

$$I = I_p \times \left(\frac{e^2}{4\pi\epsilon_o m c^2} \right)^2 P(2\theta_B)|F|^2, \tag{2.5}$$

where I_p is the intensity of the incident beam, F is the structure factor, θ_B is the Bragg scattering angle, and $P(2\theta_B)$ is the polarisation factor (see section 3.1.2), which is a function of the scattering angle.

2.1.1 Synchrotron radiation

In proceeding chapters, the x-ray source used was synchrotron radiation, produced by the storage ring at Daresbury Laboratories. Synchrotron radiation has the advantage over conventional x-ray tubes of greatly increased intensities and tuneable wavelengths,

from between 0.3-2.5Å . Both these advantages are essential for accurate crystalline phase determination in single-crystal diffraction, but especially with powder diffraction, where small sample size reduces the intensity of reflections.

Synchrotron radiation is the "waste" radiation emitted by particle accelerators. All charged particles emit radiation when they are accelerated, such as the electrons and positrons in circular particle accelerators and storage rings. When electrons are held in a storage ring (by an inertial or centripetal force), orbiting at a velocity v, the synchrotron radiation produced is in a cone of angle γ^{-1} in the same plane as the storage ring, where the energy of the electrons are given as

$$\gamma m_o c^2, \tag{2.6}$$

where m_o is the rest mass of the electron, and c is the speed of light. The polarisation of the beam is also parallel to the plane of the storage ring. A schematic diagram showing the production of synchrotron radiation by an electron storage ring is given below in figure 2.4 [9].

The Daresbury particle accelerator, called NINA, was recommissioned as the world's first dedicated synchrotron radiation source in the 1970's, using beam ports tangential to the electron storage ring to skim off the x-rays, directing them into experiment hutches. Bending magnets are used to keep the electrons orbiting around the ring, and super-conducting wiggler magnets are used to increase the intensity and spectral range by locally changing the direction of the electron beam in alternate directions so as to

produce no net change in the direction of the electron path.
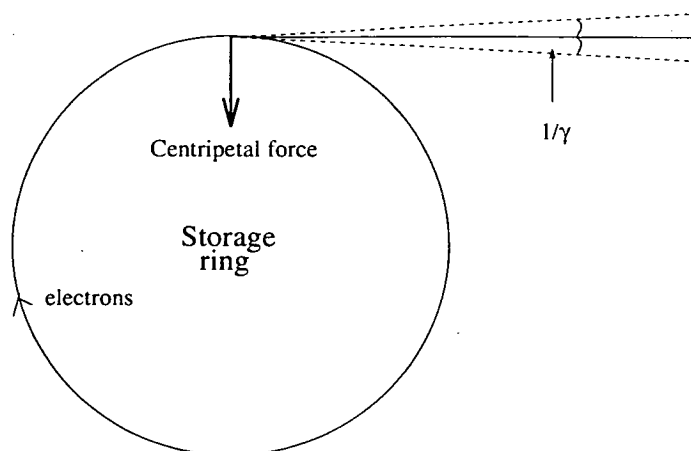
Figure 2.4. A schematic diagram of how synchrotron radiation is produced from an electron storage ring.

2.1.2 Image plate detection

The applicability of x-ray powder diffraction is severely limited by the very small sample volumes, giving weak intensities and poor powder averages. Energy-dispersive techniques, which allow the incident wavelength to be varied, improve the powder averaging of the sample, and hence boost reflection intensities. However, the intensities obtained are not as reliable as those obtained from powder diffraction for use in Rietveld refinement methods to extract crystal structure information (see section 3.1.2), due to relatively low resolutions and highly featured backgrounds. Angle-dispersive methods offer diffraction patterns suitable for structure solution and refinement, so the advent of imaging plate (IP) methods [10] greatly improved the accuracy of powder pattern data analysis. Throughout chapters 4, 6 and 7, an IP system installed at the Daresbury Laboratory synchrotron radiation source was used [11] to collect x-ray angle-dispersive powder diffraction data from samples at high pressure and room temperature.

A schematic diagram of the experimental arrangement on station 9.1 at Daresbury

is shown below.
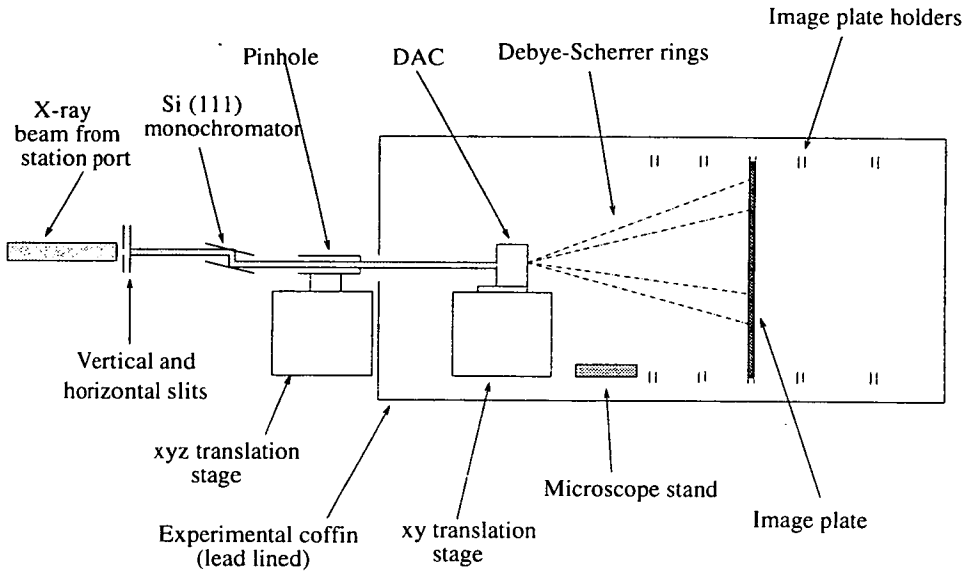
Figure 2.5. Experimental apparatus used at Daresbury to collect x-ray angle-dispersive powder diffraction data.

The white x-ray beam from a 5T super-conducting wiggler is first collimated to a $0.5 \times 0.5 mm^2$ beam, using a set of vertical and horizontal tungsten-carbide slits. A wavelength between 0.42-0.75Å is selected by the water-cooled channel-cut Si(111) monochromator. A platinum and tungsten pinhole is then used to reduce the size of the beam to a few hundred microns in diameter, which then enters the "coffin", which houses the sample being studied. Platinum is used in the pinhole because it has a high atomic number, is extremely dense, and since the K-absorption edge of tungsten is at 0.15817Å , it significantly reduces the $\frac{\lambda}{3}$ harmonic in the incident beam. The experimental coffin has a lead panel where the beam enters, to absorb any diffraction lines from the platinum pinhole, and is covered in lead-lined rubber to stop any scattered x-rays from the experimental hutch being recorded on the image-plate. The sample is held in a diamond anvil cell (DAC), of the types described in section 2.3.1, and the resulting scattered x-rays from the sample are collected on the image-plate as Debye-Scherrer rings, held at a fixed distance from the DAC.

The distance between the DAC and the image-plate may be altered before each experiment by moving the plate into different slots cut into the coffin. The distance between each slot is known exactly, having been precision-cut, but the distance between the DAC and the image-plate may vary, depending on where the sample is within the DAC. Several methods may be employed to calculate the distance between the sample and the image-plate. The methods chosen in proceeding chapters use the fact that the distance between the different slots in the hutch were known accurately. In both methods, data was collected from a single sample in the same environment at two different distances (normally at the closest and a further distance, to increase the angular divergence). The position of corresponding diffraction peaks on the image-plate were then noted, and used in each method. In the first method, the distance from the sample to the image-plate was found from similar triangles. If the distance between the two slots used is Δ, and the position of each diffraction peak on the image-plate from the straight-through position are y_1 and y_2 respectively, then the tangent of each angle must be equal.

$$tan(\theta) = \frac{y_1}{d} = \frac{y_2}{d + \Delta}, 5 \tag{2.7}$$

which may be re-expressed as a ratio of peak position,

$$\Rightarrow \frac{y_2}{y_1} = \frac{d + \Delta}{d}, \tag{2.8}$$

or in terms of the sample-to-plate distance,

$$\Rightarrow d = \frac{\Delta}{\left(\frac{y_2}{y_1} - 1\right)}. \tag{2.9}$$

Hence, by calculating the distance d for each set of peaks i, the sample-to-plate distance may be calculated as being

$$\bar{d} \pm \sigma = \sum_{i}^{N} \frac{d_i}{N} \pm \sigma, \tag{2.10}$$

where N is the number of corresponding sets of peaks, and

$$\sigma = \sqrt{\sum_{i}^{N} \frac{(\bar{d} - d_i)^2}{N - 1}} \tag{2.11}$$

is the standard deviation from the mean distance.

This method is simple, and gives an immediate indication if an incorrect set of peaks was used, from a variation of the ratios in equation 2.8. However, this method tends to give large errors, caused by slight errors in the calculation of peak positions, which are then compounded in the averaging process.

A more accurate method is to use the whole set of corresponding peaks to determine the sample-to-plate distance, instead of each individual set. In this method, the value of θ in equation 2.7 is calculated for each peak, and the difference between each value of θ for each set i is computed, $\Delta\theta_i$. This difference should ideally be zero, so the optimal sample-to-plate distance is evaluated by minimising this difference, using a simple interval-halving algorithm. In this algorithm, a region is defined by calculating the variance of each $\Delta\theta_i$ from zero for three different sample-to-plate distances d_j, where $j = 1, 2, 3$. The distances d_j are chosen in ascending order, so that the starting region is found when

$$\nu_1 > \nu_2 < \nu_3, \tag{2.12}$$

where ν_j is the variance for each distance j. The intervals are then halved, and a solution searched for, using the criteria of 2.12, until the variance reaches a pre-determined cut-off limit. Thus, the sample-to-plate distance is then

$$d_2 \pm \sigma, \tag{2.13}$$

where the standard deviation is given by

$$\sigma = \sqrt{\frac{\nu_2}{N-1}}, \qquad (2.14)$$

and N is the number of sets of corresponding peaks. This method gives a more accurate answer for the sample-to-plate distance, and a more reliable error. The first method is still used, however, to determine the correspondence between each set of peaks.

The powder pattern is recorded on an image-plate. This is an area detector, which allows a significant amount of the Debye-Scherrer cones to be sampled, increasing the intensity of each contributing powder reflection, and reducing the effect of preferred orientation in the sample (see section 3.1.2). The image-plate is approximately the size of an A4 sheet of paper (200×250mm), with a Kodak Storage Phosphor Screen (BaFBr:Eu phosphors) bonded onto a flat aluminium plate. The phosphor screen captures incident x-rays, exciting the electrons into a higher energy state. To recover the image, the plate is passed through a Molecular Dynamics 400A PhosphorImager, which scans the plate horizontally by a He-Ne laser. The energy from the laser is sufficient to excite the electrons into a further energy state, which can decay by emitting light. The emitted light is collected by a fibre-optic bundle and detected by a photo-multiplier tube. The plate is then dragged across, and the process is repeated. The whole image is stored in an 11Mbyte data file containing approximately 2800×2000 pixels (in the highest resolution each pixel is approximately 88μm in length). A typical image recorded on an image-plate is shown in figure 2.3.

Once the powder pattern has been collected and stored on the two-dimensional image-plate, it must be converted to the conventional one-dimensional powder pattern diagrams, showing scattering angle 2θ against intensity. This allows structure solution and refinement using standard data analysis packages. The computer program used to accomplish this was called PLATYPUS [12]. It was written and tested for the experimental station at Daresbury Laboratories. The program converts the position

of a pixel on the plate to the Bragg angle θ using standard geometrical relations. If the experimental arrangement is described by a series of points in space, with respect to an origin in the plane of the image plate, the position of a powder sample can be $S = (x_0, y_0, z_0)$. If the incident x-ray beam strikes the image-plate without having it's direction altered, the position on the image plate will be $C = (x_c, y_c, 0)$. However, if the incident x-ray beam is scattered from the sample, it then strikes the image plate at position $P = (x_p, y_p, 0)$. This arrangement is shown in Figure 2.6
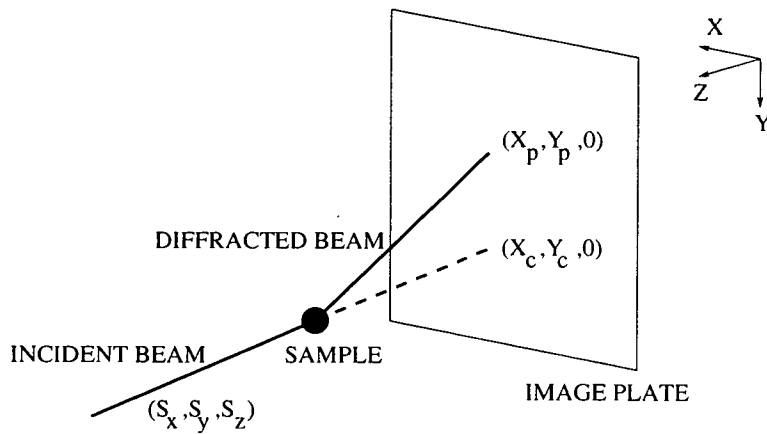
Figure 2.6. The position of the sample, the un-diffracted and diffracted beams are shown on this diagram, along with their coordinates in space with respect to an origin, whose xy plane is parallel to the image plate.

The Bragg angle can then be obtained from the dot product of the direction vectors from the sample to the positions on the image plate, as described above.

$$cos(2\theta) = \frac{\vec{SC} \cdot \vec{SP}}{|\vec{SC}||\vec{SP}|},$$
(2.15)

which can be expanded into each component as

$$cos(2\theta) = \frac{(x_c - x_0, y_c - y_0, -z_0)(x_p - x_0, y_p - y_0, -z_0)}{|(x_c - x_0, y_c - y_0, -z_0)||(x_p - x_0, y_p - y_0, -z_0)|}.$$
(2.16)

The program accounts for the plate being tilted with respect to the perpendicular direction to the incident beam, then integrates around each Debye-Scherrer ring by re-binning the data into approximately 160 sectors. The pixels within each sector are re-binned in terms of the distance in pixels from the (x_c, y_c) point on the plate. This reduces the amount of memory required to store a pattern by a factor of 14.

2.2 Composition of powder diffraction patterns

The position of scattered x-rays, or reflections, is determined solely by the size and shape of the unit-cell. However, the intensity of each reflection is a combination of many factors. Structural factors which contribute to the intensity of each reflection peak are such things as the position of each atom, the number of atoms, the species of atoms in the unit-cell, and the number and type of defects within the crystalline sample. External effects such as temperature and anisotropic pressure gradients applied to the sample also broaden the shape of each reflection peak, hence altering the overall peak intensity (these effects are discussed in section 3.1). Finally, the experimental arrangement also affects peak intensity, with collimator size and polarisation being major factors to consider (see section 3.1.2). In this section, only structural effects on the intensity of each reflection will be considered.

2.2.1 Structure factor and geometric form factor

From equation 2.4, the condition for an observable scattered reflection was developed. This can also be used when evaluating the intensity of such an allowed reflection. The scattered intensity can be described as [13] $I(\mathbf{G}) \alpha |F(\mathbf{G})|^2$, where

$$F(\mathbf{G}) = \sum_{j=1}^{N} f_j(\mathbf{G}) e^{i(\mathbf{G} \cdot \mathbf{d}_j)} \qquad (2.17)$$

$f_j(\mathbf{G})$ is the scattering strength of ion j at reciprocal lattice vector $\mathbf{G}$, and the sum is over every ion in the unit-cell at positions $\mathbf{d}_j$. Equation 2.17 is known as the *structure*

factor for the crystal.

In the case of x-ray diffraction, the scattering strength $f(\mathbf{G})$ depends on the charge density around each atom, i. This will, to a good approximation, take the form of an exponential decay as the distance from the centre of the atom increases. Then, $f(\mathbf{G})$ in equation 2.17 may be re-expressed as

$$f_i(\mathbf{G}) = -\frac{1}{e} \int \rho(\mathbf{r} - \mathbf{r}_i) e^{i\mathbf{G}\cdot(\mathbf{r}-\mathbf{r}_i)} d\mathbf{r}, \qquad (2.18)$$

where f is called the *form factor* and $\rho(\mathbf{r})$ is the electron charge density. To a first approximation, the charge density around atoms in a crystal structure will be the same as for a single isolated atom (since most scattering will be due to the relatively large proportion of the electron cloud centred around the atoms, and not by the few electrons contributing to bonding in interstitial regions). Thus, computed form factors for each element can be used in calculations of diffraction patterns. If thermal agitation of the atoms and electrons are considered in the crystal, the total structure factor for x-ray scattering can be shown to be

$$\sum_i -f_i(\mathbf{G}).e^{(-\frac{1}{4}G^2 <u_i^2>)}.e^{(i\mathbf{G}\cdot\mathbf{r}_i)}, \qquad (2.19)$$

where $<u_i^2>$ is the mean square displacement of each atom from it's mean (or equilibrium) position, and the sum is over each atom in the crystal. The extra exponential term in the middle of equation 2.19 is called the *Debye-Waller factor*, whose effect is inversely proportional to the temperature of the crystal.

2.2.2 Effect of crystal symmetry on the diffraction pattern

When crystalline solids undergo solid-solid phase transitions, the new phase may be a complete change from the original structure, brought about by a massive re-organisation of atoms. However, some transitions only involve limited bond-breaking and reforming, resulting in new structures which are modifications of the original. Symmetry breaking

can be seen under pressure in many materials, such as the transition in silicon from body-centred cubic Si-III to rhombohedral Si-XII, which is described in more detail in Chapter 4. In transitions such as these, the diffraction pattern adopts new reflections, as well as retaining those from the higher symmetry structure. These are due to an increase in the number of degrees of freedom associated with a drop in symmetry.

Another characteristic of this type of transition in the diffraction pattern is the splitting of previously degenerate reflections. Using orthogonal unit-cells for simplicity, this can be shown by taking the real lattice vectors

$$\mathbf{r}_i = a_i \hat{\mathbf{x}}_i, \tag{2.20}$$

where the $\mathbf{r}_i$ are the lattice vectors with $i = 1, 2, 3$, a_i are the unit-cell lengths (which are all equal in the case of a cubic cell), and the $\hat{\mathbf{x}}_i$ are direction vectors in real space. The reciprocal lattice vectors, $\mathbf{g}_i$ of this cell are just

$$\mathbf{g}_i = \frac{2\pi}{a_i} \hat{\mathbf{x}}_i \tag{2.21}$$

Also, any combination of the reciprocal lattice vectors is also valid, such as

$$\mathbf{G} = h\mathbf{g}_1 + k\mathbf{g}_2 + l\mathbf{g}_3, \tag{2.22}$$

where h, k, l are all integers, and are just the Miller Indices. Then, the inter-planar distance, d, in the real space lattice is given by $\frac{2\pi}{|k|}$, which is

$$d = \frac{1}{\sqrt{(\frac{h}{x_1})^2 + (\frac{k}{x_2})^2 + (\frac{l}{x_3})^2}} \tag{2.23}$$

As can be seen from equation 2.20, with cubic symmetry (*i.e* with $a_1 = a_2 = a_3 = a$, the $(h00)$, $(0h0)$ and $(00h)$-type reflections are all degenerate. With a tetragonal system, the $(h00)$ and $(0h0)$ reflections will be doublets, with the $(00h)$ reflection becoming a singlet, since the c-axis has a different length to the a and b-axes, which

are equal. With a further decrease in symmetry to orthorhombic, all three reflections become singlets, since all unit-cells lengths are different. Also, in reflections of the type (hkl), the (hkl) and (khl) reflections will be doublet in cubic and tetragonal cells, but in orthorhombic symmetry, all (hkl) reflections will be singlet (unless there are accidental absences, where the d-spacing between planes are "accidentally" the same). These situations are shown below in figure 2.7.
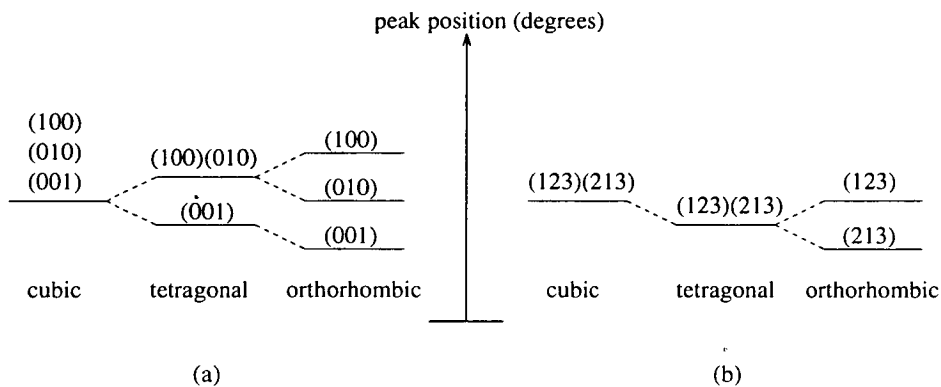
Figure 2.7. In (a) the triply-degenerate (100), (010) and (001) reflections in the cubic cell become doublets in the tetragonal cell, and singlets in the orthorhombic cell. In (b) the doubly-degenerate (123) and (213) reflections for cubic and tetragonal symmetry become singlets in the orthorhombic cell.

2.3   High pressure experiments

In order to study structural phase transitions, two external factors may be altered, *viz.* temperature and pressure. The effect of increasing temperature on a crystalline solid will force thermal motion on the constituent atoms, the magnitude of which will depend on the atoms involved. Conversely, decreasing the temperature will quench thermal motions out. These changes on the thermal motions may force changes in atomic configuration in order to minimise the equilibrium energy of the crystal. The same is true of pressure, although instead of thermal motions governing the phase transitions, co-ordination number and density become the factors which alter the total

energy of the crystal. Modern techniques allow megabar pressures to be reached using shock-compression (dynamic) experiments, and pressures up to approximately 300kbar using diamond anvil cells (static) can also be obtained.

Static high pressure experiments, using diamond anvil cells were used throughout chapters 4, 6 and 7 to examine structural phase changes in the crystalline elements and compounds studied.

2.3.1 Diamond-anvil cells

To exert the high pressures required on the powder samples used, diamond anvil cells (DACs) were employed. Many different types of DAC have been constructed over the years [14], to be used in different areas of experimentation, ranging from Raman spectroscopy to neutron diffraction. The two types of cell used throughout chapters 4, 6, and 7 were the Merrill-Basset cell [15], and the Diacell DXR-5, which is derived from the Merrill-Bassett cell, but with the shape of the unsupported beryllium surface following that of Shiferl [16], and Keller and Holzapfel [17].

Both the DACs used follow the same principle, as do all the others, whereby pressure is transmitted by the compression of the sample between two diamonds, mounted on opposite faces of the cell (see figure 2.8).
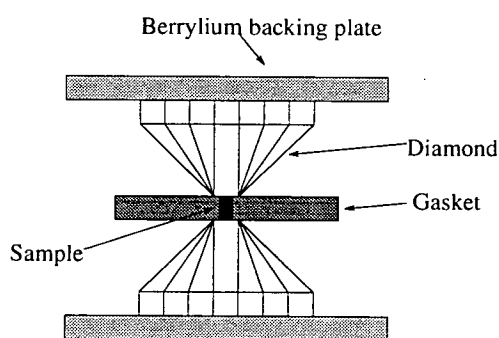
Figure 2.8. A schematic view of the action of all diamond anvil cells(DAC). Pressure is obtained by compressing the sample between the two diamonds shown. Hydrostatic conditions are achieved by mixing the sample in the gasket with a pressure-transmitting fluid.

The sample under investigation is normally either composed of a fine powder (approximately 4μm in diameter) which is used directly from the supplier, or is ground up from larger (sugar-cube sized) chunks of material. The sample is then placed in a gasket (a small hole, normally between 50μm and 100μm in diameter, punched in a piece of metal, which is normally tungsten or stainless-steel). Along with the sample, a ruby chip is added for pressure measurement, and some pressure-transmitting fluid to promote hydrostatic pressure conditions. These additional elements will be explained in more detail later in this section. The Merrill-Bassett cell is capable of exerting a maximum pressure of 100kbar, while the Diacell DXR-5 is capable of about 200kbar. These limits are inherent in the cell construction, but the maximum pressure achievable is also affected by the size of the diamond faces on the sample (usually 3mm), and also by the components of stress on the metal gasket. If, for example, the two diamond faces are not aligned perfectly parallel to each other, or if the action of high pressure alters that alignment, the gasket hole (ideally perfectly circular to eliminate any anisotropic pressure gradients) will tend to become elliptical. This ellipticity will become exaggerated by pressure, resulting in rupture of the gasket hole, preventing any further pressure increase.

The basic elements of the design of the Merrill-Bassett and the Diacell DXR-5 cell

are shown below [14, 18].
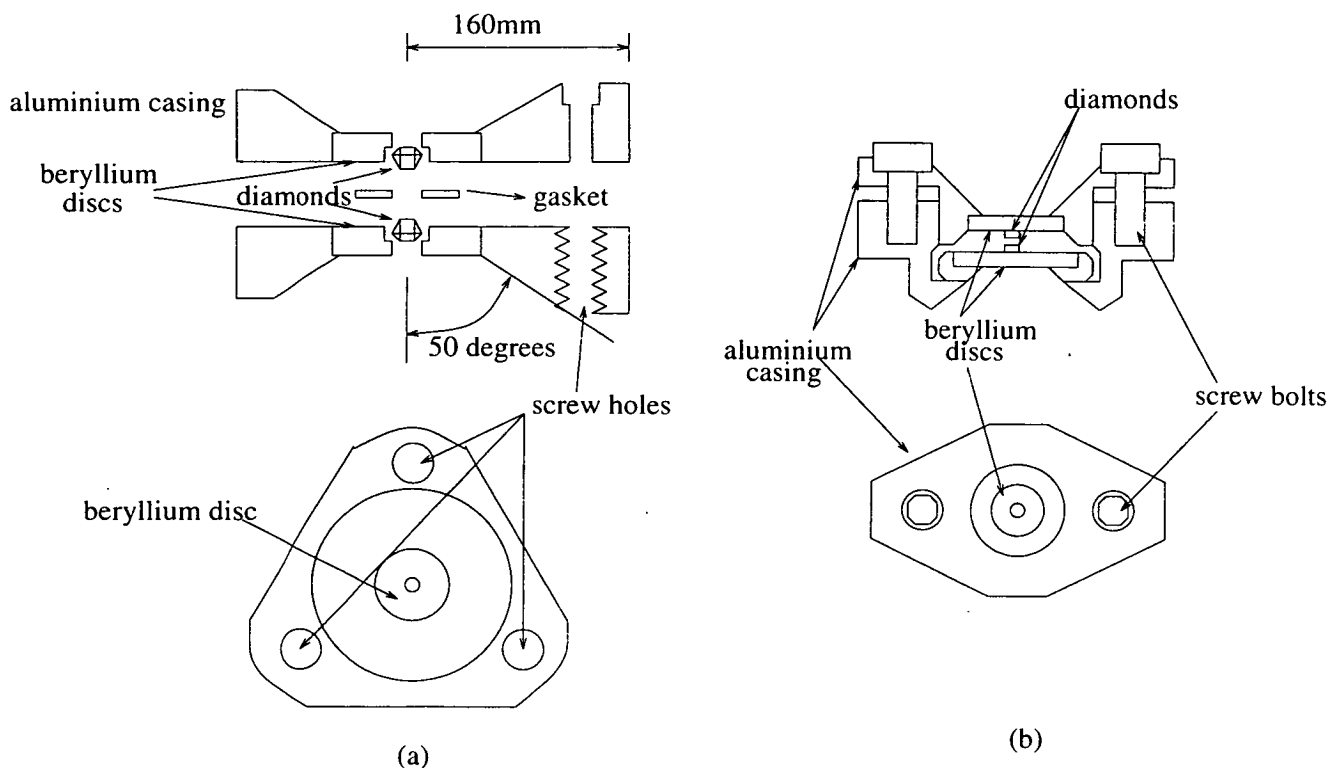
Figure 2.9. The basic design of the (a) Merrill-Bassett cell and (b) Diacell DXR-5 cell are shown (not to scale). The entrance angle (top side) of the DXR is 45°, and on exit (bottom side) it is 50° , as in the Merrill-Bassett cell.

Both cells are almost the same, except for the location of the screws which are tightened in order to increase pressure. The diamonds are mounted on beryllium backing plates. Beryllium is used, since its high strength and low compressibility results in a stable support for the diamonds. The diamonds are attached to the backing plates using standard high strength glue. The outer casing of both cells is made from aluminium, used again for strength.

The gasketting of the sample is an important aspect of the high-pressure cell arrangements. Small (50-100μm) holes are either drilled or spark eroded into tungsten or stainless-steel alloys, into which the powder sample, a ruby chip, and a pressure-transmitting fluid (to create hydrostatic pressure conditions within the gasket) is placed. Hydrostatic conditions are favoured as it helps equalise pressure gradients

within the gasket hole, helping to maintain its shape. Liquids or gases may be used as the fluid, but in proceeding chapters a liquid was used. Single-component liquids tend to crystallise at relatively low pressures, but mixtures of liquids can be taken to higher pressures than the freezing pressures of their components. Under the action of high pressure, the viscosity of mixtures increases until a glass is eventually formed. The maximum pressure limits of several fluids have been tested within the pressure ranges exerted by most DACs (up to approximately 200kbar) [19]. At room temperature the most used liquid is a 4:1 mixture of methanol:ethanol, which may be taken up to a pressure of approximately 104kbar before freezing sets in. However, in chapters 4, 6 and 7, a 16:3:1 mixture of methanol:ethanol:water was used [20] to increase this freezing point to about 145kbar at room temperature.

2.3.2 Pressure measurement

Measurement of pressure during a static high pressure experiment may be achieved by observing the reduction in volume of an accepted pressure calibrant, and calculating the resulting pressure change from a derived equation of state. The reduction in volume would be measured by computing the inter-planar spacing using x-rays, for example. Such pressure calibrants exist, and have been calibrated to high pressures [21, 22] (300kbar in the case of NaCl, since NaCl changes structure at 294kbar). Of course, these volume changes are only valid within one structure type and at one specific temperature, but other materials have also been calibrated to measure pressure up to about 2000kbar, such as silver, palladium, molybdenum, copper and aluminium. This method is generally accepted to be accurate to about 2 or 3% within their own pressure regions.

Another reliable method, and one which was used in proceeding chapters, is the ruby pressure gauge. This method uses the fact that the ruby fluorescence band in the red part of the spectrum (about 694nm) shifts linearly in wavelength (or energy) with pressure, up to about 100kbar. Above this pressure, the linear relationship begins

to break down, and the fluorescence line begins to broaden (due to increasingly non-hydrostatic pressure conditions within the DAC), making pressure determination more difficult. The pressure as given by this method is also dependent on the temperature, and the relative mixtures of Cr_2O_3 and Al_2O_3 in the ruby. However, it has been shown [23] that the effect of temperature is negligible between 4 and 360K. When all the systematic errors are compounded, the generally accepted errors on a pressure measurement recorded by the ruby method is about 3% below 100kbar, but the error limits above 100kbar are less well determined.

At the Daresbury SRS a ruby fluorescence method was employed, where a ruby chip loaded with the sample in the DAC was illuminated with laser-light, and the fluorescence measured by a standard spectrometer. The intensities of the fluorescence lines were scanned over wavelength and displayed on a Viglen PC, where the position of the fluorescence lines was converted to a pressure using a pre-programmed software package. The zero-pressure point was first located using a small ruby chip attached to a glass slide, with all subsequent pressures calculated relative to that point. The resolution of the fluorescence peaks could be altered by changing the time taken to scan the wavelength. A smoothing algorithm (interpolation) could also be switched on to locate the position of the ruby fluorescence line more accurately.

Chapter 3

Computational techniques

Once experimental results have been collected, accurate analysis techniques must be employed to extract as much information as possible from the data obtained. Throughout chapters 4,6 and 7, analytical tools used in the extraction of structural information from x-ray powder diffraction experimental data are used, therefore details of the methods used are presented in the first section of this chapter.

In order to complement the knowledge gained from experimental investigations of atomic structures, theoretical calculations are performed. These may be empirical, where experimental results are used as values in theoretical functions, or *ab-initio* (*i.e* all results are obtained from first-principles). Quantum mechanical *ab-initio* calculations were used in chapter 5, hence an overview of the necessary mathematics involved in calculations of this type are given in the second section of this chapter. Routes to solve the many-body problem, as well as important approximations, are also given.

3.1 Powder diffraction analysis

Crystal unit cell parameters and possible spacegroups may be found from collected x-ray diffraction patterns by indexing packages. Atomic positions within the unit cell must then be found, so that a full structural refinement can be obtained. Full details

of each step required for structure determination are given below.

3.1.1 Indexing methods

Strategies to deduce possible spacegroups and unit cell parameters from a powder diffraction pattern are given the name *indexing methods*. Many different techniques, as well as computational methods are employed to arrive at a solution to the problem, but the reliability of any method is determined solely by the accuracy of the data which is input. This remains the crucial factor when trying to assign a crystal structure from powder diffraction data.

Throughout chapters 4,6 and 7, the method of indexing used was supplied by the indexing code DICVOL91 [24, 25, 26]. This was obtained from the CCP14 program suite held at Daresbury Laboratory. The code in its present form allows all crystal systems to be searched, starting from cubic symmetry, gradually lowering through the crystal classes to triclinic symmetry. To facilitate this search, constraints on the maximum and minimum unit cell volume may be specified and also an integer number of molecular units can be defined as an input constraint by giving the molecular weight, along with a density and an error associated with that density. This reduces the computation time considerably when searching through the numerous monoclinic and triclinic crystal systems.

Searching techniques used by indexing programs vary quite considerably. Some methods, like DICVOL91, use brute-force searching (systematically changing the variable lattice parameters until solutions are found). Others search databases containing known crystal structures of elements, compounds and molecules, which are then compared against the material being studied to find similarities [27]. Genetic methods, involving mutations of initially random unit cell parameters until solutions are found, are also employed for orthogonal crystal systems [28]. Since the various techniques are so numerous, the only method outlined in this section will be the one used by DICVOL91.

The indexing program DICVOL91 employs an exhaustive search of all variable cell parameters in direct space. In its present form, all symmetries can be searched (cubic, hexagonal, tetragonal, orthorhombic, monoclinic, and triclinic), starting from the highest symmetry and working down.

Cell parameters are first expressed in Q-space, where

$$Q = 1/d^2, \tag{3.1}$$

and d is the d-spacing of each observed line. In terms of orthogonal crystal systems, with unit cell parameters a, b and c, this gives the relation

$$Q(hkl) = f(a, b, c), \tag{3.2}$$

where

$$f(a, b, c) = \left(\frac{h}{a}\right)^2 + \left(\frac{k}{b}\right)^2 + \left(\frac{l}{c}\right)^2 \tag{3.3}$$

has already been given in general terms in equation 2.22. For monoclinic systems, the following formulation is adopted to be more convenient for the application of the dichotomy procedure (which is the successive division of available phase, or Q-space, detailed in [24])

$$Q(hkl) = f(A, C, \beta) + g(B) \tag{3.4}$$

with

$$f(A, C, \beta) = \left(\frac{h}{A}\right)^2 + \left(\frac{l}{C}\right)^2 - 2hl\cos\left(\frac{\beta}{AC}\right) \tag{3.5}$$

and

$$g(B) = \left(\frac{k}{B}\right)^2, \tag{3.6}$$

where

$$A = a\sin(\beta), B = b, C = c\sin(\beta) \tag{3.7}$$

Triclinic systems are more complex, with a formulation for Q-space in reciprocal-space co-ordinates being required for efficient searching. The equations in this case are omitted for brevity, but can be found in ref. [26].

The variable parameters are scanned in steps of 0.40Å for cell lengths and 5° for cell angles to define maximum and minimum limits on each parameter. Within each region, a calculated powder pattern is generated, each line being represented in Q-space by a region $[Q_-(hkl), Q_+(hkl)]$. If the observed lines Q_i lie within $[Q_-(hkl) - \Delta Q_i, Q_-(hkl) + \Delta Q_i]$, where ΔQ_i is the absolute error of the observed lines, then that region is retained. After the whole parameter space has been searched in this manner, each retained region is then halved, and this whole dichotomy procedure is repeated up to a maximum of seven times. Final cell parameters are then optimised using a least-squares algorithm, and figures of merit are calculated for each predicted solution. The figures of merit used are the de Wolff value, M_N [29], and the Smith & Snyder value, F_N [30]. These values indicate how well the diffraction lines from the calculated structure match the observed diffraction lines.

The most widely used figure of merit is M_N, normally used with $N = 20$, *i.e* 20 observed lines. It is derived from a need for any indexing package to calculate diffraction lines as close as possible to the observed lines, hence minimising the discrepancies between each observed and calculated line. The value M is defined as a ratio of the average discrepancy between observed and calculated lines, and the actual discrepancy associated with each observed line. This may be re-expressed in terms of the Q-values as mentioned in equation 3.1 for each observed line by the equation

$$M_N = \frac{Q_N}{2\bar{\epsilon}N_N},\qquad(3.8)$$

where N_N is the number of different calculated Q values up to Q_N, which is the value for the N_{th} observed and indexed line, and $\bar{\epsilon}$ is the average discrepancy in Q for the N lines.

The other figure of merit used by DICVOL is the value F_N, which is described in more physically understandable terms than the value M_N mentioned above. The value F_N is given as

$$F_N = \frac{1}{|\overline{\Delta 2\theta}|} \frac{N}{N_{poss}}, \tag{3.9}$$

where N_{poss} is the number of possible diffraction lines up to the Nth observed line, $|\overline{\Delta 2\theta}|$ is the average absolute discrepancy between the observed and calculated 2θ values and N is the number of indexed lines. Hence, this value gives a measure of the accuracy of the powder pattern and also a measure of the completeness of the indexed pattern. Also, if all observed lines are indexed by the proposed unit cell, the value F_N simply reduces to the reciprocal of the average discrepancy in 2θ.

Choosing a value for the figures of merit that correspond to likely unit cell solutions is difficult. Through numerous tests conducted by de Wolff [29], it was proposed that a value of $M_N > 10$ would correspond to a possible solution, if the number of un-indexed lines was not more than two, and the number of indexed lines N was 20. If the number of lines is not equal to 20, then the applicability of the value M becomes less reliable, and the value for F_N becomes more appropriate.

3.1.2 Rietveld refinement methods

Accurate extraction of the structural information contained in a powder diffraction pattern is vital. The position of each reflection is defined by the size and shape of the unit cell, while the intensity of each reflection is dependent upon the spacegroup of the structure and the atomic locations within the unit cell. The natural solution to this type of problem is to postulate a model for the sample being examined, simulate the powder diffraction pattern it would produce, and then minimise the difference between the observed and calculated diffraction patterns by refining lattice parameters and atomic positions.

Methods of this sort were first formulated by H. M. Rietveld in 1969, and were applied to neutron powder diffraction patterns [31]. The application of this method quickly spread to accommodate x-ray powder diffraction [32] and is now generally accepted as being the standard method for accurate structural refinement from powder diffraction patterns. There are many different Rietveld codes in circulation, such as DBW [33], and MPROF [34]. The accuracy of many have been tested [35], showing the uniform reliability of each refinement code. All methods are termed *Rietveld refinement methods*, with each one following the same general principles to extract the same information, using slightly different computational techniques.

To prepare the observed diffraction pattern for the Rietveld method, the background intensity must be subtracted from the intensity produced by atomic scattering. Background intensity may have been altered by the amount of amorphisation present in the crystalline phase, or it could be an overall intensity caused by the detection system being used, *e.g* chemical fogging from a photographic plate. If the total observed intensity at point i is Y_i^o, and the background intensity at that same point is B_i^o, then the intensity used in the Rietveld refinement will be

$$y_i^o = Y_i^o - B_i^o \tag{3.10}$$

The background may either be expressed as a known function (if it is uniform, for example), or as an interpolated scheme by choosing specific points in the diffraction pattern.

The form of the calculated intensity from neutron and from x-ray powder diffraction is very similar [36], with only a few extra correction terms being necessary when x-ray diffraction from monochromatic radiation is used. The general expression for the calculated intensity [33] at point i takes the form

$$y_i^c = s \sum_K p_K L_K |F_K|^2 G(\Delta\theta_{iK}) P_K \Gamma(2\theta_i) \tag{3.11}$$

Here, y_i^c is the calculated intensity at the point i, and $K = h, k, l$, are the indices identifying each Bragg reflection. The sum is over all Bragg reflections K contributing to the diffraction pattern at point i. p_K is the multiplicity of each reflection, L_K are the Lorentz and polarisation factors [37], F_K is the structure factor, P_K is a preferred orientation correction, $G(\Delta\theta_{iK}) = G(2\theta_i - 2\theta_K)$ is the reflection profile function, and $\Gamma(2\theta_i)$ is the absorption factor of the sample at the scattering angle 2θ of the ith reflection.

The Lorentz and polarisation factors are combined in the parameter L_K because they are both affected by the experimental conditions. The polarisation factor takes into account the effect of the incident radiation being polarised, *e.g* after being mono-chromatized by reflection from a crystal. The Lorentz factor is a geometrical factor, which is concerned with the effect on intensity when the sample is rotated, *i.e.* the amount of incident and scattered radiation striking a section of a powder sample will depend on the angular velocity [9]. Both the Lorentz and polarisation factors depend on the scattering angle θ, and so will affect the intensity arising from each Bragg reflection K. However, with the experimental arrangement used in proceeding chapters, the sample was stationary while data was collected on the image plate. Therefore, the Lorentz factor was not included in any Rietveld refinements performed on data collected in this thesis.

Due to the polycrystalline nature of a powder sample, crystallites may adopt certain preferred orientations. The method for dealing with this effect on the calculated intensity is to assume a particular preferred direction, and to express the effect on intensity as a functional form for each Bragg reflection. This correction can take on many different forms [38], the theory of which cannot be dealt with in a section of this size. However, a basic form can be expressed for plate-like crystallites which tend to align their normals parallel to the largest pressure gradient within the sample [31]. The correction to the observed intensity can then be expressed as an exponential function

$$P_K = e^{-Z\alpha^2}, \tag{3.12}$$

where α is the acute angle between the scattering vector and the normal to the crystallites, and Z is a refinable preferred orientation parameter.

The choice of reflection profile function G is also varied. In neutron diffraction, a Gaussian profile is normally sufficient to describe the spread of counts around a Bragg reflection.

$$Gauss(\theta_i) = \frac{2\sqrt{ln2}}{H_K\sqrt{\pi}} \times exp[-4ln2(\Delta\theta_{iK})/H_K^2], \tag{3.13}$$

where H_K is the full-width at half-maximum for each Bragg reflection K.

This is not the case with x-ray sources, whose peak profiles tend to have extended tails. Numerous profile functions have been suggested and tested, including Lorentzian(L) curves, modified Lorentzians(ML), intermediate Lorentzians(IL) (mixture of L and ML), pseudo-Voigt (mixture of Gaussian and L), and variable-pseudo-Voigt curves (mixture of Gaussian and ML). The most commonly used is the pseudo-Voigt profile

$$PV = (1 - \eta)Gauss + \eta Lor, \tag{3.14}$$

where η is a mixing parameter ($0 \leq \eta \leq 1$), $Gauss$ is the Gaussian profile given in equation 3.13, and Lor is a Lorentzian profile

$$Lor(\theta_i) = \frac{\sqrt{C_K^L}}{\pi} \times \frac{1}{1 + C_K^L(\Delta\theta_{iK})^2}, \tag{3.15}$$

where

$$C_K^L = \frac{4}{H_K^2} \tag{3.16}$$

An example of the inadequacy of a Gaussian profile to describe a reflection generated

by x-ray diffraction can be seen in figure 3.1. Here, the experimental data shows the (211) reflection of gold at ambient pressure, collected on an image-plate using a synchrotron source, monochromatized at a wavelength of 0.4607Å . The sample used was a piece of gold foil, instead of using a powder, but the results are the same. The dashed line is a Gaussian profile fitted to the data using a least-squares algorithm. As can be seen, the observed peak tails are much wider than those generated by the Gaussian peak profile. Figure 3.2 shows the same experimental data, but with a pseudo-Voigt profile used in the fitting routine (dashed line). An obvious improvement in the correspondence between the experimental and analytical profiles has been obtained by mixing a Gaussian and Lorentzian curve in the ratio 0.64:0.36, instead of just using a pure Gaussian profile.
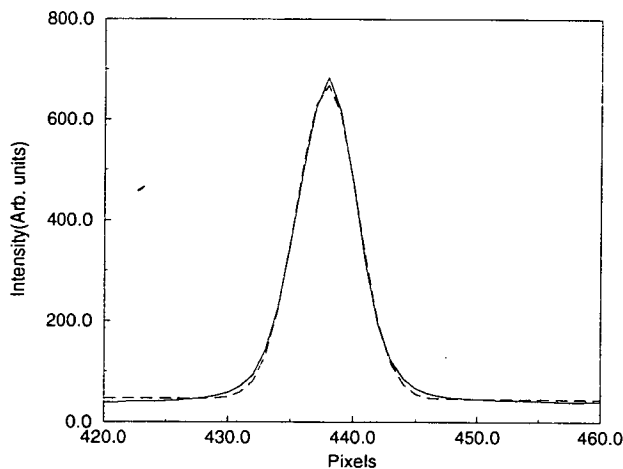
Figure 3.1. Experimental data (solid line) is approximated by a Gaussian profile (dashed line), showing the extended tail, characteristic of x-ray diffraction.
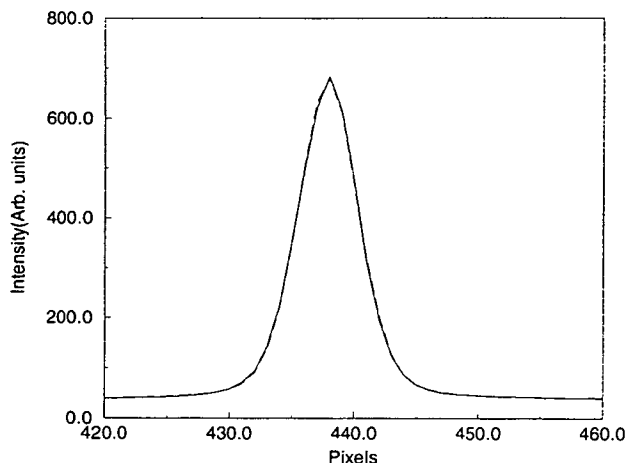
Figure 3.2. Experimental data (solid line) is approximated by a pseudo-Voigt profile (dashed line), producing a much better fit to the data.

The full-width at half-maximum H_K has been shown to be a quadratic function in $tan(\theta)$ [39], which can be expressed as

$$H_K^2 = Utan^2(\theta) + Vtan(\theta) + W, \qquad (3.17)$$

where $U, V,$ and W are refinable parameters, and θ is the diffraction angle. This formulation was derived using data from neutron diffraction experiments, but the parameters $U, V,$ and W are still used to describe the divergence of x-rays from collimators composed of a mosaic of perfect crystalline blocks. The applicability of this functional form for x-ray diffraction has been dealt with by others [40, 41], who preferred to adopt a linear variation in $tan(\theta)$, $i.e$ setting the parameter $U = 0$. However, these investigations were carried out between diffraction angles (θ) of 25° and 110°, so the quadratic term in equation 3.17 may still be required for small θ.

There are different methods to measure the goodness-of-fit between the calculated

and observed profiles. These include the difference between the positions of the calculated and observed Bragg reflections, or between the observed and calculated intensities at each point i in the profile. The most accurate indication of the goodness-of-fit is the weighted profile R-factor R_{wp} (weighted to give equal importance to weaker reflections), which is defined as

$$R_{wp} = 100 \times \sqrt{\frac{\sum\limits_{i=1}^{N} W_i (y_i^o - y_i^c)^2}{\sum\limits_{i=1}^{N} W_i (y_i^o)^2}}, \tag{3.18}$$

where

$$W_i = \frac{1}{\sigma_i^2} \tag{3.19}$$

and σ_i is the standard deviation in the calculated intensity at point i.

In Rietveld refinement methods, the variables which are refinable fall into two categories: (1) structural parameters, and (2) profile parameters. Structural parameters are the unit cell dimensions $a, b, c, \alpha, \beta, \gamma$, the atomic positions, occupancies and isotropic thermal parameters, preferred orientation parameters and global isotropic temperature factors. The profile parameters are the half-width variables U, V, W, and mixing parameters (if PV, variable PV, IL, or ML reflection profiles are assumed).

The two Rietveld refinement methods used throughout chapters 4,6 and 7 were MPROF [34] and DBW [33]. MPROF is mounted at Daresbury Laboratories as part of the powder diffraction program library, and DBW is one of the modules incorporated in the molecular visualiser CERIUS, licenced to run at Edinburgh University and Daresbury Laboratories. Both methods gave refined values which were comparable to one-another.

3.1.3 First-principles structure solution: Monte-Carlo method

The solution of crystal structures from first principles is the goal of any crystallographer. The main difficulty arises from the number of free variables which need to be optimised to give the best solution (the best solution being the one which gives the smallest difference between a comparison of the experimental data and the calculated diffraction patterns). To take an example, imagine a triclinic structure, thought to have ten atoms within the unit cell. Then there would be thirty-six variables to optimise (six unit cell parameters, and 3×10 atomic positional parameters). Even within this simple case, we have already made an assumption, *viz* the number of atoms. If we include this as another free parameter, there are then $6 + (3 \times N_{atoms})$ variables, where N_{atoms} is the number of atoms within the unit cell. However, this is still a linear problem, and with the advent of todays computing power, the problem may still be tractable for many inorganic crystalline structures.

At present, the method of structure solution is split into three parts. The first is to compute the size and shape of the unit cell. This is dealt with by the indexing programs already mentioned in section 3.1.1. The next step is to deduce possible spacegroups from the systematic absence of reflections, using the (h, k, l) labelling of observed reflections predicted by the indexing programs. The final stage is to locate the atom positions, using the observed intensities of each reflection. Density changes calculated from the change in unit cell volume under pressure (assuming a trial structure has been indexed), allow the number of atoms present in the unit cell to be estimated, which may suggest that atoms lie on special positions within the unit cell. Although the possible spacegroups may offer some information for specific atoms, the problem of locating *all* atom positions is by far the most difficult in the structure solution process, especially in triclinic systems.

One method to solve the position of the atoms is to employ a Monte-Carlo (MC) algorithm [42]. The basic idea behind any MC technique is to randomly alter the

variable parameters in the initial model, and to accept this new set if the function being minimised is less than it was previously. If however, the value of the minimising function is greater than it was previously, the trial structure is accepted or rejected based on an exponential probability, whose acceptance rate is controlled as a variable parameter. If all the variable parameters of system i are denoted x_i, then the chain of randomly generated trial structures is

$$x_1, x_2, ..., x_i, x_{i+1}, ..., x_N, \tag{3.20}$$

where N is the total number of MC cycles, and their associated minimising function values are

$$f_1, f_2, ..., f_i, f_{i+1}, ..., f_N, \tag{3.21}$$

where $f_i = f(\{x_i\})$, then trial system x_{i+1} will be accepted if

$$f_{i+1} \leq f_i, \tag{3.22}$$

or if

$$P \leq e^{\frac{-Z}{S}}, \tag{3.23}$$

where $Z = f_{i+1} - f_i$ and P is a randomly generated number.

When the minimising function is expressed in terms of energy, the parameter S in equation 3.23 can be thought of as being akin to temperature (the larger the value for S, the higher the "temperature", hence atoms are able to explore the unit cell space more easily). During the calculation, this parameter may be varied, having the effect of quenching the system to lower temperatures near favourable solutions. This allows the configuration with the lowest energy to be found. These methods have been written and tested, and are termed *simulated annealing* methods [43].

In the MC method which was employed in chapters 4, 6 and 7, the function f being

minimised was the R-factor of the weighted profile. This is the difference between the calculated and experimental diffraction patterns at each point in the pattern, weighted so as to give an equal importance to the weaker peaks (equations 3.18 and 3.19). The scale parameter s was set before the calculation began, to allow at least 60% of trial structures to be accepted (which leads to efficient sampling of the unit cell space) and was not altered throughout the calculation.

The initial form of the MC code was written by members of Prof. Harris's research group at the School of Chemistry at Birmingham University and Dr. Maryjane Tremaine at the University of Central London. Unit cell parameters, obtained from the experimental pattern using an indexing package, must be given as input, along with initial atomic positional parameters. A spacegroup must also be specified, but this may be set to $P1$ if no higher symmetry can be inferred from the data. Within the MC code, the atomic positions are expressed with respect to an orthogonal cell, whose cell edges are set the same to those of the actual unit cell. If the actual unit cell was related to a cell with orthogonal axes, the lengths of each side would obviously depend on the inter-axis angles within the original cell. However, the lengths of the orthogonal cell used are re-scaled to the cell lengths of the actual cell to enable the fractional coordinates in both cells to correspond to each another. These co-ordinates are then transformed to fractional co-ordinates in the actual cell by a transformation matrix. To evaluate the R-factor for each trial structure, the structural parameters are passed on to a modified Rietveld refinement code, DBW [33]. The scale factor for the calculated profile is refined for a preset number of cycles (usually between three and five) and the R-factor is passed back to the main Monte-Carlo program. The randomly generated new trial structure is accepted or rejected based on equations 3.22 and 3.23, then the whole process is repeated.

The code was originally written to solve molecular structures, with whole molecular units being randomly translated, and rotated about a specified pivotal point, within the unit cell [44]. This formulation was inappropriate for the elemental and compound

systems being considered in chapters 4, 6 and 7, so the code was altered. All sections of code dealing with rotations have been removed and a contact distance subroutine added. The contact distance subroutine calculates the distance between the centres of all atoms, and rejects any trial structure which positions atoms closer than the sum of their atomic radii, specified for each atom as inputs. Symmetry equivalent atomic positions can also be considered, generated by the spacegroup of the unit cell, given as symmetry operation matrices in a separate input file. Trial structures are then accepted if the contact distance between atoms is less than half the sum of their radii. This is to allow structures with atoms on special positions (whose symmetry equivalent position is on-top of the position being considered) to be accepted*. Whenever the contact distance subroutine was switched on, the scale parameter, S, was deliberately set to a larger value to allow more structures to be explored, but the atomic radii were then altered to again allow at least 60% of trial structures to be accepted.

The code has been written to compile and run on Silicon Graphics and Hewlett-Packard workstations. Run-times are difficult to estimate, since the workstations used for the work here were shared between other users. However, for a typical calculation involving the random movement of four atoms in three-dimensional space, one-thousand MC cycles were completed in about thirty minutes. By including the contact distance subroutine, this time is considerably reduced, since the program does not call the refinement program when a trial structure is rejected on the grounds of atoms being too close together. The refinement of the scale factor takes the most time to complete (almost 70% of the run-time per iteration). When trial structures are rejected on the basis of the distance between symmetry equivalent atom positions, the time-savings made from not calling the refinement code are lost from the increased number of atom-pair distances the code must check. In some cases, the run-time may be increased by including this routine , when large numbers of atoms are involved. However, the number

---

*This method was used, rather than only considering atoms on inequivalent positions, because it is computationally less intensive.

of impossible trial structures (*i.e* when atoms are located too close to one-another throughout the cell) generated is reduced to almost zero[t] when contact distances are taken into account, and especially when crystal-symmetry is used.

3.2 *Ab-initio* calculations

Ab-initio calculations are those performed from first-principles. All results are obtained without the need for any experimental values to be input (calculations requiring experimental values are called empirical calculations). In chapter 5, *ab-initio* total energy calculations were performed on various crystal structures. When computing total energies, the term *ab-initio* implies quantum mechanical calculations, using information only about the crystal structure (such as crystal system, crystal symmetry, atomic positions, lattice parameters and electronic composition). Any extra inputs required throughout the calculation are all aspects of the approximations used.

To analyse the stability of a crystal structure, it is necessary to compute the total energy required to hold a particular arrangement of atoms together in equilibrium. This is done by solving the Schrödinger equation for all the electrons present in the crystal

$$\sum_{i=1}^{N} \left(-\frac{\hbar^2}{2m} \nabla_i^2 \Psi - Ze^2 \sum_{\mathbf{R}} \frac{1}{|\mathbf{r}_i - \mathbf{R}|} \Psi \right) + \frac{1}{2} \sum_{i \neq j} \frac{e^2}{|\mathbf{r}_i - \mathbf{r}_j|} \Psi = E\Psi, \qquad (3.24)$$

where $\Psi = \Psi(\mathbf{r}_1 s_1, \mathbf{r}_2 s_2, \ldots, \mathbf{r}_N s_N)$ is the wavefunction of all the N electrons at positions $\mathbf{r}_i$ with spin orientation s_i, in a crystal with atoms of atomic number Z, at fixed positions $\mathbf{R}$ on a Bravais lattice. The potential energy term in the above equation is split into two parts: the negative potential energy term in brackets is the electrostatic potential of the ions, and the last term represents the interaction of each electron with

---

[t]Although the routine rejects a lot of impossible structures, the criteria for rejection is very simplistic, allowing nonsense atomic positions to still be accepted.

all the other electrons (the $\frac{1}{2}$ term comes from the fact that the sum does not distinguish between each electron, so each electron pair would be counted twice, instead of just once).

However, in just a cubic centimetre of such a simple compound as salt, there are approximately 10^{21} electrons. Even with today's computing power, a many-body calculation of this magnitude would not be feasible. Therefore, the first step is to decouple the many-body problem into that of a single-electron equation, acted upon by an effective potential, which includes the way ions interact with other ions (ion-ion interaction), electrons with other electrons (electron-electron interaction), and electrons with the underlying lattice of ions (electron-ion interaction).

The electron-ion interaction and the functional form of the electronic wavefunction is specific to the method of calculation. For example, in the pseudo-potential method, a plane-wave basis set is used to describe the electronic wavefunctions which are acted upon by an effective, or pseudo-potential, to reduce the effect of the strongly attractive ions on the electrons near the atom cores. However, in the Full-Potential Linearised Augmented Plane-Wave (FP-LAPW) method, the electronic wavefunctions are described by a superposition of plane-waves and spherically symmetric functions, as is the electron density which is used to compute the crystalline potential. These aspects will be described in more detail in a later section, where the FP-LAPW is described in some depth, as it was used in chapter 5 to compute the total energies of various high pressure crystal structures in the copper-halide, CuCl. The ion-ion interaction and the more complex electron-electron interactions will be outlined in detail within this section.

One problem is evident from equation 3.24. In order to compute the energy of each electronic band, the wavefunction must be known. But this is precisely what must be evaluated. Therefore, the calculation is performed self-consistently, *i.e* an initial potential, U, is guessed and equation 3.24 is solved to extract the electronic wavefunctions. These wavefunctions are then used to calculate a new potential, and

the whole process is repeated until the new potential is the same (within a tolerable limit) as the previous potential.

3.2.1 Ion-ion interactions

The ion-ion interaction is just the Coulombic potential between the bare ions, located at sites R_I within the Bravais lattice (where I is the index for each ion). It is well known that this ionic Coulombic potential takes the form

$$U^{coul}(r) = -\alpha \frac{e^2}{r}, \tag{3.25}$$

where e is the electronic charge, r is the distance from the ion and α is a constant (known as the Madelung constant) which depends upon the arrangement of atoms within the crystal structure. The determination of the constant α is complex, but can be computed efficiently using the Ewald method [45, 46].

The electrostatic potential energy for a set of point charges q_i is

$$E_{el} = \frac{1}{2} \sum_i q_i V_i, \tag{3.26}$$

where V_i is the electrostatic potential at the position of the ith charge produced by all the other charges (the one half term compensates for the fact that the sum counts each atom pair twice). This can be written as

$$E_{el} = \sum_{(i,j)} \frac{q_i q_j}{r_{ij}}, \tag{3.27}$$

where r_{ij} is the distance between the ith and j^{th} charges, and the sum is over all atom pairs. Hence, the electrostatic potential is

$$V_i = \sum_{(i,j)} \frac{q_i}{r_{ij}} \tag{3.28}$$

A direct summation of equation 3.27 is very inefficient, even when using numerical techniques that utilise the structure of the crystal lattice.

The Ewald method does not directly sum the electrostatic potential at each point in the lattice, but instead solves Poisson's equation for a given density. By assuming a unit positive charge at the lattice points of a Bravais lattice, surrounded by a uniform distribution of negative charge (in order to cancel exactly the positive charge, hence making the crystal electrostatically neutral), the problem is reduced to solving Poisson's equation

$$\nabla^2 \phi = -\frac{\rho}{\varepsilon_o}, \tag{3.29}$$

where ϕ is the potential, ρ is the charge density and ε_o is the permittivity of free space. Using the periodicity of the crystal lattice, the charge density can be re-expressed as a Fourier series

$$\rho = \sum_{\mathbf{K}_m} P(\mathbf{K}_m) e^{i\mathbf{K}_m \cdot \mathbf{r}}, \tag{3.30}$$

where the $\mathbf{K}_m$ are the reciprocal lattice vectors and the $P(\mathbf{K}_m)$ are the coefficients of the Fourier series. Hence the solution of Poisson's equation is

$$\phi = \frac{1}{\varepsilon_o} \sum_{\mathbf{K}_m, \mathbf{K}_m \neq 0} P(\mathbf{K}_m) \frac{e^{i\mathbf{K}_m \cdot \mathbf{r}}}{\mathbf{K}_m^2}, \tag{3.31}$$

and the coefficients of the Fourier series are

$$P(\mathbf{K}_m) = \frac{1}{\Omega} \int \rho(\mathbf{r}) e^{i\mathbf{K}_m \cdot \mathbf{r}} d^3\mathbf{r}, \tag{3.32}$$

where Ω is the volume of the unit cell, and the integration is over the whole unit cell.

In order to make the coefficients decrease with $|\mathbf{K}_m|$, Ewald chose a Gaussian distribution to describe the charge density at each lattice point

$$\epsilon^3 \pi^{-\frac{3}{2}} e^{-\epsilon^2 r^2}, \tag{3.33}$$

where ϵ is the parameter determining the width of the Gaussian distribution, and the factor $\epsilon^3 \pi^{-\frac{3}{2}}$ normalises the Gaussian curve. This choice of charge density distribution enables the sum in equation 3.31 to converge rapidly, for a correctly chosen width parameter, ϵ.

However, the actual sum required is for a set of positive point charges at the lattice sites, with a uniform negative distribution. In order to compensate for this in our reciprocal space sum of positive Gaussian potentials at the lattice sites, it is necessary to add the potential of positive point charges, whose charge is equalised by a negative Gaussian distribution. The two Gaussian distributions cancel each other, leaving only the desired potential. The second part of the sum involving point charges and a negative Gaussian distribution converges rapidly in real space, since the contributions to the total potential from the negative Gaussian tails decrease at more distant lattice points. This clever technique of splittng the sum into real and reciprocal space components allows the solution to converge rapidly.

3.2.2 Electron-electron interaction

The electron-electron interaction in the effective potential, created when re-expressing equation 3.24 as a single particle equation, can be written as

$$U^{el}(\mathbf{r}) = -e \int d\mathbf{r}' \rho(\mathbf{r}') \frac{1}{|\mathbf{r} - \mathbf{r}'|}, \tag{3.34}$$

where the potential at point $\mathbf{r}$ is calculated by assuming a smooth distribution of negative charge, density $\rho(\mathbf{r})$. If it is then assumed that all the electrons are independent, the charge density of an electron, wavefunction $\psi_i(\mathbf{r})$, in state i is

$$\rho_i(\mathbf{r}) = -e|\psi_i(\mathbf{r})|^2, \tag{3.35}$$

which gives a total charge density

$$\rho(\mathbf{r}) = -e \sum_i |\psi_i(\mathbf{r})|^2. \tag{3.36}$$

This leads to the the Hartree equations for each occupied one-electron level $\psi_i(\mathbf{r})$

$$-\frac{\hbar^2}{2m}\nabla^2\psi_i(\mathbf{r}) + U^{ion}\psi_i(\mathbf{r}) + \left[e^2\sum_j \int d\mathbf{r}'|\psi_j(\mathbf{r}')|^2\frac{1}{|\mathbf{r}-\mathbf{r}'|}\right]\psi_i(\mathbf{r}) = \varepsilon_i\psi_i(\mathbf{r}), \tag{3.37}$$

where U^{ion} is the potential from the ions, given in equation 3.24, as the second term in the sum over electrons.

However, the assumption that the electrons are independent of each other is incorrect, so the approximation to the many-electron problem in equation 3.37 will not give accurate answers to any complex system of electrons and ions. Therefore, the next level of accuracy is to include the fact that electrons are fermions, and hence, the wavefunction of a many-electron system must be antisymmetric under exchange of any two electrons. With this additional interaction included, the previously assumed smooth distribution of negative charge will have "holes" present. This is due to the fact that electrons with the same spin orientations will tend to avoid each other, in accordance with the Pauli exclusion principle. This will act to reduce the energy contributed by the Coulombic repulsion between each electron, with the reduction in energy being the so-called *exchange energy*.

When electrons are assumed to be independent of one another, the N-electron wavefunction, Ψ, may be written simply as the product of all the individual independent one-electron wavefunctions,

$$\Psi(\mathbf{r}_1 s_1, \mathbf{r}_2 s_2, \cdots, \mathbf{r}_N s_N) = \psi_1(\mathbf{r}_1 s_1)\psi_2(\mathbf{r}_2 s_2)\cdots\psi_N(\mathbf{r}_N s_N), \tag{3.38}$$

where ψ_i, $i = 1, 2, \cdots, N$ are the one-electron wavefunctions at positions $\mathbf{r}_i$ with spin

orientations s_i. However, this simple product is invariant under an interchange of two electrons. To introduce antisymmetry, a linear combination of products, each weighted with either $+1$ or -1 may be used, which forces the desired antisymmetry.

$$\Psi = \psi_1(\mathbf{r}_1 s_1)\psi_2(\mathbf{r}_2 s_2)\cdots\psi_N(\mathbf{r}_N s_N) - \psi_2(\mathbf{r}_2 s_2)\psi_1(\mathbf{r}_1 s_1)\cdots\psi_N(\mathbf{r}_N s_N) + \cdots \quad (3.39)$$

This can be written more efficiently as a Slater determinant,

$$\Psi = \begin{vmatrix} \psi_1(\mathbf{r}_1 s_1) & \psi_1(\mathbf{r}_2 s_2) & \cdots & \psi_1(\mathbf{r}_N s_N) \\ \psi_2(\mathbf{r}_1 s_1) & \psi_2(\mathbf{r}_2 s_2) & \cdots & \psi_2(\mathbf{r}_N s_N) \\ \vdots & \vdots & & \vdots \\ \psi_N(\mathbf{r}_1 s_1) & \psi_N(\mathbf{r}_2 s_2) & \cdots & \psi_N(\mathbf{r}_N s_N) \end{vmatrix} \quad (3.40)$$

Thus the solution to the N-electron Schrödinger equation will be similar to the previously stated Hartree equations, with the inclusion of another term expressing the antisymmetry of the wavefunction. The resultant solutions are the Hartree-Fock equations

$$-\frac{\hbar^2}{2m}\nabla^2\psi_i(\mathbf{r}) + U^{ion}\psi_i(\mathbf{r}) + U^{el}(\mathbf{r})\psi_i(\mathbf{r}) - \sum_j \int d\mathbf{r}' \frac{e^2}{|\mathbf{r}-\mathbf{r}'|}\psi_j^*(\mathbf{r})\psi_i(\mathbf{r}')\psi_j(\mathbf{r})\delta_{s_i s_j}$$

$$= \varepsilon_i\psi_i(\mathbf{r}), \quad (3.41)$$

where U^{el} is the Hartree electron-electron interaction in equation 3.34, and $\delta_{s_i s_j}$ is the Kronecker delta of two electrons with spin states s_i and s_j. This last term (the exchange energy) is, as stated previously, a reduction to the total energy. It takes the same form as U^{el} in equation 3.37, but with the necessary inclusion of the complex conjugate of ψ_j and the Kronecker delta to separate electrons in the same state.

This complex addition to the Hartree equations can give an exact solution for a free electron gas, *i.e.* no periodic potential. However, even in the solution of the free electron gas, additional terms must be introduced to give an exact answer [47]. These

extra terms, which are not related to any physically meaningful quantity, are the *correlation energy* contributions. The intractability of the exchange and correlation energy contributions in a periodic potential using Hartree-Fock means a new formulation for the solution of the Schrödinger equation is required, allowing exchange and correlation to be better approximated. A simpler method would be to re-express the Schrödinger equation in terms of electron density, which could once again be approximated by a set of single-electron equations, with each electron immersed in a sea of negative charge from all other electrons. This would enable the effects of exchange and correlation energy to be approximated at local points within the whole electron charge density. This is exactly what the local-density approximation within density-functional theory achieves.

3.2.3 Density-functional theory

As noted in the previous section, the first step in simplifying the effects of exchange and correlation, is to re-express the Schrödinger equation in terms of electron density. This is where density-functional theory can be used, which proves that the total energy of an electron gas is a unique functional of the electron density, even in the presence of an external potential, such as the Coulombic potential in a crystal lattice. Kohn and Sham [2] showed that this functional can be written as

$$E[n(\mathbf{r})] = \int U_{ion}(\mathbf{r})n(\mathbf{r})d^3\mathbf{r} + \frac{e^2}{2} \int \int \frac{n(\mathbf{r})n(\mathbf{r}')}{|\mathbf{r} - \mathbf{r}'|}d^3\mathbf{r}d^3\mathbf{r}' + E_{Coul}(|\mathbf{R}|) + G[n(\mathbf{r})], \quad (3.42)$$

where U_{ion} is the total static electron-ion potential, and E_{Coul} is the inter-nuclear ionic Coulomb energy for ions at positions $\mathbf{R}$. The functional $G[n(\mathbf{r})]$ is a sum of the single-particle kinetic energy and effects of the exchange and correlation energy, E_{xc}, in an interacting system with electron density $n(\mathbf{r})$ at position $\mathbf{r}$. The minimum of equation 3.42 gives the ground-state energy of the crystal, which yields the electronic

wavefunction, ψ, from the density

$$n(\mathbf{r}) = \sum_i |\psi_i(\mathbf{r})|^2,$$ (3.43)

These are found from a solution of the Kohn Sham equations,

$$\left[\frac{-\hbar^2}{2m}\nabla^2 + U_{ion}(\mathbf{r}) + U_{el} + U_{xc} \right] \psi_i(\mathbf{r}) = \varepsilon_i \psi_i(\mathbf{r}),$$ (3.44)

where U_{el} is the Hartree potential (eqn. (3.34)), ε_i is the Kohn-Sham eigenvalue, and U_{xc} is the exchange and correlation potential, which is given by the functional derivative of E_{xc} with respect to the electron density

$$U_{xc}(\mathbf{r}) = \frac{\delta E_{xc}[n(\mathbf{r})]}{\delta n(\mathbf{r})}.$$ (3.45)

The next step towards a solution of the Kohn Sham equations is to approximate an expression for U_{xc} in terms of the electron density. The method most widely adopted in total energy calculations is the local-density approximation.

3.2.4 Local-Density Approximation

Since the exchange and correlation energy contributions are dependent upon the state of all the electrons in the solid, the ideal exchange-correlation energy term would be accurate at every point in space. This is not a feasible calculation to perform with present computing capabilities, so an obvious approximation to the ideal situation would be to use a value of the exchange-correlation energy at localised points in space to represent the exchange-correlation energy in a region within the locality of the point. This is the foundation of the local-density approximation [2].

By assuming that the exchange-correlation energy contribution per electron at a point $\mathbf{r}$ in the electron gas, $\varepsilon_{xc}(\mathbf{r})$, is equal to the exchange-correlation energy contribution per electron in a homogeneous electron gas, $\varepsilon_{xc}^{hom}(\mathbf{r})$ that has the same density

as the electron gas at point **r**, equation 3.45 may be equated to

$$\frac{\delta E_{xc}[n(\mathbf{r})]}{\delta n(\mathbf{r})} = \frac{\delta[n(\mathbf{r})\varepsilon_{xc}(\mathbf{r})]}{\delta n(\mathbf{r})}, \tag{3.46}$$

where

$$\varepsilon_{xc}(\mathbf{r}) = \varepsilon_{xc}^{hom}[n(\mathbf{r})]. \tag{3.47}$$

Many different parameterisations exist that link the exact results for the exchange-correlation energy contribution of homogeneous gases at different densities using interpolation methods [2, 48, 49, 50]. The choice of which parametrisation to use depends on the type of total energy calculation and the materials being studied.

3.2.5 k-point sampling

In order to make quantum mechanical calculations such as these tractable for a three-dimensional crystalline solid, the infinite extent of the crystal is approximated by that of a finite repeatable unit, or unit cell. The symmetry of the solid imposes boundary conditions on the unit cell, which may be used to represent any periodic function of infinite extent within the crystal, such as the electronic wavefunctions, as the product of a cell-periodic part and a wavelike part. This is known as Bloch's Theorem, and takes the form

$$\phi_i(\mathbf{r}) = e^{i\mathbf{k}\cdot\mathbf{r}} f_i(\mathbf{r}), \tag{3.48}$$

where ϕ_i are the wavefunctions of the i electrons in the crystal at position **r** with wavevector **k**, described as a function of the periodicity of the cell, f_i.

Although Bloch's Theorem removes the need to calculate the infinite number of electronic wavefunctions in a bulk solid, the finite set of wavefunctions is offset by the infinite number of k-points that each electron wavefunction must be computed at.

However, wavefunctions at neighbouring k-point states will have approximately the same value, and hence this infinite extent can be reduced by coarse-graining methods. The locations of chosen k-points could be totally random, or just general points in the Brillouin zone. To reduce the size of the k-point set, the symmetry of the crystal can again be used to find points of low symmetry that occupy separate locations within the irreducible part of the Brillouin zone in k-space. Thus, many points in k-space can be represented by just a single point in the Brillouin zone.

Several methods have been formulated to calculate the optimum position and weighting of special k-points within the Brillouin Zone which lead to the greatest density of k-points [51, 52, 53]. Although each method is just an approximation of the exact solution, the error in the total-energy calculation may be reduced by using larger sets of special k-points.

3.2.6 The Full-Potential Linearized Plane-Wave (FP-LAPW) method

The basic methods outlined in the previous sections are used in many of the total energy calculations used today. However as mentioned already, each method differs in the way the electron-ion interaction is described, and how the electronic wavefunction is represented.

In the FP-LAPW method used in chapter 5 [54], the potential of the ions (screened by the core electrons) felt by the valence electrons is described in two distinct regions. In the vaccinity of the ions[‡], the potential is described by the product of a spherically symmetric function and a radial function

$$U_{ion}(\mathbf{r}) = \sum_{L,M} U_{LM}(r) Y_L^M(r), \qquad (3.49)$$

where the spherical harmonics Y_L^M calculated at angular momentum quantum numbers

---

[‡]Each ion species is given a sphere of influence which defines the core region of that ion. This region has been given the name "muffin-tin" radius [55].

L and M are weighted by the distance from the centre of the ion position by the radial

function $U_{LM}(r)$.

In the interstitial region between each ion, outwith the sphere of influence of the

ions, the potential is described by a product of plane waves

$$U_{ion}(\mathbf{r}) = \sum_{\mathbf{K}} U(\mathbf{K}) e^{i(\mathbf{K} \cdot \mathbf{r})}, \tag{3.50}$$

where the plane waves are summed over the reciprocal lattice vectors $\mathbf{K}$, and weighted

by the function $U(\mathbf{K})$.

The electronic wavefunction is described in two similar regions using functions sim-

ilar to the potential. Within the ion spheres, the wavefunction is represented by the

product of spherical harmonics and a linear combination of radial functions, and outside

the ion spheres it is represented by a plane wave.

Inside the sphere,

$$\psi(\mathbf{k}_n, \mathbf{r}) = \sum_{l,m} \left[A_{lm}(\mathbf{k}_n) u_l(r, E_l) + B_{lm}(\mathbf{k}_n) \dot{u}_l(r, E_l) \right] Y_{lm}(\hat{\mathbf{r}}), \tag{3.51}$$

whilst outside the sphere,

$$\psi(\mathbf{k}_n, \mathbf{r}) = \frac{1}{\sqrt{\Omega}} e^{i(\mathbf{k}_n \cdot \mathbf{r})}, \tag{3.52}$$

where the spherical harmonics Y_{lm}, computed at angular momentum quantum numbers

l and m, are multiplied by the sum of the radial function u_l computed at energy E_l and

its partial derivative with respect to energy $\dot{u}_l = \frac{\delta u_l(r,E)}{\delta E}\Big|_{E_l}$. The interstitial electronic

wavefunctions, expressed as plane-waves, are calculated at $\mathbf{k}_n = \mathbf{k} + \mathbf{K}_n$, where $\mathbf{k}$ is a

reduced wave vector in the first Brillouin zone and the $\mathbf{K}_n$ the reciprocal lattice vectors,

and scaled by the unit cell volume Ω.

The plane-wave in the interstitial region is augmented with the spherically symmet-

ric function in the core region by solving (3.51) for A_{lm} and B_{lm}, and matching their

value and slope with the plane-wave description (3.52) at the sphere boundary. This

expression for the electronic wavefunction is hence called an augmented plane-wave (APW). The linearisation of u_l in (3.51) gives the FP-LAPW method part of its name (LAPW), and is required since the energy at which it is calculated depends on the final energy eigenvalue for the electron wavefunction. By linearising this function, and using an initial guess for E_l, the direct energy dependence is removed [56].

Now that the electron-ion interaction has been defined, and the basis set for the electronic wavefunction has been set-up, the FP-LAPW computation can now proceed. The method of calculation is best described in a series of steps that are iterated until the input and output charge densities are the same, within a tolerated value.

The five boxes in figure 3.3 represent five separate sections of code in the FP-LAPW program. These five sections of code run sequentially, producing output that is read in as input by the next section. Initial charge densities for the bare ions are used as the full charge density in the first cycle, from which the Schrödinger equation is solved to find the electronic eigenvalues and eigenvectors. Valence and core charge densities are then computed, using equations such as 3.43. These charge densities are then combined to give a total crystal charge density. This total charge density is "mixed" with the charge density from the previous cycle[§], which is then used to compute the crystal potential by solving Poisson's equation [57]

$$\nabla . \nabla U_{ion} = -\frac{\rho}{\varepsilon_o}, \quad (3.53)$$

for charge density ρ, where ε_o is the permittivity of free space. The charge density from the current and previous iterative cycles are mixed to reduce the number of cycles required to relax the system into an equilibrium state.

[§]The densities are mixed in the ratio $n\rho_i + (n-1)\rho_{i-1}$, where n is a number between 0 and 1 given in one of the input files, and ρ_i is the charge density at iterative cycle i.

```
                        ( START )
                            │
                            ▼
        ┌───────────────────────────────────────┐
        │ Solve Schrödinger's Equation          │
    ┌──▶│ to compute the electron               │
    │   │ eigenvalues and eigenvectors          │
    │   │ from the crystal potential            │
    │   └───────────────────────────────────────┘
    │                       │
    │                       ▼
    │       ┌───────────────────────────────┐
    │       │ Compute valence charge        │
    │       │ density from eigenvalues      │
    │       │ and eigenvectors.             │
    │       └───────────────────────────────┘
    │                       │
    │                       ▼
    │       ┌───────────────────────────────┐
    │       │ Compute core states           │
    │       │ and densities                 │
    │       └───────────────────────────────┘
    │                       │
    │                       ▼
    │       ┌───────────────────────────────┐
    │       │ Mix input and output          │
    │       │ charge densities              │
    │       └───────────────────────────────┘
    │                       │
    │                       ▼
    │       ┌───────────────────────────────┐
    │       │ Generate new potential        │
    │       │ from charge densities         │
    │       └───────────────────────────────┘
    │                       │
    │                       ▼
    │                  ╱─────────╲
    │                 ╱ Is the     ╲
    │                ╱ new potential ╲
    └───────────────◀   same as the   ▶
               NO    ╲ old potential? ╱
                      ╲─────────────╱
                            │ YES
                            ▼
                        ( END )
```
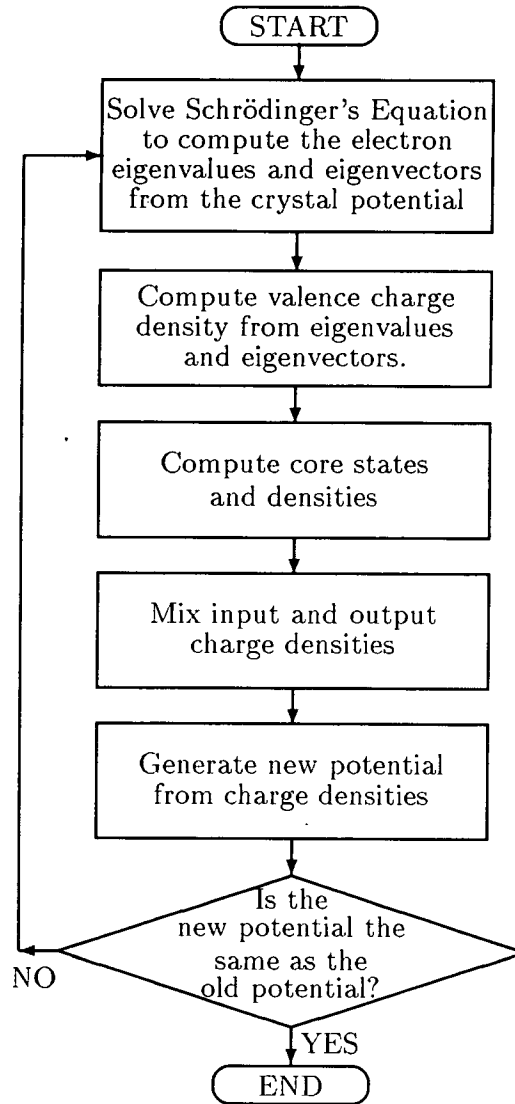
Figure 3.3. The FP-LAPW method is summarised here in a series of steps.

Chapter 4

Study of a high pressure phase of silicon, Si-XII

Using angle-dispersive x-ray powder diffraction with image-plate area detectors, high pressure structural phase transitions were observed in silicon. Particular interest was given to the body-centred cubic phase of silicon (Si-III), existing between 100kbar and ambient pressure, obtained after decompression from the high pressure β-tin form, which exists above 100kbar. Previous experiments had shown extra reflections present in diffraction patterns of phase III under pressure, which were unaccounted for by the cubic structure. These additional lines were shown to be produced by a separate, new phase of silicon, hereafter named Si-XII.

My contribution to this work was in the generation and analysis of the diffraction patterns from Rietveld refinements, and the use of the Monte-Carlo method to re-compute the structure of Si-XII. The rhombohedral Bravais lattice for Si-XII was determined by Dr. Ross Piltz, and the crystal structure solved by Dr. Jason Crain.

4.1 Background

To date, twelve different crystalline phases have been reported, both stable high pressure phases, and meta-stable structures obtained after decompression. Only four phases are studied in this chapter, all existing at room temperature, between ambient pressure and (127 ± 6)kbar*. At ambient pressure, silicon adopts a diamond-type structure (Si-I), which then transforms to a metallic β-tin type structure (Si-II) at about 120kbar [58, 59, 60]. Decompression from this state does not lead to the recovery of the diamond phase. Instead, a body-centred cubic structure with 8 atoms in the primitive rhombohedral unit cell (Si-III) has been observed from about 100kbar to ambient pressure [61, 62]. Until recently, the Si-III phase had not been examined under pressure experimentally. Only ab-initio calculations had tested the stability of the structure at elevated pressures [63, 64, 65]. This chapter is an investigation into the effects of pressure on Si-III and a detailed study of the newly refined phase of silicon, Si-XII, existing between Si-II and Si-III, at pressures between about 20kbar and 100kbar [66, 67].

4.2 Structural details

4.2.1 Si-I: The diamond structure

The only elements to adopt the diamond structure under normal conditions of pressure and temperature are carbon, silicon, germanium and α-tin. This structure is characteristic of these covalently bonded elements, where bond directionality plays the dominant role in structural adoption.

The diamond structure of silicon, Si-I, is a face-centred cubic structure, with basis atoms at fractional co-ordinates $(0,0,0)$ and $(\frac{1}{4},\frac{1}{4},\frac{1}{4})$. This corresponds to spacegroup $Fd3m$ (in international notation), with atoms on the $8(a)$ sites, as given by Wyckoff

---

*As mentioned in section 2.3.2, below 100kbar there is a 3% error associated with pressure measurements within a diamond-anvil cell using the ruby fluorescence technique (which was used in this set of experiments), and about a 5% error above 100kbar.

notation. At ambient pressure the lattice parameter, a, is 5.43Å [68]. A projection of this structure along the z-axis is given in figure 4.1.

As can be seen, there are only two different contact distances, one bonded, the other non-bonded. The bonded distances lie between atoms forming regular tetrahedra, with each atom separated by 2.35Å at ambient pressure. The non-bonded distances correspond to the separation of atoms at the corners of the tetrahedra, which are all 3.84Å apart under normal conditions.
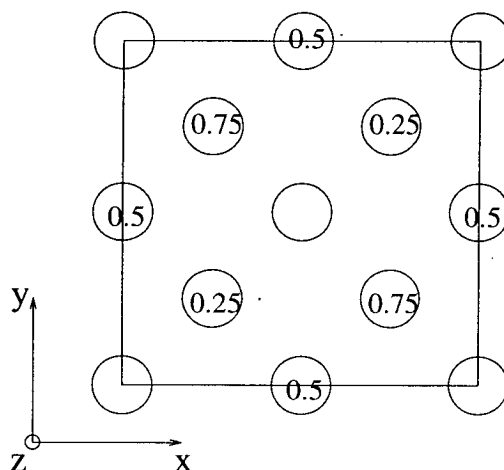
Figure 4.1. The diamond structure of Si-I, as viewed down the z-axis (the arrows show the direction of the axes). The circles signify atomic positions and the numbers within the circles are fractional heights up the z-axis. Atoms without numbers are at zero height.

The packing ratio of the diamond structure is 34%. That is, 34% of space within the primitive unit-cell is occupied by the basis atoms, assuming the atoms are filling space as if they were hard spheres. As mentioned before, the s-p hybridisation of the energy bands in silicon creates the need for a tetrahedrally co-ordinated structure, even though this is a very inefficient way to arrange atoms, in terms of space-filling arguments.

4.2.2   Si-II: The β-tin structure

Si-II adopts the β-tin structure. At ambient pressure, tin exists in two forms, labelled α and β. The α-Sn structure is the diamond structure of Si-I, and is observed in Sn

below 286.4K. Above this temperature, the β-Sn phase is adopted, which is a body-centred tetragonal structure. The spacegroup for this structure is $I4_1/amd(1)$, and contains five atoms; four on the $4(a)$ sites, and one at the unit cell centre. For silicon, the lattice parameters observed just after the transition are $a=4.686$Å and $c=2.585$Å [58, 14]. This structure is related to the diamond structure by a contraction of the c-axis, and by re-assigning the a and b-axes in the β-tin phase as the (110) and ($\bar{1}$10) planes in the diamond structure, respectively. Figure 4.2 shows a schematic diagram [6] of this relation.

This structure also corresponds to the maximum packing ratio for the diamond structure when the c-axis is compressed. By keeping atoms fixed in the diamond arrangement and contracting the c-axis, the maximum packing ratio of 55% is obtained at a $\frac{c}{a}$ ratio of 0.37, which corresponds to a $\frac{c}{a}$ ratio in the β-tin structure of 0.524[†] (see figure 4.3). This compares favourably with the observed $\frac{c}{a}$ ratio in the β-tin structure, which is 0.54. The difference in the calculated and experimental values for the $\frac{c}{a}$ ratios could be due to the fact that atoms cannot be likened exactly to hard spheres. If the volume occupied by an atom can be approximated to that of a sphere, then since the diamond structure is not a Bravais lattice, the local charge distribution around each basis atom will be different. This would invalidate the assumption that the atomic radii of both basis atoms are the same. Therefore, the calculated results may approach the experimental data by adopting slightly different atomic radii for each basis atom.

However, the actual transition is not such a simple mechanism, since it is irreversible. If packing of hard spheres was a valid model for such a transition, then a contraction of the c-axis in the diamond structure would be the preferred route (although a slight increase in the packing fraction can be obtained by distorting the structure orthorhombically, similar to the high pressure *Imma* phase observed in III-V

[†]Since the a and b-axes of the β-tin structure are equal to the (110) and ($\bar{1}$10) directions in the diamond structure, the value of 0.37 for the $\frac{c}{a}$ ratio in the diamond structure must be multiplied by $\sqrt{2}$ to convert it to the $\frac{c}{a}$ ratio in the β-tin structure.

compounds [69]), but the bonding nature of silicon at pressures below the transition to the β-tin structure suggests atomic co-ordination plays a dominant role.
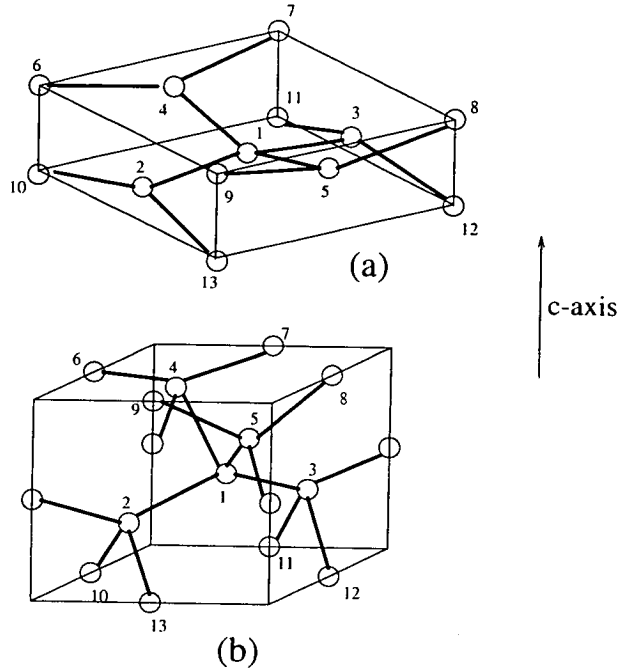

Figure 4.2. The diamond structure (b) can become the β-tin structure by compressing the c-axis. The numbered atoms in each cell correspond to one another, showing the equivalence of the two structures.
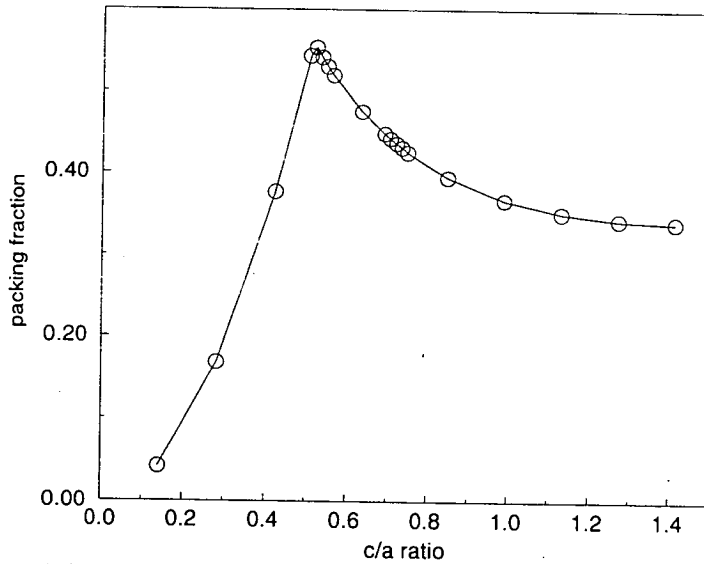

Figure 4.3. The $\frac{c}{a}$ ratio given is for β-tin. Maximum packing efficiency occurs at $\frac{c}{a} = 0.524$, and when this ratio reaches a value of 1.141, the diamond structure is obtained.

4.2.3 Si-III: The BC8 structure

The structure of Si-III [62] is that of a body-centred cube, with 16 atoms within the unit cell. The name BC8 comes from both the conventional unit cell (which is body-centred) and the primitive unit cell (which contains eight atoms). The spacegroup is $Ia\overline{3}$, with atoms on the $16(c)$ sites, (v, v, v). There are two distinct bond lengths (one short and one long) and two bond-angles in this structure. These can all be related to the atomic fractional co-ordinate, v, and the lattice parameter, a_o.

$$\frac{R_A}{a_o} = 2v\sqrt{3}, \tag{4.1}$$

$$\frac{R_B}{a_o} = \sqrt{8v^2 - 2v + 0.25}, \tag{4.2}$$

$$cos\theta_{AB} = \frac{(8v - 1)}{\sqrt{96v^2 - 24v + 3}}, \tag{4.3}$$

$$cos\theta_{BB} = \frac{(4v^2 - v)}{8v^2 - 2v + 0.25}, \tag{4.4}$$

where R_A and R_B denote the short and long bond-lengths respectively, and θ_{AB} and θ_{BB} are the angles between an A and a B bond and between two B bonds. A schematic diagram of this structure is shown in figure 4.4. Both the A and B lengths correspond to contact distances between bonded atoms, giving four-fold co-ordination, but each atom also has a unique non-bonded nearest neighbour. This distance, R_5, can be described in terms of the atomic co-ordinate and the lattice parameter as

$$\frac{R_5}{a_o} = (0.5 - 2v)\sqrt{3} \tag{4.5}$$

This body-centred cubic cell may be re-expressed in the primitive setting as a rhombohedral structure (see figure 4.5(a)), spacegroup $R\overline{3}$, with two atoms on the $2(c)$, (u, u, u), and six atoms on the $6(f)$, (x, y, z), sites. The structural parameters in this setting, $(a, \alpha, u, x, y$ and $z)$ are related to the atomic co-ordinate v of the cubic

structure by $u = 2v$, $x = 0.5$, $y = 0$, $4z = 0.5 - 2v$ and $a = \frac{a_o\sqrt{3}}{2}$. The rhombohedral angle, α, is fixed at 109.47°. At ambient pressure, these structural parameters are [62] a=5.747Å ,α=109.47°, u=0.2006, x=0.5, y=0.0, and z=0.2994.

This structure has only been observed in Si and Ge, but not in any of the group III-V semiconductors, although they have been predicted to adopt the binary analogue of this structure [70]. This binary analogue, called SC16 (since it can be described in terms of a 16 atom simple cubic structure), has been observed experimentally in the copper halides, CuCl and CuBr [71]. The next chapter describes this structure in more detail, and presents results of *ab-initio* calculations on this phase for CuCl.
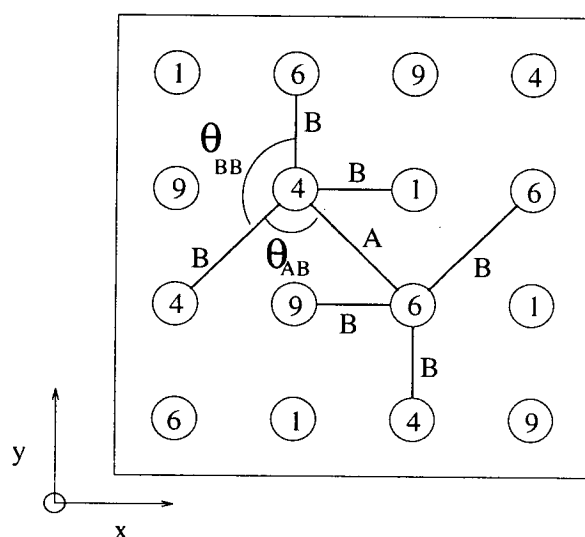

Figure 4.4. Schematic diagram of the structural arrangement of atoms in Si-III, in the body-centred cubic setting. Bond-lengths A and B are shown, as well as bond-angles θ_{AB} and θ_{BB}. The numbers within the circles denote the height of each atom (in tenths) up the z-axis, which is coming out of the page.

4.3   Experimental details

The angle-dispersive x-ray powder diffraction data was collected using the methods described in sections 2.1 and 2.2 at the Daresbury Synchrotron Radiation source. The

Si(111) monochromator was used to select a wavelength of 0.4652Å which was calibrated using a silicon standard. Pinholes of 50 or 75μm were used to collimate the monochromatic beam, and the two-dimensional diffraction patterns recorded on imageplates were scanned by a Molecular Dynamics 400A PhosphorImager. The computer program PLATYPUS was used to analyse the resulting Debye-Scherrer rings, as mentioned in section 2.1.2.

All samples originated from National Bureau of Standards [72] silicon standards with a purity of 99.9999%. The samples were loaded in tungsten gaskets, with a 4:1 mixture of methanol and ethanol as the pressure transmitting fluid, and a ruby chip to measure pressure by the ruby fluorescence method. The pressure of the sample was measured both before and after each set of image plate exposures.

4.4 Experimental results

4.4.1 Progression of phase transitions

Pattern number	Pressure(kbar)	Comments
1	127±6	Si-II phase
2	104±5	Si-II phase
3	97±3	Majority Si-II, minority Si-XII
4	89±3	Majority Si-XII, minority Si-II
5	82±2	Smaller Si-II component
6	63±2	Less Si-II component
7	46±1	No Si-II, fully Si-XII
8	28±1	Si-XII phase
9	ambient	Mixture of Si-III and Si-XII
10	16±1	Majority Si-III, minority Si-XII
11	25±1	Majority Si-XII, minority Si-III
12	27±1	Fully Si-XII
13	ambient	Si-III, annealed for two hours

Table 4.1. Summary of pressures at which images were recorded (usually at two different sample-to-plate distances (see section 2.1.2)).

As already mentioned, the sample of silicon in the diamond-anvil cell was initially pressurised to 127kbar, allowing the transition to the Si-II phase to be fully complete before the experiment began. The pressure was slowly released to ambient, recording several images on the down-stroke. Pressure was then increased to show any hysteresis in both directions (up-stroke and down-stroke) and to prove the reversibility of the phase transition between Si-III and Si-XII. Then finally, the sample was quenched to ambient pressure once again. The last image recorded at ambient pressure was obtained after the sample had been heated in an oven at 100°C for two hours in an attempt to reduce the amount of Si-XII by annealing. This was done to obtain accurate refinements of Si-III, making the experimental analysis of the relevant phases of silicon complete. A summary of the images obtained is given in Table 4.1, along with comments about the images observed at each pressure.

Figure 4.5 shows the progression of each phase mentioned so far (Si-I, Si-II, Si-III and Si-XII) with pressure. The shaded region between about 63kbar and 100kbar indicates the co-existence of Si-II and Si-XII on the down-stroke of pressure. Our observation of the onset of the transition from the β-tin phase at 100kbar is slightly lower than that of previous experiments [73, 74]. This is probably due to the slightly non-hydrostatic pressure environment experienced by the sample in the DAC.

The progress of the diffraction pattern on the down-stroke, shown in figure 4.6, gives an immediate impression of the transition between the tetragonal Si-II phase and the rhombohedral Si-XII phase. The onset of Si-XII occurs between (97 ± 3)kbar and (104 ± 5)kbar, which is indicated by the splitting of the $(20\bar{1})$, (112), $(10\bar{2})$ reflections around $2\theta=10°$, and the existence of the (110) reflection at about $11°$. Si-II and Si-XII co-exist until between (89 ± 3)kbar and (46 ± 1)kbar, below which Si-XII is stable. The increasing background intensity with decreasing angle in the Si-XII patterns indicates

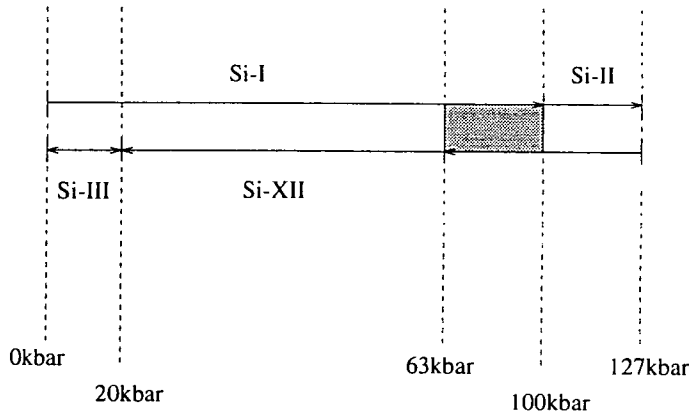that a degree of amorphisation accompanies the transition from Si-II.

Figure 4.5. Isothermal diagram at room temperature, showing the progression of phase transitions with pressure. Although no errors are quoted with each pressure, they are all subject to the same errors as given in table 4.1.
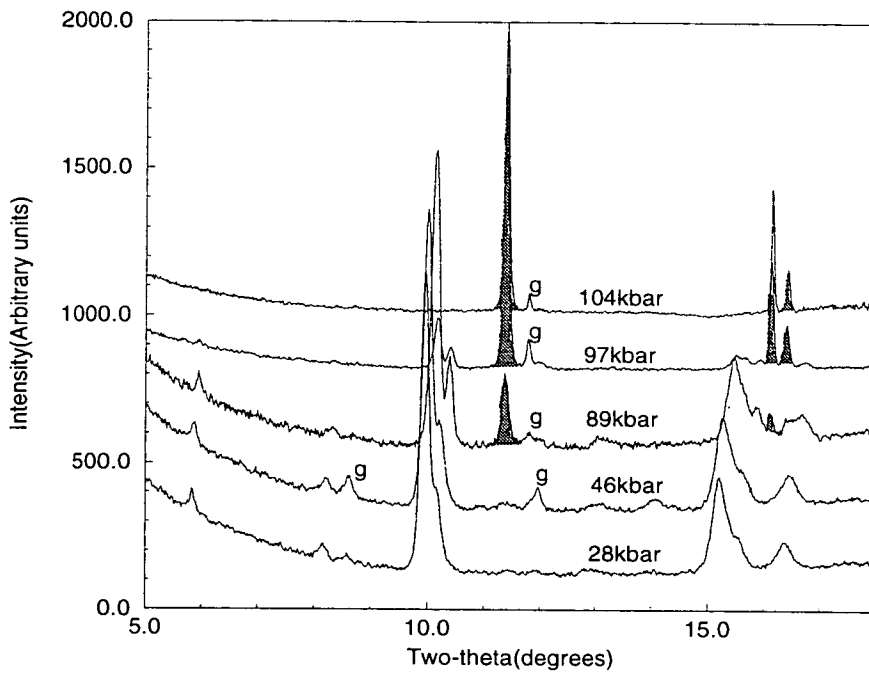

Figure 4.6. The onset of Si-XII is shown on the down-stroke from Si-II. The reflections marked g are from the tungsten gasket and the shaded reflections are those from Si-II. Unshaded reflections are produced by Si-XII.

In figure 4.7, pressure was being increased from ambient, showing the Si-III to Si-XII transition. The (211) and (321) reflections at 10° and 15° (as assigned in the cubic

setting) are clearly seen to split, and the extra (100) reflection (not permitted with body-centred cubic symmetry) appears at just above 5°, consistent with a rhombohedral distortion of the cubic cell.

Using the pattern obtained at ambient pressure, after being heated at 100°C for two hours, a structural refinement of Si-III was obtained (see figure 4.8). This was done for completeness, since the phase had already been solved [62]. The structural parameters obtained from the Rietveld refinement (as described in section 3.1.2) did not vary significantly from previously published values. Although there is slight disagreement in the cell parameters, the limited intensity accuracy of our data as well as the small number of observed reflections does not justify a re-evaluation of the previously accepted values.
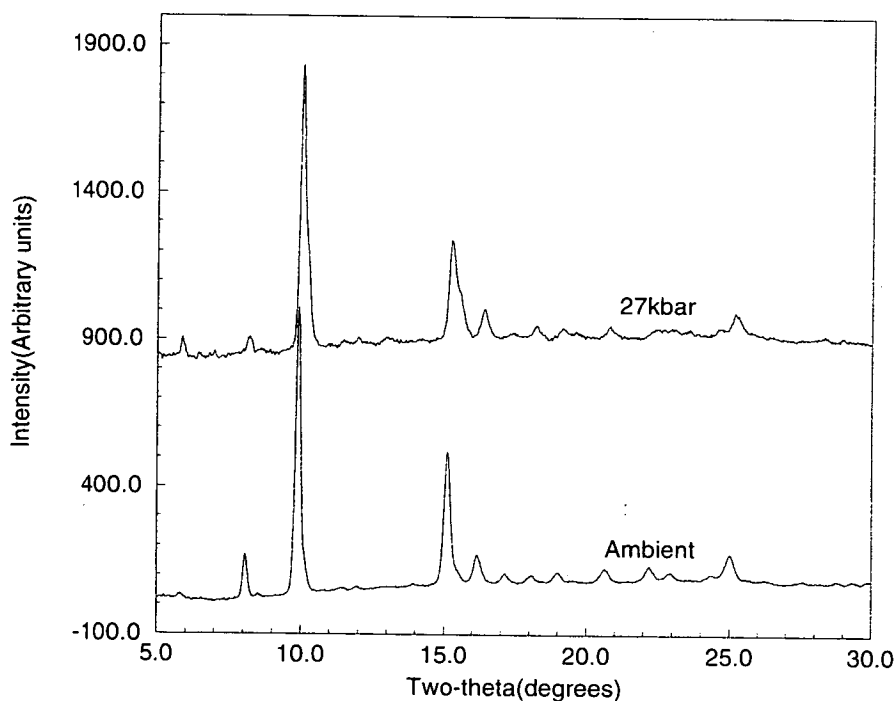

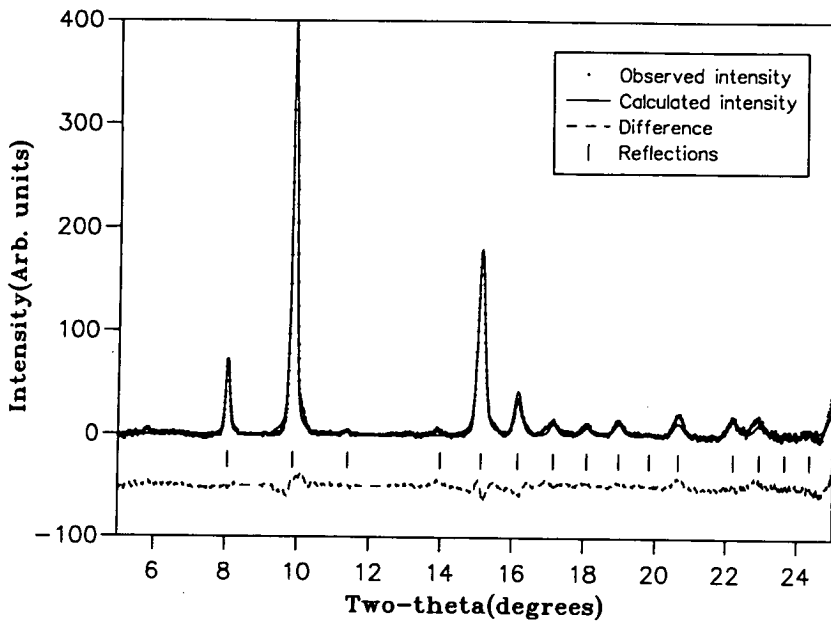**Figure 4.7.** Silicon being pressurised from ambient pressure.

Figure 4.8. The refinement of the BC8 phase of silicon, after being heated at 100°C for an hour is shown here.

4.4.2   Structure solution of Si-XII from *ab-initio* Monte-Carlo methods

From the experimentally collected diffraction profiles for Si-XII, there is evidence of a rhombohedral structure, which can be seen from the pattern of peak splitting. Due to the high quality of the collected data, the Monte-Carlo (MC) method was used to find atomic co-ordinates within a trial rhombohedral cell. One of the symmetry sub-groups of Si-III is $R\bar{3}$, which may also be used to describe Si-III in terms of a rhombohedral cell, as mentioned in section 4.2.3. Therefore, this trial spacegroup was used in the MC calculations.

Using data collected at a pressure of 82(2)kbar, the indexing program DICVOL91 [24, 25, 26] was used to find possible lattice parameters. Using the eight strongest peaks in the Si-XII diffraction pattern, only one possibility was produced, which corresponded to a rhombohedral lattice with unit-cell length a=5.6094Å and rhombohedral angle α=110.08°. The figure of merit, F, as described in section 3.1.1, had a value of 24.0,

which means the average difference between the calculated and experimentally observed peak positions was about 0.04°.

This data was used in the Monte-Carlo code, specifying the spacegroup $R\bar{3}$ with two atoms on (x, y, z) sites[‡] , with the atomic radius of each basis atom set to 1.5Å . After 5000 MC cycles, a definite clustering was observed at atomic positions (0.58(8),0.530(9),0.49(3)) and (0.17(2),0.22(2),0.58(1)). This clustering of atoms also included the best solution, which had an R-factor of about 9.8%, compared to the worst trial structures, with R-factors averaging about 10.3% (see figure 4.9).
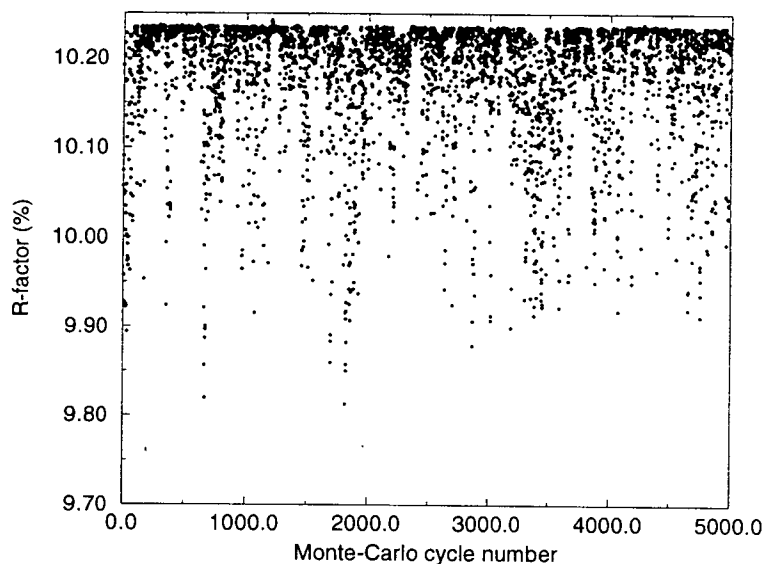

Figure 4.9. The change in R-factor for each Monte-Carlo step is shown here. Several trial structures can be seen to have been produced, with the best solution at MC cycle number 1819.

The x, y and z parameters of the first atom are very close to one another, indicating that it is on the special position (u, u, u). Averaging the atomic co-ordinates of the first atom gave $\bar{u}$=0.53(4). The structure was refined from the lattice parameters given by DICVOL91 and initial atomic co-ordinates from the Monte-Carlo code, using the

---

[‡]Using two atoms on general position within the rhombohedral $R\bar{3}$ symmetry results in twelve atoms. There are only eight atoms in the rhombohedral setting of Si-III, achieved by one of the atoms being on a special position. Since the location of this position was not known for the Si-XII structure, the maximum number of degrees of freedom were initially used.

Parameter	Initial	Refined	$\Delta(\%)$
$a(\text{Å})$	5.6094	5.6094	0
$\alpha(^o)$	110.08	110.07	0.009
u	0.53	0.71	18
x	0.17	0.04	13
y	0.22	0.26	4
z	0.58	0.46	12

Table 4.2. As can be seen, the percentage difference (Δ) between the refined atomic positions and those given by the Monte-Carlo method is small enough to lead to a successful Rietveld refinement.

MPROF Rietveld refinement code [34] (see figure 4.10). The final refined parameters are given in Table 4.2, along with the difference between those predicted by the Monte-Carlo code.
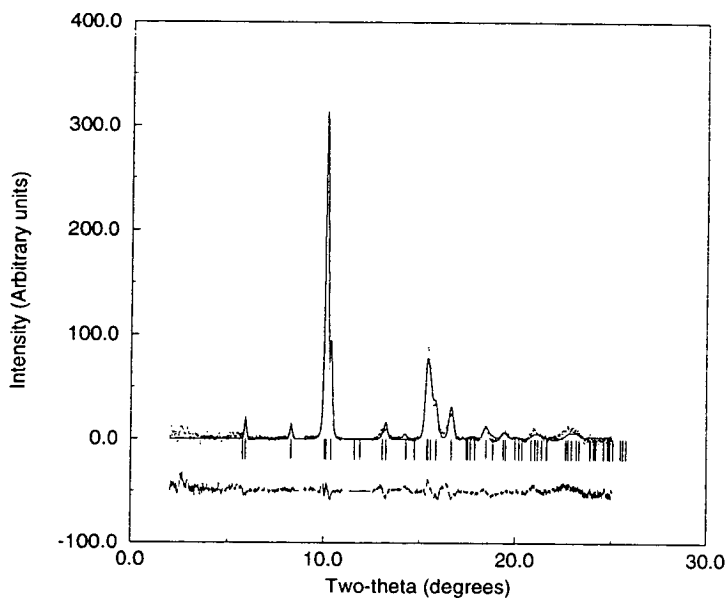

Figure 4.10. A Rietveld refinement of Si at 82(2)kbar is shown here. The dots are the experimental pattern, the solid line is the calculated profile. The line below the diffraction pattern indicates the difference between the calculated profile and experimentally observed data.

The differences between the refined atomic positions and those given by the Monte-Carlo method could have been further reduced by running the Monte-Carlo code for

more than 5000 cycles and also by increasing the minimum contact distance, although many more cycles would then have been required to find the best solution.

4.4.3 Si-XII: The R8 structure

The rhombohedral structure of Si-XII is similar to the rhombohedral cell of Si-III, except the atomic co-ordinates in Si-XII are unrelated, and the rhombohedral angle, α is free. The spacegroup is $R\bar{3}$, with eight atoms; two on $2(c)$, (u, u, u), sites and six on the $6(f)$, (x, y, z), sites (hence the name, R8, denoting an eight atom rhombohedral cell). The atoms on the $2(c)$ sites have two distinct bond lengths and bond angles, and the atoms on the $6(f)$ sites have three distinct bond lengths and six independent bond angles. A direct comparison of the rhombohedral structures of Si-III and Si-XII is given in figure 4.11.

Structurally, Si-XII is comprised of linked pairs of aplanar pentagonal rings running along the $< 100 >$ crystallographic directions. The sides of these pairs also form two distinct types of eight-membered rings. Irregular hexagonal rings occur at locations where two pentagons share a common side. There are two 2(c) site atoms in the five-fold rings and only one in the six-fold rings.

The increased number of independent internal degrees of freedom in Si-XII offers an explanation for silicon adopting this structure under high pressure. Since all the bond-lengths and angles in Si-III are related directly to the atomic co-ordinate and the lattice parameter through symmetry, only bond compression is possible under pressure to reduce the unit-cell volume. However, Si-XII is able to buckle under pressure, with independent atomic positions and a free rhombohedral angle. This type of volume reduction (by bond bending and buckling) will be much more energetically favourable
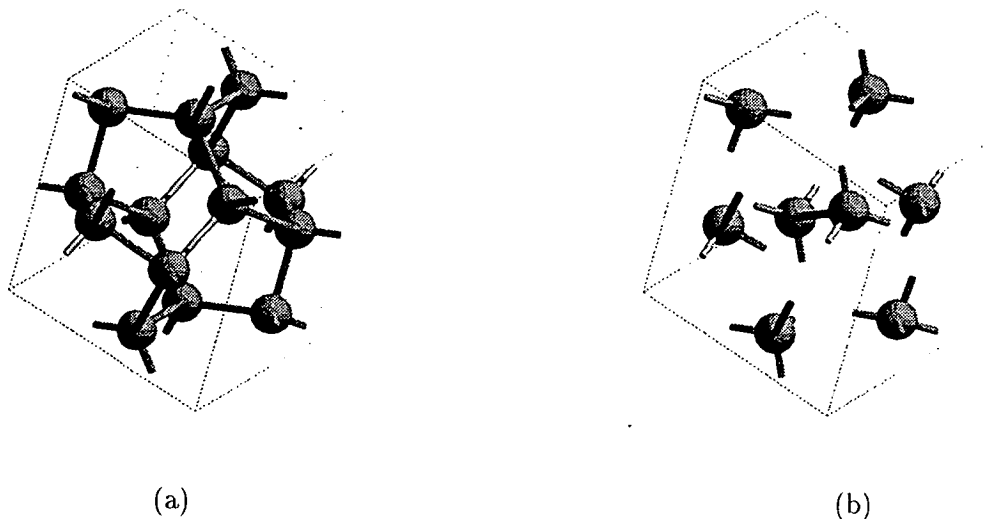
than the constrained bond compression of Si-III.

<div align="center">(a)   (b)</div>

Figure 4.11. The rhombohedral structures of (a) Si-III and (b) Si-XII are shown here.

4.4.4   Pressure dependence of Si R8

Full Rietveld refinements of Si-XII were possible on the down-stroke, from 82(2)kbar down to 28(1)kbar, and on the up-stroke at 27(1)kbar. A typical refinement of Si-XII is given in figure 4.12, from a pattern taken at 28(1)kbar on the down-stroke (R_{wp}=13.97%). The structural parameters for Si-XII at this pressure are given in Table 4.3, along with the refined structural parameters from a pattern taken at 27kbar on the up-stroke from ambient pressure. These results are very interesting, in that they show the reversibility of the Si-III to Si-XII transition, by the similarity in the structural parameters.

However, from all the refinements of Si-XII, it was found that the internal positional parameters did not change appreciably from the mean values of u=0.291(2), x=0.462(4), y=−0.031(5) and z=0.269(3). From the limited intensity accuracy of the data collected, it was not possible to distinguish between these mean values and values refined by least-squares analysis. Therefore, bond-length and bond-angles do not alter

Parameter	28kbar, down-stroke	27kbar, up-stroke
$a(Angstroms)$	5.696(4)	5.690(4)
$\alpha(°)$	109.99(4)	109.95(4)
u	0.291(2)	0.291(2)
x	0.462(4)	0.462(4)
y	-0.031(5)	-0.031(5)
z	0.29(3)	0.269(3)

Table 4.3. The similarity in the structural parameters for these two patterns show the reversibility of the XII–III transition.

much under pressure. The variations [75] with pressure are shown in figures 4.13(a) and 4.13(b), merely to illustrate the increased complexity of the Si-XII structure, the implications of which will be discussed later.
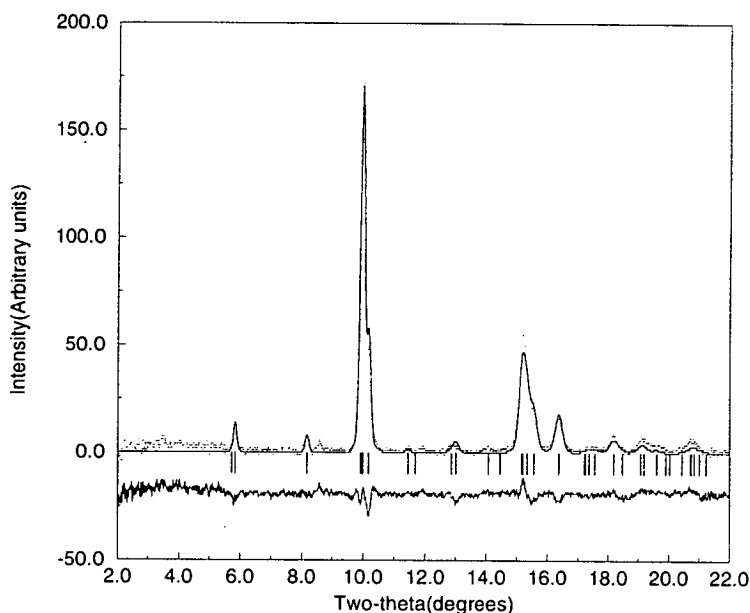

Figure 4.12. A Rietveld refinement of Si-XII at 28kbar. The dots are the experimental pattern, the solid line is the calculated profile and the line below the diffraction pattern shows the difference between the two. Tick marks show where all the reflections are.
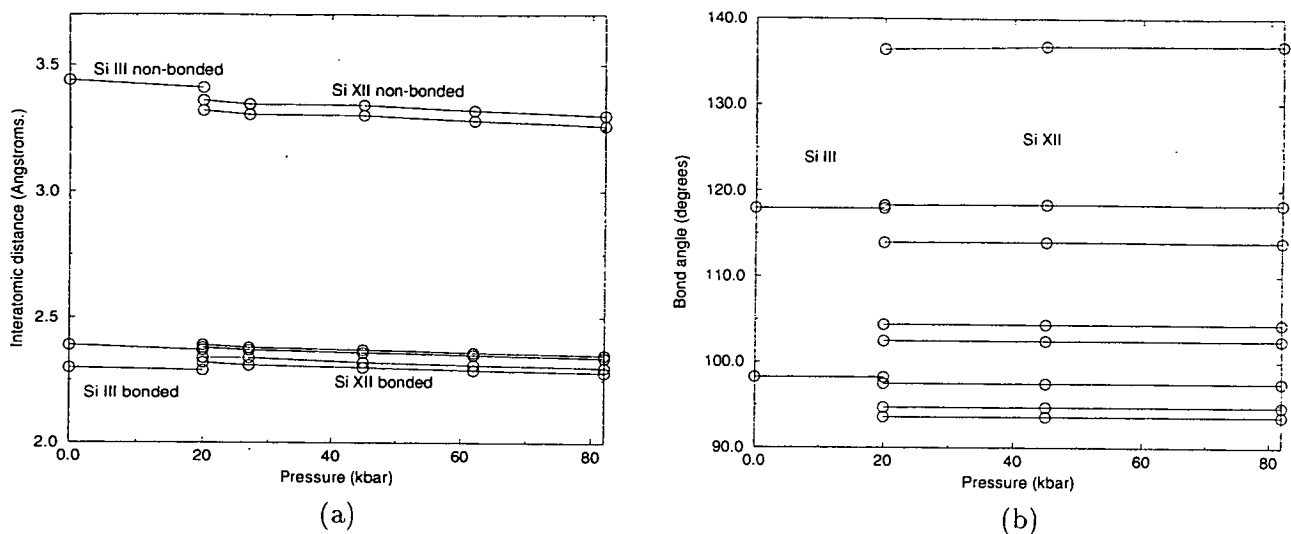
(a)   (b)

Figure 4.13. The variation of inter-atomic distances (both bonded and non-bonded atom pairs) against pressure is shown in (a), and the variation of bond-angles against pressure is given in (b). These two diagrams show the increased degree of complexity in Si-XII as opposed to Si-III.
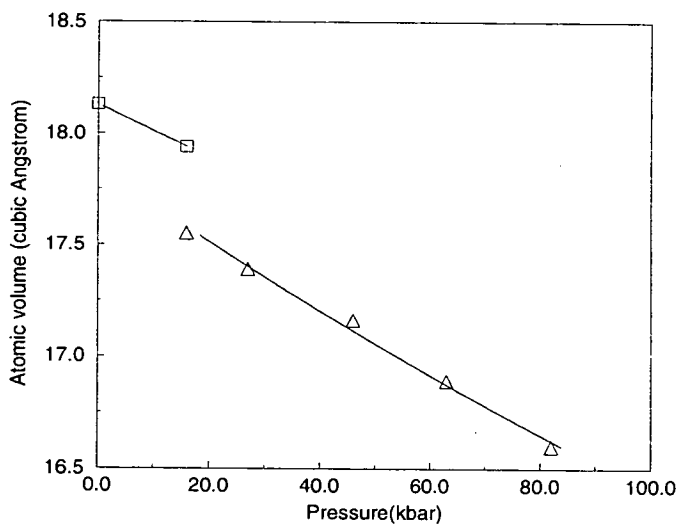

Figure 4.14. The change in the volume per atom with pressure for Si-III and Si-XII proves the first-order nature of the phase transition. The solid line is a fit to the experimental data points using the Birch equation of state.

The volume change with pressure is shown in figure 4.14, with the simultaneous

refinement of Si-III and Si-XII at 16kbar on the down-stroke clearly showing the first-order nature of the phase transition. From the fit of the data to the Birch equation of state [76], the bulk moduli of Si-III and Si-XII were calculated to be 1200(100)kbar and 960(50)kbar, respectively.

4.4.5 Transition mechanisms

The type of transition mechanism which occurs during the phase transition from the high pressure Si-II (β-tin) phase to the Si-XII (R8) phase was analysed in detail in Ref. [66], but the basic results obtained are summarised below.

A model for the transition route between Si-II and Si-XII was formulated, involving a nucleation and growth mechanism. This transition mechanism requires the existence of a set of planes in the parent phase to be commensurate with a set of planes in the daughter phase. This then provides a "pivotal point", around which the atoms can move to form one structure from the other structure.

By considering all low-index (hkl) planes of Si-II, supercells of Si-II and Si-XII containing sixteen atoms, were created which satisfied this condition. From these supercells, a computer searching algorithm was written to map atoms in one supercell to those in the other. The energetics of the most plausible atomic displacements were evaluated by calculating the distance of closest approach between atoms in the intermediate structures between the two supercells. From this simple concept, only two atomic mappings resulted in feasible distances, comparable to the shortest bond-length in Si-XII. All other mappings required shorter contact distances, which would be energetically less stable. However, detailed *ab-initio* electronic calculations are required to rule out any of the possible intermediate structures. The movement of atoms in the

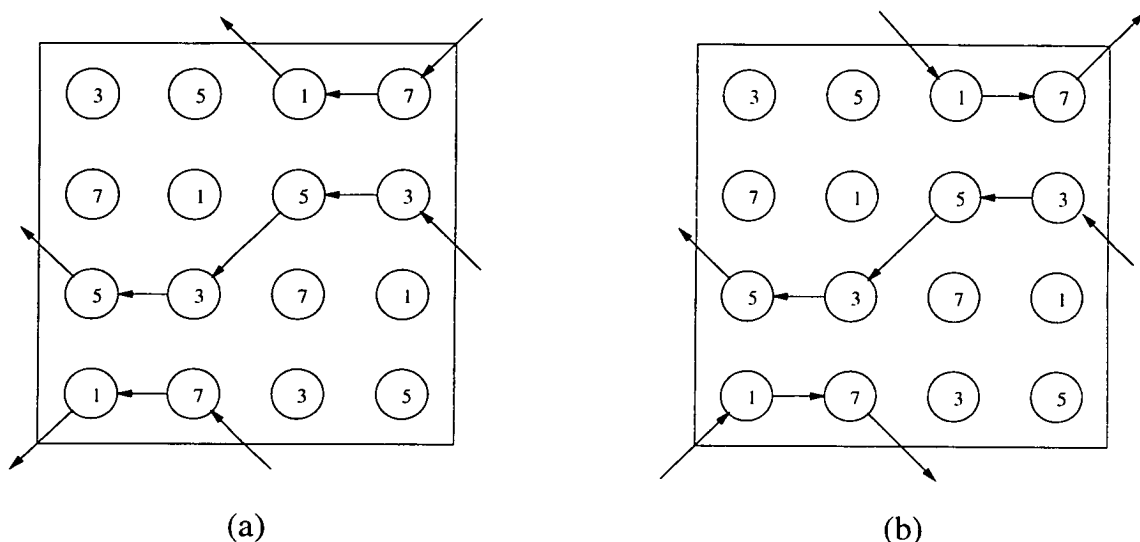two most feasible transition routes is shown in figure 4.15.

(a)   (b)

Figure 4.15. This figure shows the approximate change in the atomic fractional co-ordinates corresponding to the most plausible transition routes. The circle represents an atom in the Si-XII supercell, with the numbers corresponding to the value of the y co-ordinate in units of $\frac{1}{8}$. The arrows indicate the approximate change in x and z co-ordinates required to transform the Si-XII supercell into the Si-II supercell.

4.5   Conclusion

Using angle-dispersive x-ray powder diffraction with image-plate area detection, a new phase of silicon, Si-XII, has been observed. From experiments conducted on both the up-stroke and down-stroke of pressure, this phase has been proven to be reversible, and from the volume per atom at various pressures, the transition between Si-XII and Si-III to be of a first-order nature.

The importance of the structure of Si-XII has been demonstrated recently by *ab-initio* psuedopotential calculations on carbon [77]. Results of this study have revealed R8 to be a stable high pressure structure in carbon, existing at elevated pressures beyond the ambient pressure diamond phase. This means the pressure that diamond-anvil cells can reach is limited to about 5Mbar. Experiments have yet to prove these

theoretical calculations.

Figure 4.13 demonstrated the complexity of Si-XII. Indeed it is the most complex structure observed to date occurring in any tetrahedral network of atoms. Thus, the R8 structure may be a very useful model in calculations of the properties of amorphous silicon. The BC8 structure has already been used in calculations of the vibration properties of amorphous tetrahedral semiconductors, the results of which are reviewed by Joannopoulos and Cohen [78] and Alben *et al* [79]. The increased complexity of the R8 structure may provide a valuable insight into materials of this type.

Chapter 5

An *ab-initio* theoretical study of CuCl

The structural and electronic properties of high pressure phases of CuCl are presented here. Total energy calculations using the Full Potential Linearised Plane Wave method (FP-LAPW) were performed, with most interest given to the simple cubic structure existing between the ambient pressure face-centred, and the high pressure body-centred cubic structures. This intermediate structure (called SC-16), the binary analogue of the BC8 structure seen in Si-III, was first predicted to be a stable high pressure form in group III-V compounds, but was seen for the first time in this group I-VII copper halide.

My contribution to this work was all the total energy calculations using the FP-LAPW method. This comprises all of the results presented in this chapter. However, at the time the work was being carried out, parallel calculations were performed by Dr. H-C Hsueh using the psuedo-potential method to compare the two techniques, as well as obtaining the maximum amount of information about the SC-16 phase.

5.1 Background

The group I-VII copper halide compounds CuX,(X=Cl,I,Br), are the most ionic of the iso-electronic, eight valence electron compounds. Relative ionicities in the $A^n B^{8-n}$ compounds have been quantified in terms of quantum mechanical terms, which can be related to spectroscopically defined variables, by the Phillips-van Vechten ionicity [3]. The Phillips (Phillips-van Vechten) scale comes from a method to calculate the dielectric constant which, for eight valence electron materials, involves a parameter describing the charge transfer, $C_{\alpha\beta}$, between two different atom types, α and β. This charge transfer parameter is defined to be

$$C_{\alpha\beta} = \left(\frac{Z_\alpha e^2}{r_{\alpha 0}} - \frac{Z_\beta e^2}{r_{\beta 0}} \right) f_{\alpha\beta},$$ (5.1)

where Z is the atomic number, e is electronic charge, and $r_{\alpha 0}$ and $r_{\beta 0}$ are the equilibrium radii of the atoms α and β respectively. The parameter $f_{\alpha\beta}$ in equation 5.1 represents Thomas-Fermi screening, and can be used to measure the degree of ionicity in the zinc-blende structure. If $f_{\alpha\beta} = 1$, then purely ionic bonding would result, with the bare ions Z_α and Z_β exchanging charge. However, as covalency increases, f will decrease and screening will become more dominant as electron density builds between the ions.

By plotting the position of group IV elements and iso-electronic compounds on a graph using axes describing the homopolar energy gap (E_h) and the difference between the homopolar and heteropolar energies ($C_{\alpha\beta}$), a clear line can be drawn separating elements and compounds adopting the zinc-blende and rocksalt formations. This critical value of $f = 0.785$ marks the stability boundary between the zinc-blende structure and the rocksalt structure (these structures are described in detail in the next section). The group IV elements, such as Si and Ge are the most covalent, with relative ionicity increasing up to that of the CuX compounds, which have values of $f \approx 0.7$. This is approaching the stability boundary between four and six-fold coordination.

The copper halides differ from the other group IV, III-V and II-VI tetrahedral

semiconductors in the nature of their bonding. The $3d$ core electrons in the copper atoms have a similar energy to the p-like valence electrons in the halogen, which creates a strong hybridisation. This means the number of valence electrons increases from 8 to 18, producing interesting effects such as a negative spin-orbit splitting of the uppermost valence band in CuCl [80].

Among the copper halides, much experimental interest has been devoted to CuCl, as evidence for a superconducting phase was observed at low temperature (100 - 170K) and moderate pressures ($\approx$5kbar) [81]. Strong diamagnetic anomalies were reported, implying a Meissner effect, which would be a pre-cursor for a superconducting state. This was supported by a sharp drop in resistivity at ambient temperature at about 40kbar, showing an insulator $\rightarrow$ metal transition [82] occurring within the zinc-blende phase.

The evidence for this superconducting state, however, was unsupported by various other research groups [71, 83], with neutron and optical resistivity experiments showing no insulator $\rightarrow$ metal transition. The "irreproducibility" is thought to be due to a mixture of possible effects such as impurities, non-hydrostatic pressure environments, or sample preparation differences. The disproportionation of cuprous chloride (Cu-I) into copper metal and cupric chloride (Cu-II) (2CuCl $\rightarrow$ Cu + $CuCl_2$) was also thought to be a reason for the drop in resistivity, but this would lead to a 3% collapse in volume, and hence would be the more stable structure under high pressure instead of the zinc-blende phase.

In order to investigate the claims of an insulator $\rightarrow$ metal transition at 40kbar, and also to prove the stability of an intermediate high pressure phase, occurring between the zinc-blende and rocksalt structures observed at ambient temperature, total energy calculations were performed. The FP-LAPW method (detailed in chapter 3) offers an accurate way of coping with the large number of valence electrons in the CuCl crystal system. The fact that core electrons are treated exactly by a few spherical harmonics deals with the deep atomic potentials, requiring only moderate amounts of interstitial

plane waves to adequately describe the whole potential in the unit cell. This is in contrast to calculations involving the pseudopotential method, where only plane-waves are used to simulate the wavefunction of all electrons, acted upon by a modified core potential. However, pseudopotential calculations were performed on CuCl in unison with these FP-LAPW calculations [84], giving comparable results between both methods and the experimental observations.

5.2 Structural details

5.2.1 The ZnS-type structure

All three copper halides CuX,(X=Cl,I,Br) adopt the four-fold co-ordinated ZnS (zinc-blende) structure at ambient pressure. This is the binary analogue of the diamond structure observed in other group IV elements, such as Si and Ge. The spacegroup of zinc-blende is $F\bar{4}3m$, with Z=4. Each atomic species occupies the sites of two interpenetrating fcc sub-lattices displaced by one quarter along the crystallographic (111) direction (see figure 5.1). This structure is one of the three most plausible structures for an ionic solid to adopt*.

5.2.2 The SC16 structure

Under a pressure of about 55.2(2)kbar, CuCl transforms to the binary analogue of the BC8 structure, which both Si and Ge have been shown to adopt. In Si, this cubic structure is body-centred, but when two atom species are placed in this setting, the only way to arrange the atoms with one atom-type surrounding the other is to lose the body-centred symmetry operation, hence becoming simple. For this reason, the phase

---

*The other two structures are close-packed hexagonal and body-centred cubic [6].

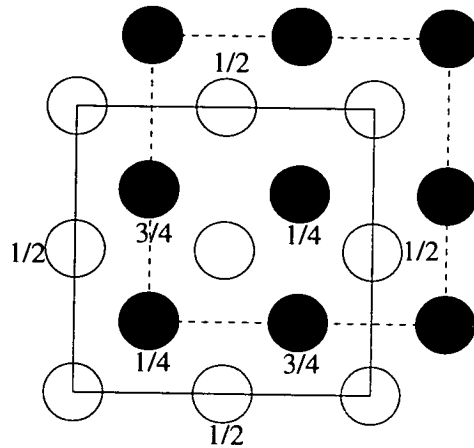is known as SC16 (simple-cubic with 16 atoms in the unit cell, *i.e* eight formula units).

Figure 5.1. The zinc-blende structure can be thought of as being composed of two inter-penetrating, face-centred cubic sub-lattices of each atomic species, displayed as white and black spheres in the diagram. The diagram shows a projection along the (001) direction, with the fractions next to the atoms being their respective fractional heights along this axis.

This structure has been predicted to be a stable high-pressure polymorph of other III-V compounds, such as GaAs, AlAs and InAs [70], but this has not yet been experimentally observed. It was also proposed that the formation of this structure was inhibited in these more covalent compounds by the phase transition mechanism. The R8 structure observed in silicon, detailed in the previous chapter, offers a possible route to this structure which would be energetically unfavourable for bivalent compounds, due to the odd-membered rings (and hence like-atom bonding). A three-dimensional

For an isothermal system change, the second term in equation 5.5 drops out (since $dT=0$). Since the total energy calculations are performed at zero Kelvin (the adiabatic approximation), $T=0$, so the first term also drops out, leaving only the final term.

$$dU = -PdV \Rightarrow P = -\frac{dU}{dV} \tag{5.7}$$

Thus, the instantaneous pressure of the crystal may be obtained from the gradient of a plot of total energy against volume. The common tangent between phases will therefore be the pressure at which one structure transforms into the other.
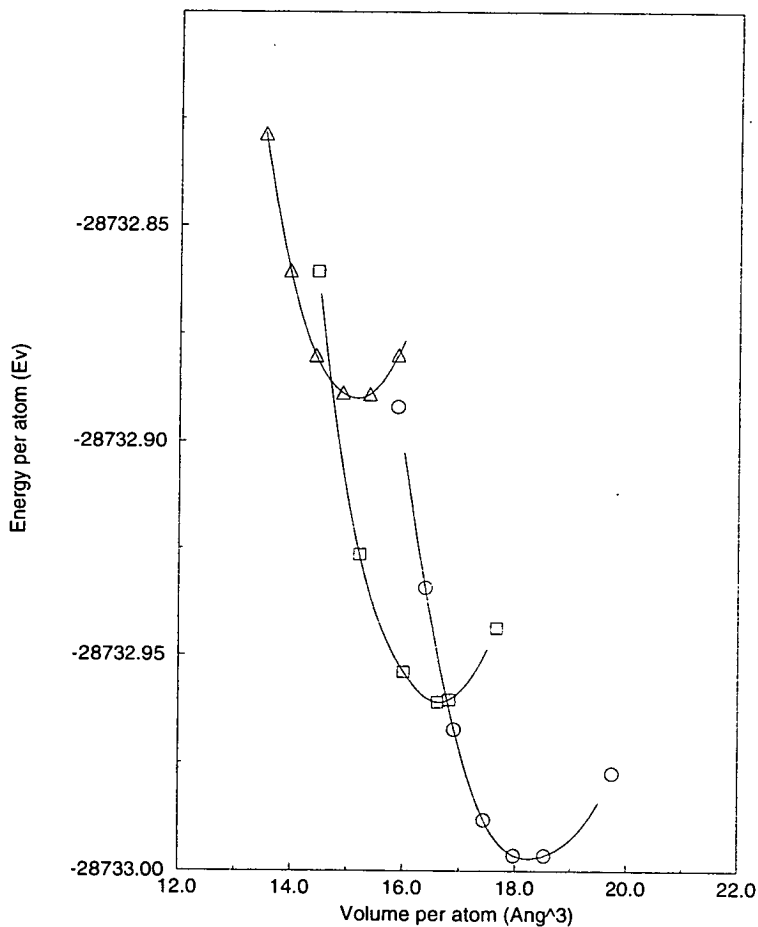

Figure 5.4. The total energy curves for the zinc-blende (circles), SC16 (squares) and rocksalt (triangles) structures are shown. Physical properties, such as the transition pressure, equilibrium volume and compressibility can be deduced from these curves.

From the total energy curves, the structural parameters for, and transition pressures

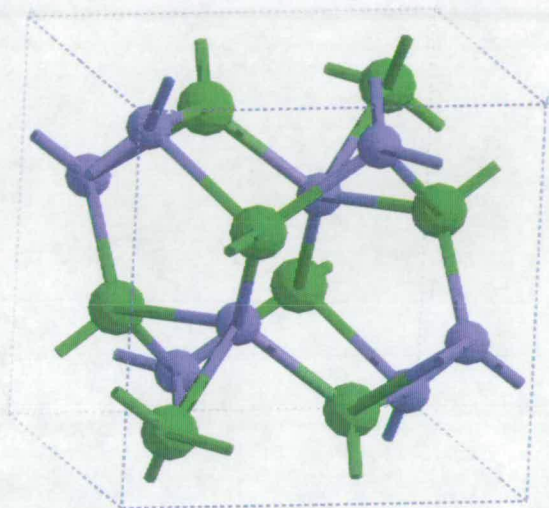image of the SC16 structure is shown in figure 5.2.

Figure 5.2. The SC16 structure is a complex tetrahedral network of atoms, shown above with dashed lines defining the unit-cell edges. The green spheres are Cl atoms, and the blue spheres are Cu atoms.

The spacegroup of the SC16 structure is $Pa\overline{3}$, with 16 atoms in the unit cell. Each atomic species are on the 8(c), (x, x, x) sites.

5.2.3 The NaCl-type (rocksalt) structure

The next phase transition occurs in CuCl at 104.9(4)kbar, which is another solid-solid transition to the rocksalt structure. This six-fold co-ordinated, face-centred cubic structure can also be described in terms of two inter-penetrating fcc sub-lattices, but now displaced by one half along the crystallographic (111) direction (see figure 5.3). This classic structure, adopted by most metallic compounds has spacegroup $Fm\overline{3}m$,

with atoms on the 4(a) (0,0,0) and the 4(b), $(\frac{1}{2}, \frac{1}{2}, \frac{1}{2})$ sites.
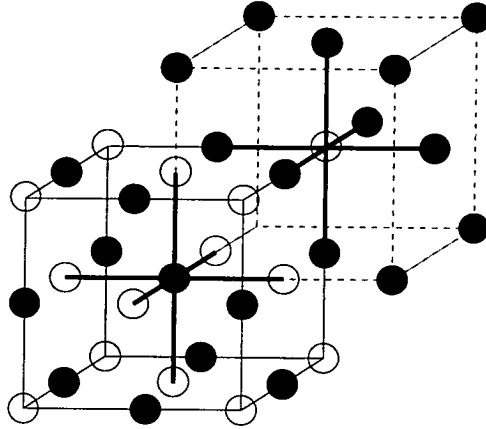

Figure 5.3. The rocksalt structure of CuCl is one of the most common structures adopted by metallic and high pressure materials. The structure can be described by two inter-penetrating fcc sub-lattices, displaced relatively by $(\frac{1}{2}, \frac{1}{2}, \frac{1}{2})$.

5.3 Computational details

The FP-LAPW calculations were performed using the Vosko-Wilk-Nussair [49] form of the exchange and correlation potential, which has proven to be a reliable parameterisation for group III-V compounds [85]. Brillouin zone sampling for the zinc-blende, SC16 and rocksalt structures involved sets of 10, 4 and 56 special k-points. The core electrons were treated fully relativistically by solving the Dirac equation with relativistic effects, such as the mass-velocity and Darwin terms included, and spin-orbit coupling introduced later as a perturbation term. The calculation of valence states did not include spin-orbit coupling. This is the so-called "scalar-relativistic approximation"[86].

The muffin-tin sphere radii were 1.06Å for both Cu and Cl. Inside the muffin-tin spheres the wave functions, charge densities and potentials were expanded in spherical harmonics up to an angular momentum cutoff of $L_{max}=12$ for the wave functions and $L_{max}=6$ for the charge densities and potentials.

Since relaxation of the atomic positions under Hellman–Feynman [87] forces had not been implemented in the FP-LAPW code used, the two atomic positional parameters in the SC16 structure were optimised only at the calculated equilibrium volume. To optimise the atomic parameters, the total energy was calculated at six different values of x_{Cu} and x_{Cl} centred around the experimentally observed values, and a contour plot was used to find the minimum value within this range. The calculated and experimental atomic positions are shown in Table 5.1. These values were then used at all subsequent volumes, since the dependence upon pressure shown by both parameters was experimentally observed to be small[†] [71].

Parameter	Experimental	Calculated	% difference
x_{Cu}	0.6297(3)	0.6320	0.23
x_{Cl}	0.1527(3)	0.1525	0.02

Table 5.1. The calculated and experimental atomic positional parameter for Cu and Cl used in the FP-LAPW calculations are tabulated. The experimental values were obtained from a Rietveld refinement of neutron powder diffraction data, collected at 55.2kbar (the transition to the SC16 structure proceeds at a pressure of 51(1)kbar).

5.4 Computational results

5.4.1 Structural

For all three structure types, the total energy was calculated at a set of lattice parameters, which included the experimentally observed lattice parameter. This produced a smooth curve with a positive second derivative, the minimum of which is the equilibrium lattice constant for that structure. The computed curves for CuCl in all three phases are shown in figure 5.4.

By fitting the points on each curve to the Murnaghan equation of state [88], the

---

[†]Under pressure, x_{Cu} does not vary within the error given in Table 5.1, and Cl changes by only 0.13% between the CuCl-II→CuCl-IV and CuCl-IV→CuCl-V transitions.

bulk modulus (B_o) and equilibrium volume (V_o) were obtained. The total energy, E as a function of volume, V, defined by the Murnaghan EOS is given in equation 5.2.

$$E(V) = \frac{B_o V}{B_o'(B_o' - 1)} \left[B_o' \left(1 - \frac{V_o}{V} \right) + \left(\frac{V_o}{V} \right)^{B_o'} - 1 \right] E_o, \tag{5.2}$$

where B_o' is the pressure derivative of B_o and the equilibrium energy $E_o = E(V_o)$.

From the first law of thermodynamics, the internal energy of a system is characterised by a combination of the kinetic and potential energy of each particle contributing the whole system. This is directly analogous to the total energy calculated for the crystal in this case. The second law gives us expressions to relate physical properties, such as pressure, volume and temperature. For both reversible and irreversible systems, the following relation holds true.

$$dU = TdS - PdV, \tag{5.3}$$

where dU is the infinitesimal change in internal energy brought about by changes in entropy, dS and volume, dV, under external pressure P and temperature T. Differentiation of S with respect to V gives an expression for dS as

$$dS = \left(\frac{\delta S}{\delta V} \right)_T dV + \left(\frac{\delta S}{\delta T} \right)_V dT, \tag{5.4}$$

so equation 5.3 becomes

$$dU = T \left(\frac{\delta S}{\delta V} \right)_T dV + T \left(\frac{\delta S}{\delta T} \right)_V dT - PdV \tag{5.5}$$

From the Maxwell relation, $\left(\frac{\delta S}{\delta V} \right)_T = \left(\frac{\delta P}{\delta T} \right)_V$, derived from the Helmholtz free energy, equation 5.5 can be re-written as

$$dU = T \left(\frac{\delta P}{\delta T} \right)_V dV + T \left(\frac{\delta S}{\delta T} \right)_V dT - PdV. \tag{5.6}$$

For an isothermal system change, the second term in equation 5.5 drops out (since $dT=0$). Since the total energy calculations are performed at zero Kelvin (the adiabatic approximation), $T=0$, so the first term also drops out, leaving only the final term.

$$dU = -PdV \Rightarrow P = -\frac{dU}{dV} \tag{5.7}$$

Thus, the instantaneous pressure of the crystal may be obtained from the gradient of a plot of total energy against volume. The common tangent between phases will therefore be the pressure at which one structure transforms into the other.
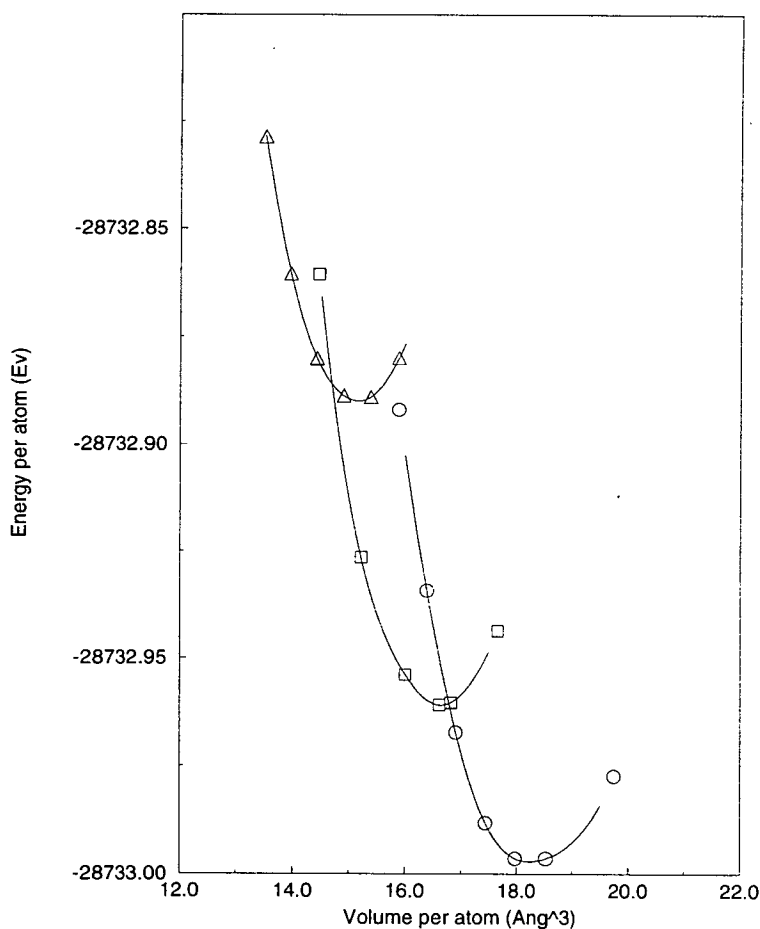

Figure 5.4. The total energy curves for the zinc-blende (circles), SC16 (squares) and rocksalt (triangles) structures are shown. Physical properties, such as the transition pressure, equilibrium volume and compressibility can be deduced from these curves.

From the total energy curves, the structural parameters for, and transition pressures

between, all three phases have been calculated and compared to the experimentally observed results in Table 5.2.

Description	$a_o(\text{Å})$		$B_o(\text{kbar})$		$P_t(\text{kbar})$	
	FP-LAPW	Expt.	FP-LAPW	Expt.	FP-LAPW	Expt.
Zinc-blende	5.273	5.4202(2)	756	381(6)	-	-
SC16	6.421	6.4162(3)	839	660(1)	37	55.2(2)
Rocksalt	4.893	4.9290(8)	927	-	87	104.9(4)

Table 5.2. Calculated structural parameters for the zinc-blende, SC16 and rocksalt phases of CuCl are compared against experimentally observed values here.

Comparing theory with experiment, the first discrepancy to note is in the predicted transition pressures for both the SC16 and rocksalt phases (*i.e* the transition pressure between the zinc-blende and SC16 phase, and between the SC16 and rocksalt phase, respectively). They are both computed to be lower than was actually observed in the recent neutron experiments [71]. The experimental values given were only taken on the up-stroke of pressure, so hysteresis effects may act to increase the actual experimental value, but this effect would be expected to be small.

A possible reason for the difference could be that the SC16 phase is formed in small localised areas in the crystal at lower pressures than are experimentally observed, which then spreads throughout the crystal. The long-range crystallographic order probed by neutrons would not pick up on the small clustering of SC16 crystallites within the zinc-blende phase.

However, by far the most dominant factor is the temperature dependence of the transition pressure. All the FP-LAPW calculations were performed using the adiabatic approximation, hence at zero Kelvin, but the experiments were conducted at room temperature ($\approx$300K). When the phase diagram of CuCl is studied [89], it can be seen that the calculated transition pressures become consistent with experimental values (see figure 5.5). These findings have been supported by the observation of the luminescence peak from the SC16 phase at a pressure of 40kbar at 6K [90], the occurrence of which

was at first assumed to be produced by a tetragonal crystal structure [82, 91].

The calculated equilibrium volumes are smaller than the experimentally observed values, except for the SC16 structure. As well as this, the bulk moduli are calculated higher than expected. This is due to an accepted limitation with the local density approximation used in the FP-LAPW and other total energy calculations. The result of effectively averaging the electron-electron interaction, by assuming a constant local electronic charge density acting on each individual electron, has an over-binding effect. This causes inter-atomic distances to be reduced (hence lowering equilibrium volumes), which decreases the compressibility (or increases the bulk modulus). However, the magnitude of the discrepancy observed in these computations are within the accepted tolerance for calculations of this kind, which is about 5%.
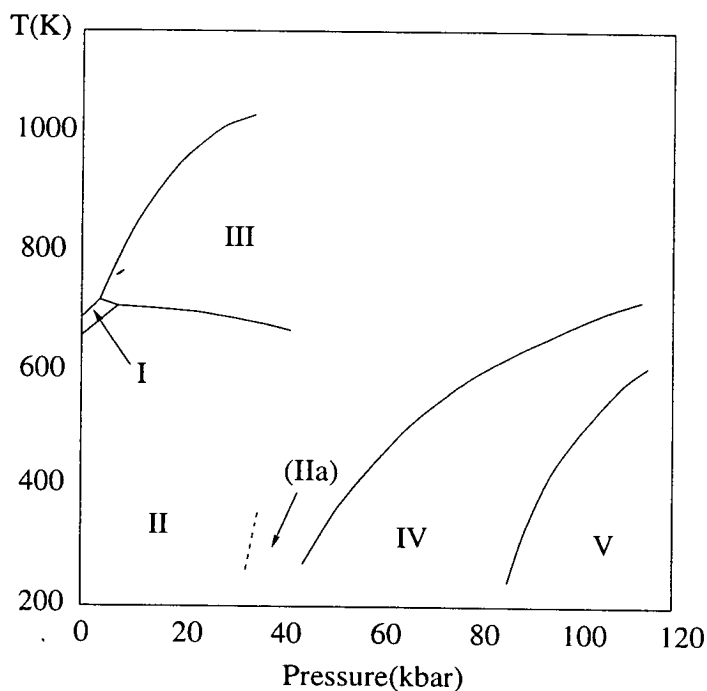

Figure 5.5. A schematic reproduction of the phase diagram of CuCl is shown here. The phase labelled IIa in brackets represents the unconfirmed phase obtained after the proposed insulator → metal transition.

5.4.2 Electronic

Inherent in the calculation of total crystalline energy is the computation of electronic energy levels. Along with this, the Fermi energy must be calculated to determine the occupancy of each band. When the energy of the whole system is required, the distribution of k-points sampled in the Brillouin zone is organised such that the maximum amount of information is obtained from the least number of points. However, when an electronic band structure is desired, the k-point set should be placed along particular directions of interest in the Brillouin zone. This was done for all three phases in CuCl to determine the electronic nature of each phase. As can be seen from figure 5.6, the band structure of the zinc-blende phase was calculated along the $X \to \Gamma$ and $\Gamma \to L$ directions in the Brillouin zone. There is a clear direct energy gap at the Γ point (coupled with the fact that the Fermi energy coincided with the top of the valence band), indicates that this phase is insulating. Table 5.3 details the progression of the direct band-gap under varying amounts of external pressure for the zinc-blende phase, as well as the energy difference between the top of the valence band and the Fermi energy. As can be seen, for all pressures up to the experimentally observed phase transition there is no closure of the energy gap, and the Fermi energy does not rise above the bottom of the conduction band, as would be required in an insulator-to-metal type transition. These results add to the growing doubts about the existence of a superconducting phase (named IIa) in CuCl.

Unit-cell length (a.u)	Pressure(kbar)	E_c-E_v(Ryd)	E_F-E_v(Ryd)
9.9645	0.0	0.05(1)	-0.00(1)
9.9	42(5)	0.05(1)	-0.01(1)
9.8	149(5)	0.06(1)	-0.01(1)

Table 5.3. The direct energy-gap (E_c-E_v) of CuCl in the zincblende phase remains the same under pressure, with the Fermi energy lying on the top of the valence band (within computational uncertainty). This situation remains even beyond the experimentally observed transition pressure of 55kbar.
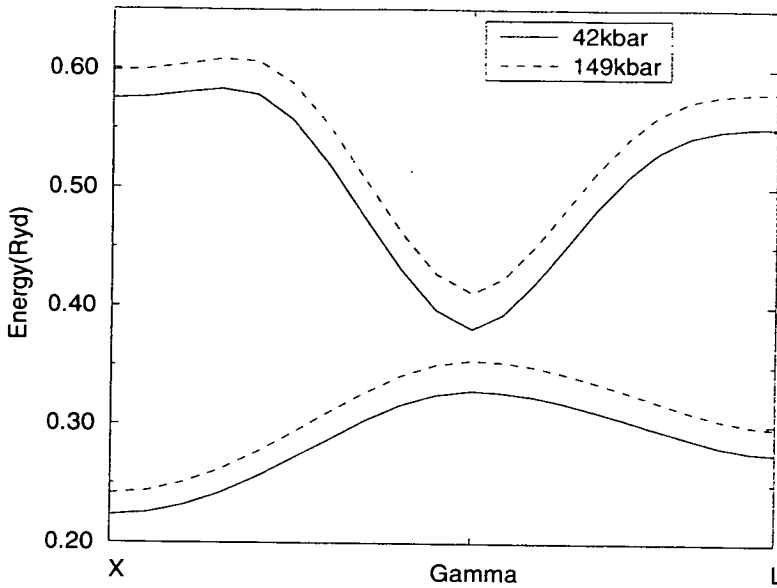
Figure 5.6. The top of the valence band and the bottom of the conduction band is plotted here for CuCl in the zinc-blende phase at 42kbar and 149kbar. As can be seen, under pressure the direct energy gap remains, even beyond the transition pressure at 55kbar.

Figures 5.7(a) and 5.7(b) show the band structures obtained for the SC16 and rocksalt phases. Again, both these phases are shown to be insulating, with an indirect energy gap in the rocksalt phase between the L and X points and a direct gap at the Γ point for the SC16 phase. These results are consistent with experimental evidence using the sharpness and definition of the absorption edges [92], and from electrical studies [93], which showed no evidence for a metallic phase up to 120kbar. Similar calculations performed using an LMTO (Linear-combination of Muffin-Tin Orbitals) method have been reported by Ves et al. [80], which also agree with the present findings. The results are summarised in tabular form below, along with the values for the energy gaps calculated with the LMTO method.

Structure	FP-LAPW method (eV)	LMTO method (eV)
ZB direct gap	0.7	0.5
SC16 direct gap	0.5	-
Rocksalt indirect gap	0.6	0.6

Table 5.4. The results of the present calculation using the FP-LAPW method and previous values obtained from an LMTO method are compared. At the time of the LMTO calculations, the structure of the SC16 phase was not known, and was not included in the analysis.

(a)   (b)
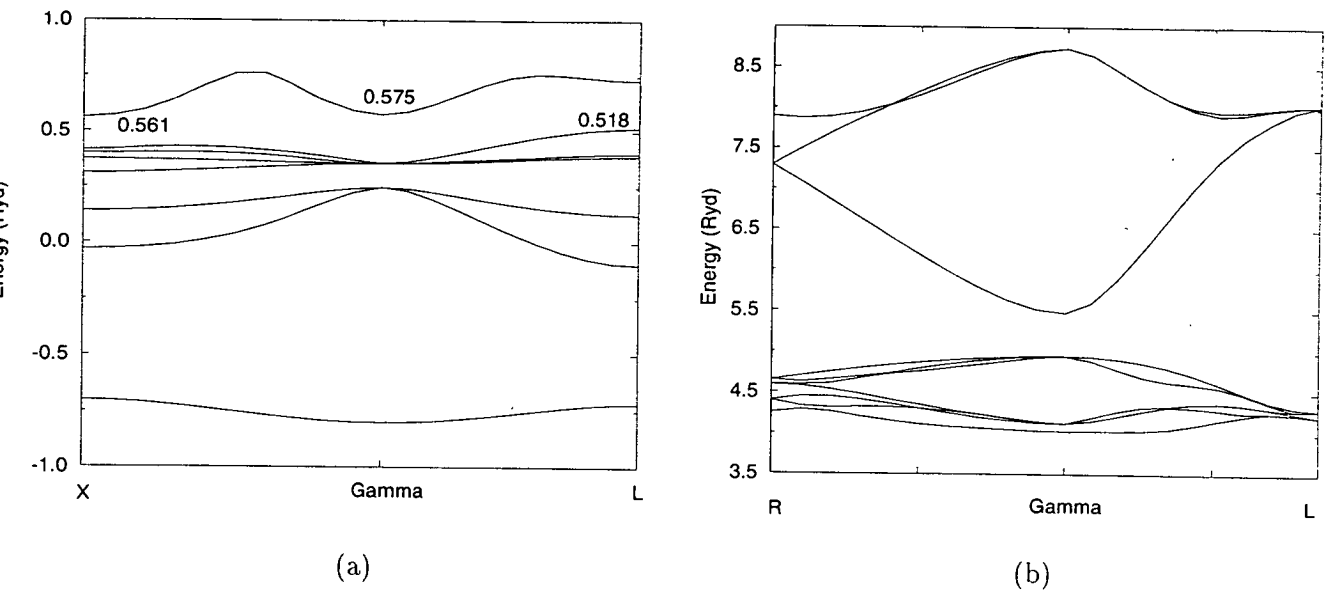
Figure 5.7. An indirect energy gap of 0.6eV, between the L and X points of CuCl in the rocksalt structure (a), shows that this phase is insulating. A direct energy gap can also be observed in the band structure for the SC16 phase (b). The numbers on the band structure diagram for rocksalt are the energy at the X and Γ points on the conduction band, and the L point at the top of the valence band.

5.5   Conclusions

Comparison with the experimentally observed structural and electronic properties of all three phases investigated, shows that the FP-LAPW technique is very adept at

handling such large atomic systems. This gives confidence to future computations of this nature, and enables predictions which are unsubstantiated by experimental findings to be taken seriously. Such "sanity checks" are always useful when first-principles methods are applied.

The results obtained in this chapter for the SC16 structure of CuCl represent the largest ever full-potential calculation undertaken to date. Although 16 atoms may not sound very impressive, when the degree of ionicity in the structure is considered (which increases the electronic kinetic energy around the ions), along with the large numbers of electrons in the system, the complexity of the computation can be fully appreciated.

Issues involving the superconductivity of CuCl under pressure were also been explored. By analysing the change in the direct energy gap of CuCl in the zinc-blende phase as pressure was applied, no evidence could be seen of either band-gap closure or band overlap, which would lead to a sudden drop in the resistivity due to electrons filling the conduction band. Hence, according to the FP-LAPW results, other factors appear to have been the cause for the experimentally observed conductivity changes.

The FP-LAPW method has thus proven to be a useful technique for handling structures involving large numbers of valence electrons, which causes problems for computational methods utilising the powerful properties of plane-waves. However, when dealing with systems where large ions (i.e atoms with large atomic numbers, such as Pb), the chosen method must compute the Schrödinger equation fully relativistically, using the Dirac formulation. This problem was encountered when calculations of the structural and electronic properties were attempted for the other Cu-halides, CuBr and CuI. The increase in atomic number from 17 for chlorine to 35 for bromine and 53 for iodine meant that electronic energies were approaching the limit where relativistic effects, such as spin-orbit coupling, became noticeable. Although total energy curves for CuBr and CuI were obtained for the zinc-blende phase and higher pressure phases in CuI (the SC16 phase and a tetragonal phase, spacegroup $P4/nmm$, with Z=2), the calculated bulk moduli and transition pressures were much lower than the experimentally observed

values (as much as 50% for the bulk modulus calculated for CuBr in the zinc-blende phase).

These poor results may be improved by increasing the size of the muffin-tin radius used for each atom, allowing more of the electronic wavefunctions to be described by spherical harmonic, thus reducing the need for as many plane-waves. This will also reduce the size of the Hamiltonian matrix in the total energy calculations, improving computation times. Increasing the number of angular momentum components in the spherical harmonics used to describe the potential and electronic wavefunctions may also have a large effect. For CuI in the zinc-blende phase it was noted that increasing the cutoff value of L_{max} used in the wavefunction spherical harmonics, reduced the bulk modulus, but improved the shape of the total energy curve. These effects must be explored further to deduce the implications on the total energies obtained by altering such factors.

Chapter 6

High pressure forms of group V elements

Using x-ray powder diffraction and image-plate data collection, crystal structures of high pressure phases of the group V elements Sb and Bi were investigated. Much attention was devoted to the solution of a crystal structure common to both Sb and Bi under pressure. Previous reports have given evidence to support a tetragonal structure, but additional reflections not consistent with orthogonal axes were observed. Instead, a monoclinic distortion to the tetragonal structure produces reflections at the correct scattering angles, evidence for which is presented here. Attempts to refine this structure were, however, hindered by the presence of preferred orientation effects.

My contribution to this work was the collection and analysis of all diffraction patterns. This includes the modification of a Monte-Carlo analysis technique, originally written by Prof. Harris to solve crystal structures of organic materials from x-ray powder diffraction data.

6.1 Background

The group IV elements, such as Si or Ge, are considered to be the most ideally covalently bonded crystal structures, with four valence electrons being shared in an sp^3-hybridisation bonding configuration. As the number of valence electrons is increased to five, the bonding configuration exhibited by P, As, Sb and Bi becomes less covalent and more like that exhibited by the noble gases such as Xe and Ar, where the electronic configuration is of a stable closed-shell type. This "atomic crystal"-like* arrangement of atoms distorts the bond directionality in the group V elements, leading to many complex structures over a range of pressures and temperatures. Due to the distortion of bonds caused by the mixture of molecular and covalent bonding, high pressure structures adopted by As, Sb and Bi remained unsolved until only a few years ago.

The phase transition sequence of Sb is fairly simple. Rhombohedral Sb-I was thought to become simple-cubic in a first order phase transition at about 55kbar [94, 95, 96], but this phase has also been unresolved by several other researchers, such as those in references [97, 98, 99]. Beyond this supposed simple-cubic phase (named Sb-II), the structure formed by Sb-III has been indexed to be monoclinic [94, 100] at about 78kbar, which was then re-indexed [101] to be tetragonal. Most recently, this phase has been re-examined to give a completely different tetragonal structure [99], with atomic locations refined from observed intensities. Under increased pressure, this monoclinic/tetragonal structure has been observed to transforms into a body-centred-cubic phase (Sb-IV) [102]. It is evident that a full evaluation of the simple-cubic and monoclinic/tetragonal structures merit further work to elucidate the exact structures.

For Bi the situation is much the same, with the rhombohedral phase Bi-I becoming monoclinic Bi-II at 25kbar [103]. This transition has been studied in great detail,.

---

*Here, the term "atomic crystal" is used to denote materials such as the noble gases, where the electrons are localised around the ions.

and in fact is used as a pressure calibrant. Upon increased pressure. the same mono-clinic/tetragonal structures proposed for Sb have been observed, indexed and refined [94, 101, 104]. Bismuth also becomes body-centred-cubic at elevated pressures [105]. Once again, the structure of Bi-III needs careful evaluation. Although the structures of most of the phases have been confirmed by several research teams. a complete study of all the phases has never been published before.

This study aims to resolve several questions concerning the phase transition se-quence of Sb and Bi. The existence of Sb-II is examined, and the structure of both Sb-III and Bi-III is investigated. Finally, all the observed high pressure phases of Bi are presented in one complete study, showing the pressure dependence of all degrees of freedom within each structure.

6.2   Structural details

6.2.1   Rhombohedral phase I

At ambient pressure, As, Sb and Bi all adopt the same structure. The five valence electrons create a lone pair, which buckles the diamond structure (detailed in chapter 4 for Si), to create a rhombohedral structure, spacegroup $R\overline{3}$ with six atoms on the 6(c), $(0, 0, v)$ sites in the hexagonal setting, or two atoms on the 2(c), (v, v, v) sites in the rhombohedral setting. This rhombohedral structure can also be seen as a distortion of the simple-cubic structure, as shown in figure 6.1. The similarity between this rhom-bohedral structure and the rocksalt structure is important when considering the phase transition sequence observed in the lead chalcogenides, detailed in the next chapter.

As can be seen, the rhombohedral structure is made up of linear chains, with four different bond lengths, forming two inter-layer bonds and two intra-layer bonds. All four of these differing contact distances form the sides of the distorted simple-cubic structure. In fact, Sb was thought to become simple-cubic in a first-order transition
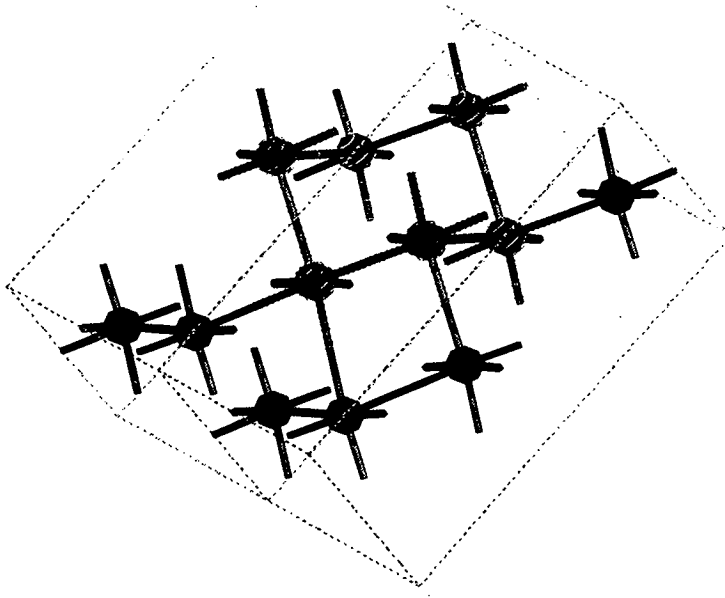
[94].

Figure 6.1. The rhombohedral structure adopted by arsenic, antimony and bismuth at ambient pressure can be viewed as a distortion of a simple-cubic cell. The hexagonal setting of Bi-I is shown here.

6.2.2   Bi-II: Monoclinic $C2/m$ structure

The second phase seen in Bi, but not in either As or Sb, is also a distortion of a simple-cubic cell [106]. This six-fold co-ordinated monoclinic structure has spacegroup $C2/m$ with 4 atoms in the unit-cell, adopting a connected, "almost planar" form [103]. The compressibility of this structure must be similar to that of the simple-cubic structure, as a result of the atomic arrangement. Being planar with near orthogonal bonding, shearing of atomic planes from anisotropic pressure gradients will occur easily, as is evident from the small stability region under pressure at room temperature (approximately 1kbar). Although this small stability region makes the phase difficult to find experimentally, there are large structural and electronic effects which indicate the transition has occurred. An almost 6-fold drop in resistivity accompanying the phase transition

[107], as well as a 5% volume reduction, enables this transition to be used as a pressure calibrant for high pressure experiments.
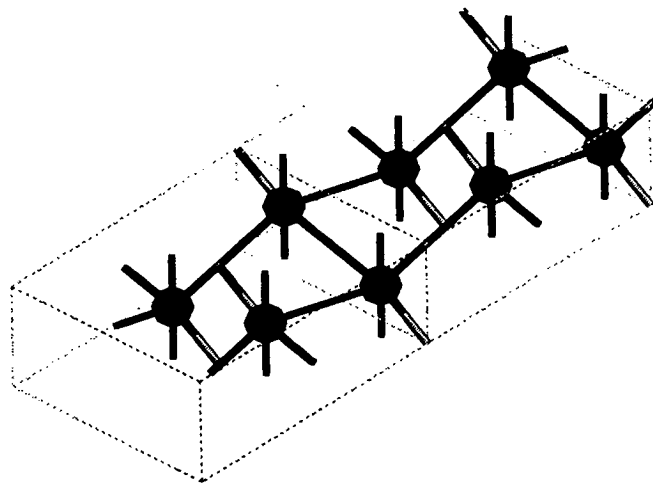

Figure 6.2. The monoclinic Bi-II structure shown here is also a distorted simple-cubic cell.

6.2.3 Tetragonal phase III

Both Sb-III and Bi-III adopt the same structure in the next phase of their pressure transition sequence. This can be seen from the similarity of their diffraction patterns, in terms of relative peak positions and intensities. For just over a decade, this structure has been shown to be a 10 atom tetragonal structure with spacegroup $P4/n$ in Sb [99], which was later solved for Bi-III [104], proving that the same structure is indeed adopted by the two elements. As can be seen from figure 6.3, this tetragonal structure

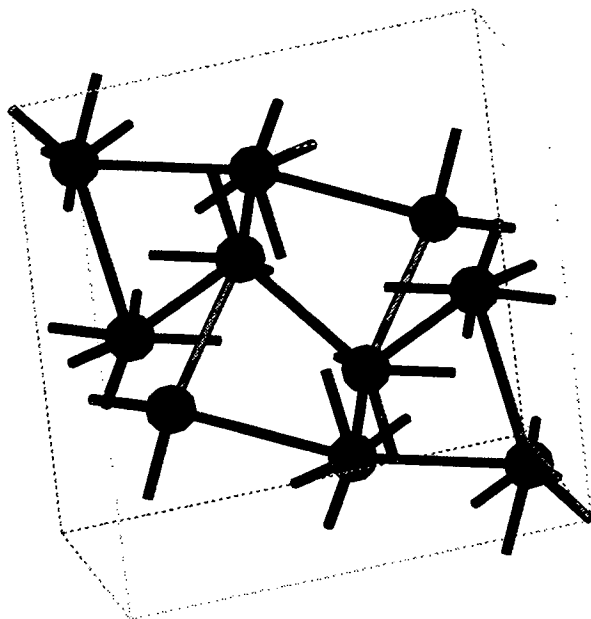is very complex, with 8-fold coordination running throughout the structure.

Figure 6.3. The 10 atom tetragonal structure adopted by both Sb and Bi is shown here for Bi.

6.2.4   The body-centred cubic (bcc) structure

The body-centred cubic form is also seen at higher pressure in both Sb and Bi. This cubic arrangement of atoms is also 8-fold co-ordinated, with spacegroup $Im3m$ and 2 atoms in the conventional unit cell, but with one atom in the primitive rhombohedral description, as already mentioned in chapter 4. This arrangement of atoms (see figure 6.4) is one of the most commonly adopted structures under high pressure, and by many metallic elements and compounds at ambient conditions of pressure and temperature. The percentage of space in the unit cell which is filled by atoms is 64%. This percentage rises to about 74% when two different atom species with a radius ratio of 0.732 adopt the binary form of this structure. This high density of atoms in the unit cell leads to

close contact distances, enhancing the hybridisation of valence electron energy levels.
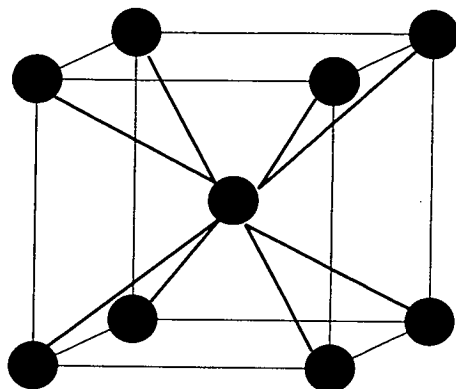

Figure 6.4. The conventional body-centred cubic cell is shown here. When the centre atom is of a different atomic species, the cell becomes simple cubic, adopting the CsCl structure.

6.3 Experimental details

The experimental arrangement is the same as that used previously in chapter 4. Angle-dispersive x-ray powder diffraction data was collected using the methods described in sections 2.1 and 2.2 at the Daresbury Synchrotron Radiation source. A Si(111) monochromator was used to select a wavelength of between 0.4Å and 0.5Å which was calibrated using a gold foil. Pinholes of 50 or 75 μm were used to collimate the monochromatic beam, and the two-dimensional diffraction patterns recorded on the image plates were scanned by a Molecular Dynamics 400A PhosphorImager. The computer program PLATYPUS was used to analyse the resulting Debye-Scherrer rings, as mentioned in section 2.1.2.

The samples, which were prepared either from crushing large granules or directly from a 4μm powder, were loaded in tungsten gaskets. A 4:1 mixture of methanol and ethanol was again used as the pressure transmitting fluid, with a ruby chip contained

within the gasket to measure pressure inside the diamond anvil cell. The pressure of the sample was again measured both before and after each set of image plate exposures, to show any signs of metal fatigue in the gasket.

6.4 Analysis and results

6.4.1 Sb-II: The simple-cubic structure

The first-order structural phase transition of rhombohedral Sb-I to that of a simple-cubic atomic arrangement (Sb-II) [94, 95, 96], has since been doubted by numerous research groups, such as those in refs. [97, 16, 99]. The unrepeatable results in individual experiments were accounted for by sample preparation and non-hydrostatic pressure conditions within the sample-space.

In order to clarify these reports, a sample of Sb was placed under conditions of both hydrostatic and non-hydrostatic pressure (achieved by including and excluding the pressure transmitting fluid from the gasket, respectively). Pressure was increased, in small steps from ambient pressure, until the relative position and intensities of the Bragg peaks in the diffraction pattern altered, indicating a change of phase. Rietveld refinements were performed on the collected diffraction patterns, from which structural properties were extracted and tabulated at each pressure.

The results given in Table 6.1 are for the sample in hydrostatic conditions, and the results for the non-hydrostatic case also showed no evidence for a structural phase transition to the simple-cubic structure. The latter diffraction patterns were not used for Rietveld refinements, since inhomogeneous pressure coefficients would result in unreliable structural parameters (unreliable in the sense that they would give slightly different structural parameters from the hydrostatic case, but are still accurate enough to show that the simple-cubic case is not adopted).

Figure 6.5 shows a typical Rietveld refinement of Sb-I at ambient pressure, and in figure 6.6 the (211) and (10$\bar{1}$) reflections at about 12° are shown to approach one

Pressure(kbar)	$a(\text{Å})$	$c(\text{Å})$	$\frac{c}{a}$	v
0	4.290	11.227	2.617	0.235
20	4.244	10.895	2.567	0.237
40	4.212	10.691	2.538	0.238
55	4.191	10.568	2.521	0.239
62	4.181	10.483	2.507	0.240
69	4.175	10.433	2.499	0.241
simple-cubic			2.450	0.250

Table 6.1. Under hydrostatic pressure the hexagonal unit cell lengths a and c, the $\frac{c}{a}$ ratio and the atomic positional parameter $(00v)$ of Sb-I approach the simple-cubic parameters. However, the first-order phase transition to phase III occurs at about 70kbar, preventing any change to the simple-cubic structure.

another under pressure. With the resolution afforded by the 2-dimensional data collection technique employed, these two peaks are easily resolved until the transition pressure required for the next phase is reached. However, with an x-ray diffraction data collection system that has a lower signal-to-noise ratio than an image-plate, the resolution will not be as great. This may lead to an incorrect assignment of the cell to be simple-cubic.

At a pressure of 69kbar, an angular resolution of about 0.16° is required to resolve (211) and (10$\bar{1}$). The theoretical maximum angular resolution obtainable from the image-plate data collection method used here (described in more detail in section 2.1), is about 0.04°. Although the imaging resolution of camera film is much greater than this, chemical fogging reduces the signal-to-noise ratio greatly, resulting in typical angular resolutions of the order 0.1°. This value is also dependent upon the design of the experimental arrangement, which supplies another possible reason for the mixed reports

about the existence for the simple-cubic Sb-II phase.
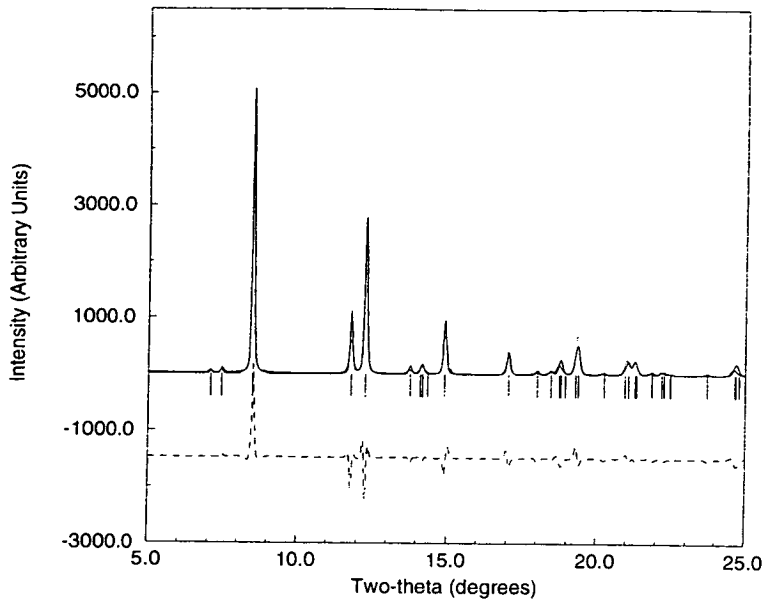
Figure 6.5. The experimental diffraction pattern (dots) is used to perform a Rietveld refinement, producing a calculated pattern (solid line, overlaying the experimental pattern) and a plot of the difference between the experimental and calculated diffraction patterns (dashed line below patterns). The reflections of the hexagonal structure are also shown as tick marks.

Figure 6.6. The position of the (211) and the (10$\bar{1}$) peaks are shown in more detail here as pressure is increased from 10.0(3)kbar to 62(2)kbar.

6.4.2 Sb-III and Bi-III: A monoclinic distortion

The structures of Sb-III and Bi-III have been the subject of much speculation for a number of years. The phase transition into Sb-III was noticed as early as 1963 [108] and the data collected was tentatively indexed as 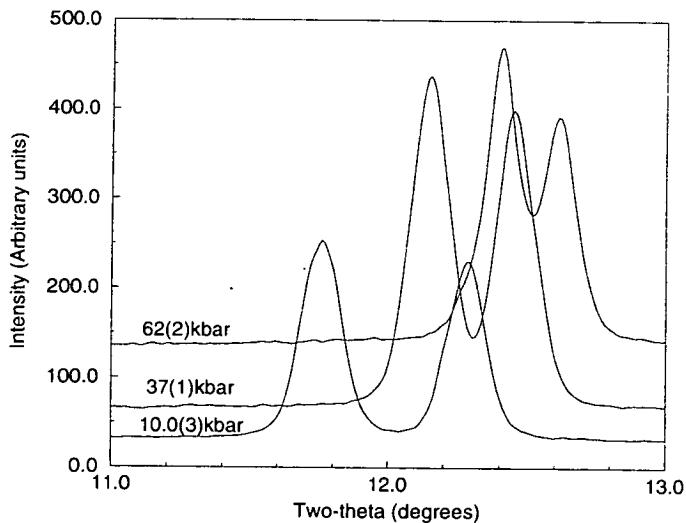being produced by a hexagonal structure. In Bi, the transition to phase III was not observed until 1969 [109], but from this time onward, research groups worked on both materials, since the structures adopted by both Sb and Bi were recognised as being the same. The suggested structures of both follow the same progression, with Kabalkina *et al.* predicting a monoclinic structure ($P2_1/m$, Z=4) [94], which was later re-indexed as being tetragonal [101]. One research group has even suggested an orthorhombic structure for Bi-III [110].

By far the most convincing work has been performed recently on both Sb and Bi [99, 104]. X-ray diffraction data was collected on image-plates, mounted at a distance of 156mm from the powder samples. At this sample-to-plate distance, there is an angular resolution of $\approx 0.3°$, assuming a digitised pixel size of 88μm. The resulting data was indexed as being produced by a tetragonal structure, from which restricted Rietveld refinements were performed for both Sb and Bi using ten atoms in the unit cell. The spacegroup used was $P4/n$, producing a structure which is a distortion of a body-centred cubic lattice, which is adopted by both under increased pressure. This structure is shown in figure 6.3 for Bi at 38kbar, using lattice parameters of a=8.640nm and c=4.235nm from ref. [104].

Although the tetragonal structure proposed for both Sb-III and Bi-III is very convincing, weak peak splittings can be observed (especially in diffraction patterns of Bi-III [104]), which are not accounted for by the tetragonal symmetry of the proposed unit cell. By increasing the distance between the sample and the image plate, finer resolution can be obtained at the expense of the angular spread over which the diffraction data can be collected. The present study on Bi-III and Sb-III was conducted

at a sample-to-plate distance of 326.8(2)mm, effectively doubling the angular resolving power. Using this increased distance, and an image-plate pixel size of 88μm, the minimum angular distance (2θ) resolvable is $\approx$0.015°. The experimental arrangement used offers a minimum angular resolution of the order 0.01°, allowing the maximum theoretical resolution to be achieved.

From the diffraction patterns collected, additional peak splittings can be observed, indicating either an orthorhombic, monoclinic or triclinic distortion of the tetragonal structure. The results in Table 6.2 show a comparison between the d-spacing observed in the present study for Sb-III at a pressure of 122(12)kbar, and those of ref. [99] collected at a pressure of 120kbar.

The split reflections in Sb-III diffraction patterns were initially indexed by assuming the ten atom tetragonal structure. Orthorhombic and monoclinic distortions were introduced to try to accommodate the additional splittings, by computing the positions of any extra reflections resulting from the drop in symmetry, and then matching the positions of these reflections to observed diffraction peaks. From the (hkl) assignments and the experimentally observed positions, the lattice parameters were refined using a least-squares algorithm. The code used to perform this refinement is called REFCEL, part of the powder diffraction program suite mounted on workstations at the Daresbury Laboratory. The average difference between observed and calculated peak positions was used as a guide for comparison between trial structures. The best structure solution obtained from this analysis was monoclinic, with a small monoclinic angle, γ.

The observed diffraction pattern of Sb-III, collected at 122(12)kbar, is shown in figure 6.7. The split (400) and (040) reflections at about 13° are enlarged for clarity. Although the splittings are small, they are consistently seen in all diffraction patterns for both Sb-III and Bi-III, which rules out any data processing errors. These additional reflections are not remnants of the previous phase of either material, which is especially evident for the Bi samples, where the previous phase only exists for approximately

d-spacing (10^{-4}nm)						
(H K L)$_{Tetr}$			Tetragonal cell (120kbar)	Present study (122kbar)	(H K L)$_{Mono}$		
2	2	0	2824(14)	2841(6)	2	2	0
2	0	1	2758(14)	2791(6)	0	2	1
2	1	1	2622(13)	2640(5)	1	2	1
3	1	0	2519(13)	2542(5)	3	-1	0
				2291(4)	3	-2	1
4	0	0	1981(10)	2009(3)	4	0	0
				1991(3)	0	4	0
0	0	2	1927(10)	1948(3)	0	0	2
4	2	0	1778(9)	1801(3)	4	2	0
4	2	1	1614(8)	1631(3)	2	4	1
3	1	2	1531(8)	1548(2)	3	-1	2
3	3	2	1347(7)	1362(2)	3	3	2

Table 6.2. The d-spacings for the two sets of data are close when experimental errors are accounted for. The tetragonal cell gives lattice parameters of a=7.965nm and c=3.857nm, compared to the monoclinic cell from the present study, which has a=8.050(4)nm, b=7.978(8)nm, c=3.904(3) and γ=89.56(9)
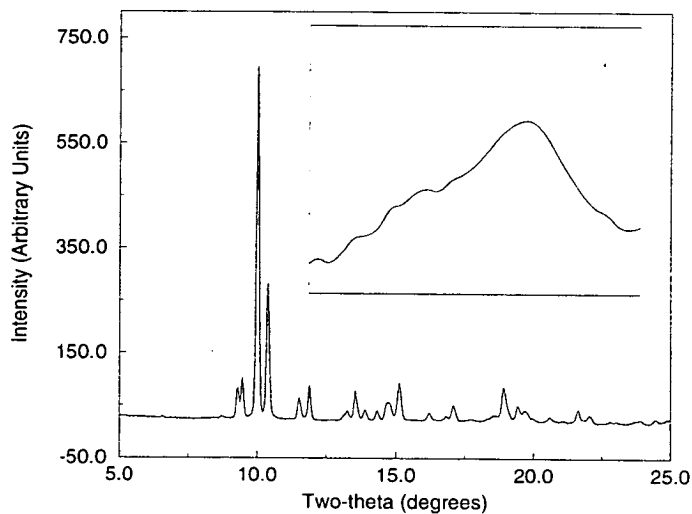
1kbar.

Figure 6.7. The diffraction pattern of Sb at 122(12)kbar is shown here, with the (400) and (040) reflections magnified to show the splitting more clearly.

The split reflections seen in Sb are also observed in Bi. Using the same technique described above for Sb, the lattice parameters for several diffraction patterns of Bi-III

and Sb-III collected at different pressures were computed. These results are shown in Tables 6.3 and 6.4 for Bi and Sb, respectively. As can be seen, the monoclinic angle in each material does not alter appreciably under pressure, but the a and b parameters tend towards those of a tetragonal structure.

H	K	L	$2\theta_{43kbar}$	$2\theta_{48.5kbar}$	$2\theta_{50.5kbar}$	$2\theta_{64.5kbar}$	$2\theta_{70.5kbar}$
2	2	0		8.68	8.70	8.77	8.81
2	-2	0	8.74	8.75			
2	0	1	8.80				
0	2	1		8.84	8.84	8.89	8.96
2	1	1	9.30	9.31	9.33	9.39	9.43
2	-1	1	9.35	9.36			
1	-2	1				9.44	9.49
3	1	0			9.70	9.80	9.83
3	-1	0	9.74	9.77			
1	-3	0					9.91
2	2	1	10.72	10.74	10.78	10.82	10.86
2	-2	1		10.79			
4	0	0	12.33	12.35	12.33	12.40	12.44
0	4	0	12.42	12.41	12.44	12.46	12.51
0	0	2	12.59			12.71	12.79
3	3	0	13.07	13.05	13.05	13.15	13.23
1	1	2				13.44	13.53
1	-1	2	13.36	13.37	13.38		
4	2	0	13.72	13.77	13.78		
2	4	0	13.80			13.91	13.95
2	0	2	13.99	14.04		14.13	14.23
4	1	1	14.15	14.18	14.19	14.27	14.33
$a(\text{Å})$			8.598(7)	8.578(5)	8.562(7)	8.530(5)	8.500(6)
$b(\text{Å})$			8.523(9)	8.534(6)	8.520(8)	8.485(5)	8.447(5)
$c(\text{Å})$			4.202(3)	4.194(5)	4.187(4)	4.165(2)	4.136(2)
$\gamma(°)$			89.50(9)	89.53(6)	89.3(1)	89.71(7)	89.69(7)
$V(\text{Å}^3)$			307.9	307.0	305.5	301.4	297.0

Table 6.3. As pressure is applied to Bi-III, the monoclinic angle γ does not seem to alter appreciably, indicating that the monoclinic structure is stable. All values of 2θ are subject to an error of $\pm 0.02°$.

The pressure dependence of Sb-I and Sb-III is shown graphically in figure 6.8, with the solid line between the points indicating a fit to the Murnaghan equation of state [88],

with B'_o fixed at a value of 5 (where B_o is the equilibrium bulk modulus). From this fit, the bulk moduli of Sb-I and Sb-III are calculated to be 402(15)kbar and 458(47)kbar, respectively. This increase in bulk modulus (or decrease in compressibility) is brought about by the greater packing fraction seen in the monoclinic structure of Sb-III. The increased complexity and density of this phase decreases the contact distance between neighbouring atoms, as would be expected in a metallic structure. There is a hysteresis of about 20kbar between the two phases, but beyond 80kbar, no degree of phase I is observed in the Sb-III diffraction patterns.
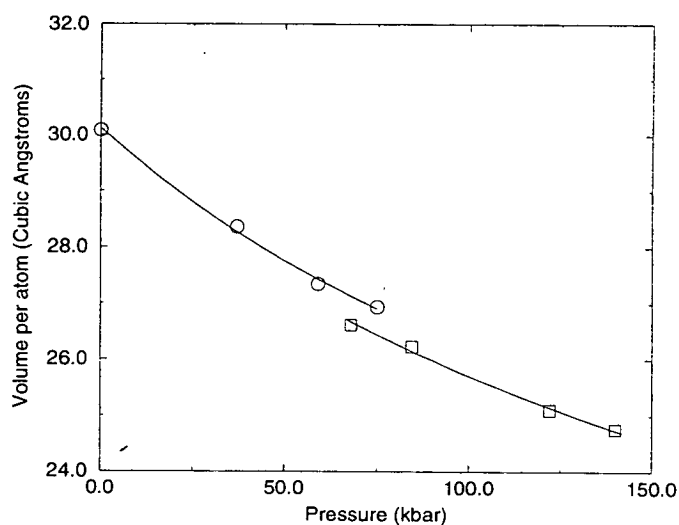

Figure 6.8. The volume per atom plotted against pressure for Sb-I (circles) and Sb-III (squares) is shown here. The data for Sb-I was collected on the upstroke of pressure, and those for Sb-III on the down-stroke. The solid lines correspond to a fit to the Murnaghan equation of state.

Metallic structures (and this tetragonal structure is no exception) tend to adopt atomic arrangements which will maximise the packing ratio. This leads to easier mobility of electrons in the conduction bands. While structures such as body-centred cubic and face-centred cubic (as adopted by NaCl) may increase the packing ratio, it is achieved at the expense of bond directionality, thus decreasing uni-directional strength. Body-centred cubic structures can be produced by layering atoms in the (111), (200), (020), (002), (110), etc crystallographic directions. Face-centred cubic and hexagonal

close packed structures can also be thought of as being composed of layers of atoms in the (200), (220), etc directions. These layered structures lead to shearing stresses which promote cleavage, resulting in an increased probability of preferred orientation.

In structural refinements for Sb-III by other authors [99], preferred orientation in the sample was found to be a problem. Even after the calculated diffraction patterns had the effects of preferred orientation included in their computation, the correspondence between calculated and experimentally observed intensities of several diffraction peaks was still poor. This preferred orientation was also seen in the present study in diffraction patterns of Sb-III and Bi-III. A typical image from the image-plate data for Bi at 70(2)kbar is shown in figure 6.9. The colour contrast of the image has been altered to emphasise the unequal variation of intensity around each Debye-Scherrer ring. At this pressure, both Sb and Bi are metallic, which offers a possible explanation as to why preferred orientation effects are so obvious in these samples under pressure.

Preferred orientation effects and pressure within the diamond anvil cell deviating slightly from the ideal hydrostatic condition combine, making a full Rietveld refinement difficult. When attempting a full refinement, the computed intensities for several reflections either fell too short of the observed intensity, or were too strong. This led to the least-squares method altering the position and peak shape of the reflections to

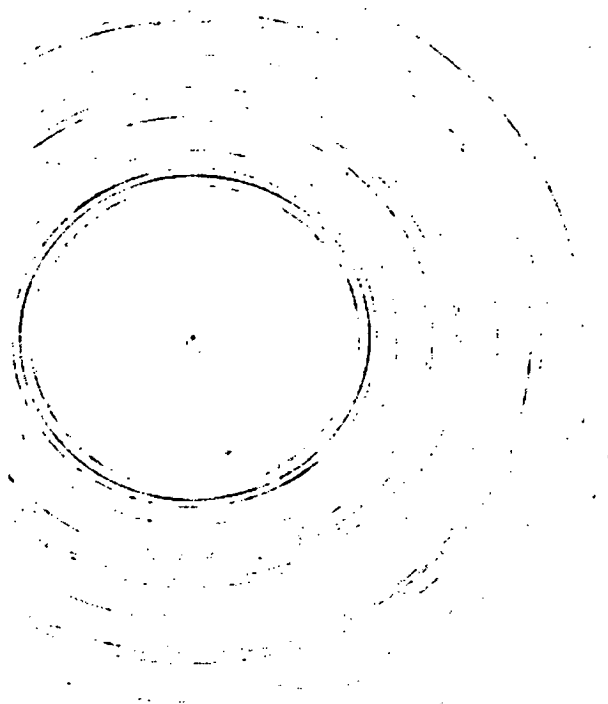compensate for the intensity shifts. This inevitably led to inaccurate results.

Figure 6.9. The image-plate data for Bi at 70(2)kbar is shown here. The colours have been inverted, and the contrast altered to show the effects of preferred orientation in the sample more clearly.

Although corrections could be applied to the computed diffraction patterns generated by the Rietveld refinement methods, the simple formula involved proved ineffective. Therefore, another scheme was employed to compute atomic positions within the unit cell, with error limits placed around these locations. A Monte-Carlo technique, originally written to seek structural models for organic solids, was optimised for inorganic materials and used to compute the best structural configuration, using the whole diffraction pattern and the weighted R-factor from a heavily constrained Rietveld refinement (only the scale factor was refined).

The spacegroup of the monoclinic phase was first obtained by observing the reflection conditions $(hk0)$: $h + k = 2n$, $(h00)$: $h = 2n$ and $(0k0)$: $k = 2n$. This last reflection condition is not allowed by the tetragonal spacegroup $P4/n$, necessitating a

H	K	L	$2\theta_{68kbar}$	$2\theta_{84.5kbar}$	$2\theta_{122kbar}$	$2\theta_{140kbar}$
2	0	0	6.42	6.47	6.56	6.59
2	2	0	9.10	9.17	9.30	9.34
0	2	1	9.31	9.34	9.47	9.51
2	1	1		9.84		
1	2	1	9.79		10.01	10.06
3	1	0	10.16	10.24		
3	-1	0			10.40	10.44
3	-2	1			11.54	11.59
4	0	0	12.87		13.17	13.22
0	4	0	13.03		13.29	13.35
0	0	2	13.30	13.39	13.58	13.60
3	2	1				13.68
1	0	2			13.94	13.99
3	3	0	13.63			
1	-1	2	14.05			14.42
4	2	0	14.37		14.70	14.74
4	-2	0		14.53		14.84
4	0	1			14.82	
4	1	1	14.81	14.94	15.15	15.21
2	4	1			16.24	
4	2	1				16.29
3	-1	2		16.88	17.12	17.19
3	1	2	16.73			
0	4	2		18.73		
5	2	1	18.55		18.96	19.03
3	3	2	19.05	19.22	19.48	19.56
6	0	0			19.76	19.85
1	5	2		21.40		
5	-1	2	21.22			
$a(\text{Å})$			8.219(6)	8.173(4)	8.050(4)	8.019(4)
$b(\text{Å})$			8.123(9)	8.115(6)	7.978(8)	7.935(9)
$c(\text{Å})$			3.986(3)	3.954(2)	3.904(3)	3.891(3)
$\gamma(°)$			89.2(1)	89.75(6)	89.56(9)	89.57(7)
$V(\text{Å}^3)$			266.1	262.3	250.7	247.6

Table 6.4. The progression of diffraction maxima can be seen in Sb-III under pressure. The computed lattice parameters are also shown below each list of reflections.

drop in symmetry to the monoclinic spacegroup $P2/n$ ($P2/c$, with the c-axis unique). $P2/n$ was also chosen because it is a sub-group of $P4/n$.

The MC calculation was started using a diffraction pattern of Sb collected at 140(14)kbar, space-group $P2/n$ and 3 atoms, two placed on the general, $4(g)$ (x, y, z) site, and one on the special, $2(e)$ $(\frac{1}{4}, \frac{1}{4}, z)$ site. A minimum contact distance of 2Å was imposed on the trial structures to limit the number of randomly generated atomic arrangements. The lattice parameters, as computed using least-squares refinement of the accurately determined peak positions, were used. These are given in Table 6.4. After 10000 cycles, one clear solution emerged from all other trial structures, as the top 10 solutions with the best R-factors were all the same structure. These solutions are presented in Table 6.5.

	R= 37.534			R= 38.959		
SB	0.2500	0.7350	0.2500	0.2500	0.7037	0.2500
SB	0.5830	0.1885	0.1898	0.5886	0.7808	0.9428
SB	0.6591	0.7179	0.4957	0.4360	0.7523	0.7114
	R= 37.781			R= 39.032		
SB	0.2500	0.7534	0.2500	0.2500	0.7625	0.2500
SB	0.6165	0.2329	0.2063	0.5591	0.7889	0.0099
SB	0.6410	0.7882	0.5041	0.4409	0.7817	0.7186
	R= 38.398			R= 39.167		
SB	0.2500	0.2593	0.2500	0.2500	0.3176	0.2500
SB	0.6865	0.2474	0.4635	0.2002	0.8303	0.5067
SB	0.5697	0.7778	0.2024	0.9325	0.7336	0.2044
	R= 38.639			R= 39.377		
SB	0.2500	0.7746	0.2500	0.2500	0.8087	0.2500
SB	0.5738	0.7457	0.9645	0.5733	0.7192	0.9528
SB	0.4207	0.7790	0.7290	0.4622	0.7377	0.7315
	R= 38.688			R= 39.378		
SB	0.2500	0.7067	0.2500	0.2500	0.7688	0.2500
SB	0.5947	0.2784	0.2215	0.0503	0.8187	0.6956
SB	0.6495	0.8183	0.4912	0.6910	0.6764	0.0132

Table 6.5. Fractional atomic co-ordinates of the three Sb atoms placed within the unit-cell are shown for the 10 best solutions obtained after 10000 MC cycles. The lattice parameters used were a=8.019Å, b=7.935Å, c=3.891Å and γ=89.57°.

The progression of R-factor with MC cycle number is shown in figure 6.10, from which it can be seen that the solution with the lowest R-factor was reached within 3000 MC cycles, making this an efficient form of analysis. The drop in R-factor was about 13%, between the best solution and the most randomly generated structure. The best solution gave atomic co-ordinates at $(\frac{1}{4}, \frac{1}{4}, 0.76(3))$, $(0.10(5), 0.75(5), 0.26(5))$ and $(0.25(5), 0.80(5), 0.55(5))$.

When compared to the atomic co-ordinates obtained from the refinement performed on the tetragonal structure proposed for Sb-III at 120kbar [99], the results from the Monte-Carlo calculation are found to be consistent with a monoclinic distortion. The two atoms on general positions computed from the MC calculations can be related to one atom on the (x, y, z) position and the symmetrically equivalent position, $(y+\frac{1}{2}, \bar{x}, \bar{z})$, within the tetragonal $P4/n$ structure.

Although in this analysis the Monte-Carlo method was successful in computing average atomic positions from diffraction patterns suffering from preferred orientation effects, this will not always be the case. Reflection intensities alone are used to deduce atomic positions, so if they are affected in any way, this will hinder any analysis method. With severely affected diffraction patterns, the Monte-Carlo method may even cluster atoms around locations which might compute diffraction patterns close to the observed data, but which may not lead to the correct crystal structure. Therefore, careful attention must be taken by the end-user of the Monte-Carlo technique, that the inherent

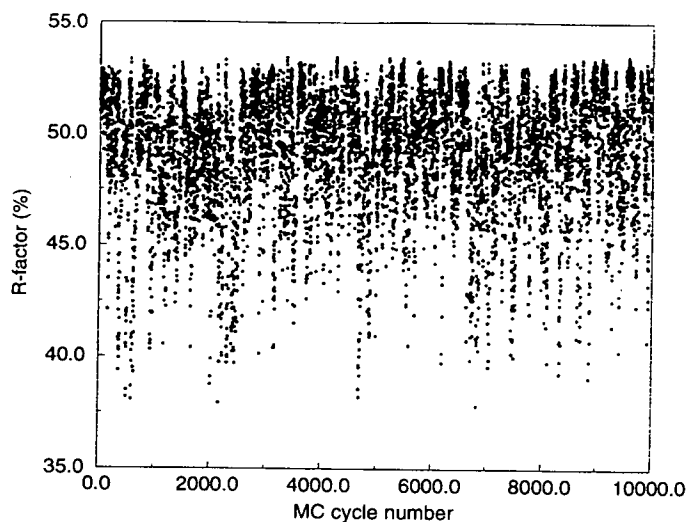random nature of the method does not lead to false conclusions.

Figure 6.10. The R-factor computed at each MC cycle is plotted here to show the calculation entering, and exiting, the best solutions.

6.4.3 Structural phase transitions in Bi

Although many results have been published on the various high pressure phases observed in Bi [103, 104, 106], one complete study of all phases has never been undertaken. In order to consolidate all previous reports under pressure, Bi was examined from ambient pressure up to 84(5)kbar, allowing all high pressure structures to be examined in detail. The monoclinic structure of Bi-II, previously observed and refined using neutron diffraction [103] was confirmed, and the monoclinic distortion from the tetragonal structure seen in Sb was also shown to exist, as described in the previous section.

The structure of all phases of Bi have been described in the previous two sections, which range from the ambient pressure rhombohedral structure to the two monoclinic structures, ending up in the body-centred cubic structure. This sequence of phase transitions are summarised by the diagram in figure 6.11.

The progression of Bi under pressure is also shown in figure 6.14, by plotting the diffraction patterns obtained at various pressures, in each observed phase. Slight mixing
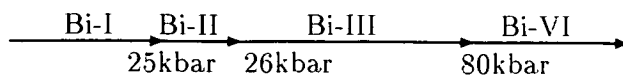
Bi-I   Bi-II   Bi-III   Bi-VI

25kbar   26kbar   80kbar

Figure 6.11. Rhombohedral $(R3/m)$ becomes monoclinic $(C2/m)$ at 25kbar. This exists for about 1kbar at ambient temperatures, until the monoclinic $(P2/n)$ distortion of the tetragonal structure becomes stable. Then, at about 80kbar, Bi becomes body-centred cubic $(Im3m)$.

of phases I and II was observed at a pressure of 26(1)kbar. The amount of mixing was small, so in order to reduce refinement error, only the lattice parameters of phase I were refined, and the variable atomic parameter was fixed at the refined value obtained at the closest pressure to the phase II transition, but still within the phase I structure. The observed and calculated patterns are shown in figure 6.12 for this refinement, and the computed structural parameters are given in Table 6.6.
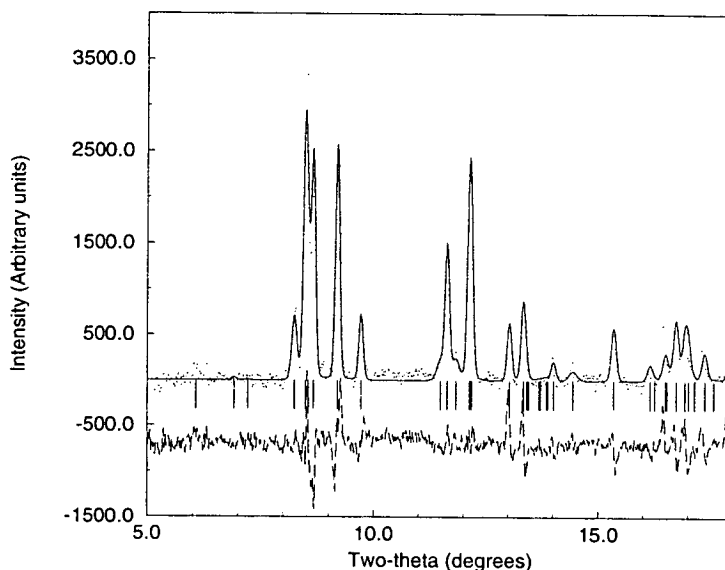

Figure 6.12. The Rietveld refinement of Bi-II is shown here. The solid line is the computed diffraction pattern from the experimental pattern (dots). The profile (dashed line) below the two main diffraction patterns is the difference between the two curves, with reflection shown as tick marks below all three curves.

As explained in the previous chapter, no refinement of Bi-III was performed, since preferred orientation effects introduced too many errors, but refinements of the final phase, Bi-VI were completed. This was trivial, as the structure is just body-centred

cubic, but from the lattice parameters obtained an isothermal phase diagram for Bi at room temperature ($\approx 25°$C) was calculated. This is shown in figure 6.13.

	Bi-I	Bi-II
Amounts(%)	4.8	95.2
$a(\text{Å})$	4.50(1)	6.70(1)
$b(\text{Å})$	4.50(1)	6.15(1)
$c(\text{Å})$	11.49(1)	3.32(1)
$\alpha(\text{Å})$	90.0	90.0
$\beta(\text{Å})$	90.0	110.39(1)
$\gamma(\text{Å})$	120.0	90.0
v	0.243	
x		0.247
y		0.348

Table 6.6. The structural parameters obtained for Bi-I in the hexagonal setting and Bi-II from the multiphase refinement at 26(1)kbar (figure 6.12) are tabulated here. The atomic positional parameters are for the atoms on the $6(c)$, $(0,0,v)$ sites in Bi-I, and for the atoms on the $4(i)$, $(x,0,z)$ sites in monoclinic $C2/m$ Bi-II.

Using the values obtained from Rietveld refinements of Bi-I patterns and least-squares analysis of Bi-III reflections, the Murnaghan [88] equation of state was used to compute bulk moduli. B'_o was fixed at a value of 5, resulting in a bulk modulus of 307(24)kbar for Bi-I and 471(95)kbar for Bi-III. It was not possible to perform these calculations for Bi-II or Bi-VI due to the small number of available patterns for

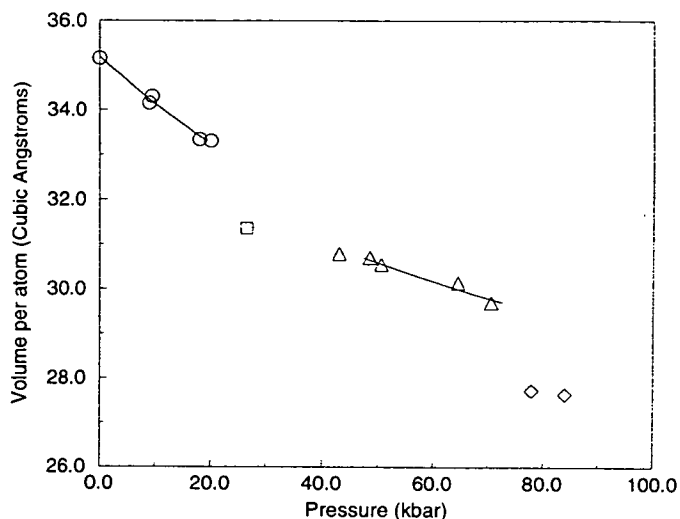refinement (only one for Bi-II and two for Bi-VI).

Figure 6.13. The isothermal phase diagram of Bi at 25°C is calculated from re-
finements of Bi-I (circles), Bi-II(squares) and Bi-VI(diamonds), and from the lattice
parameters obtained from the least-squares analysis of Bi-III(triangles). The solid
lines through the points indicate a fit to the Murnaghan equation of state.
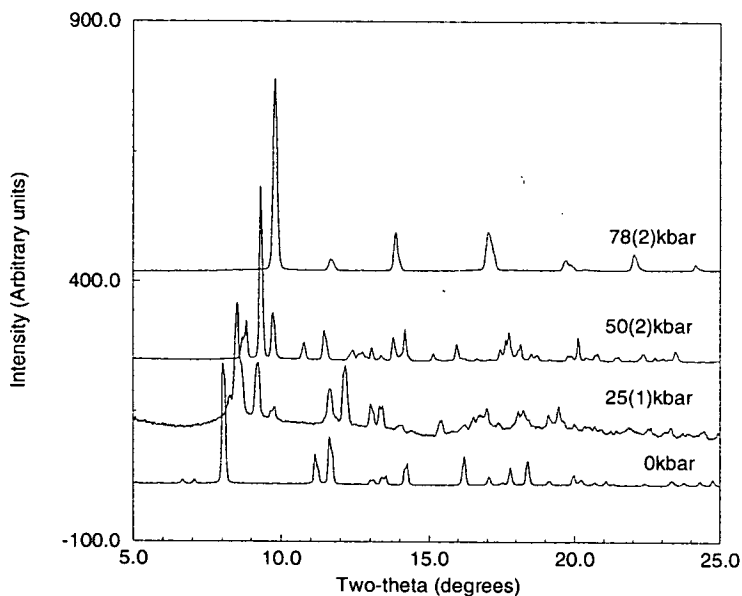

Figure 6.14. The diffraction patterns obtained for Bi are shown here at ambient
pressure(Bi-I), 25(1)kbar (Bi-II), 50(2)kbar (Bi-III) and 78(2)kbar (Bi-VI).

6.5 Conclusions

One of the main reasons for studying high pressure phase transformations occurring in the group V elements was to shed light on the transformations observed in the group IV-VI PbX, (X=Se,S,Te) compounds under pressure. The lead chalcogenides begin in the NaCl-type structure, which under pressure transforms to the CsCl-type structure via an intermediate phase. This sequence of transitions is basically similar to those occurring in the group V elements, and especially in Sb, which adopts a distorted face-centred cubic structure at ambient pressure, which then transforms to the mono-valent equivalent of the CsCl-type structure (body-centred cubic) via an intermediate phase.

The structure of PbSe has been found to be an orthorhombic structure, similar to the structure adopted by GeS, but PbS and PbTe do not exist in this structure [111]. When indexing diffraction patterns of Sb-III, Bi-III and the intermediate phase observed in PbS and PbTe, only monoclinic or triclinic cells are produced using DICVOL or TREOR90. Since a monoclinic structure was found for both Sb-III and Bi-III, this suggests that the intermediate phase seen in PbS and PbTe may also be a complex monoclinic phase, perhaps related to the monoclinic structure observed in Sb and Bi. Indeed, under conditions of elevated temperature and pressure, Sb has been indexed monoclinic with lattice parameters not unlike those of the intermediate phase of PbSe [112].

Another observation was made when analysing the experimentally collected data on Bi-III, as to the nature of the phase transition from body-centred Bi-VI to monoclinic Bi-III. As pressure was increased from ambient, Bi-III was formed at about 26kbar, producing clear 2-dimensional Debye-Scherrer rings on the image-plates. This indicated that the powder averaging of the sample was still good. After the transition to Bi-VI was completed at about 70kbar, the pressure was then reduced in small steps to recover the previous phases. However, when Bi-III patterns were formed once again, the rings on the image-plate patterns were composed almost entirely of spots, but integration

still gave diffraction patterns consistent with the Bi-III structure. These two images of Bi-III on the upstroke and downstroke of pressure are shown in figures 6.15(a) and 6.15(b), respectively. This indicates that upon decompression large crystallites of Bi-III are formed, producing the "spotty" patterns which were observed. To form such crystallites through a phase transformation suggests that some form of nucleation and growth is occurring, allowing small crystals of Bi-III to form. These crystals will reach a certain critical size before becoming too stressed, perhaps as a result of phase mixing or non-hydrostatic pressure conditions in the diamond-anvil cell. It would be interesting to study this recovered phase using methods probing short-range order, to view the stacking arrangement of atoms within the structure.
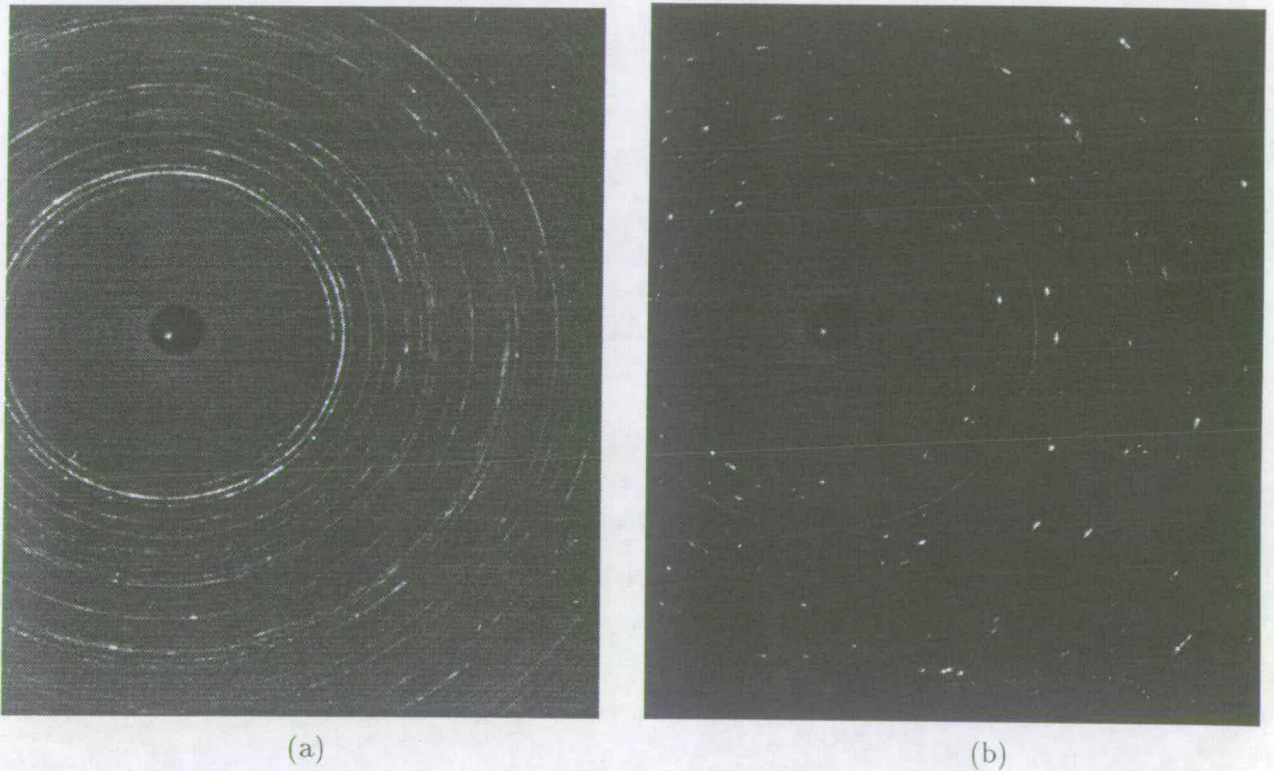

(a)

(b)

Figure 6.15. Image-plate data for Bi-III on the upstroke of pressure (a) at 64.5kbar, and on the downstroke (b) at 65kbar are shown here.

In order to complete the study of the high pressure phase transition observed in Sb, total energy calculations were started on Sb-III using the pseudo-potential method

[113]. These were performed to show the electronic nature of each pressure phase, as well as confirming the stability of each structure under pressure. The calculations were started with the ambient pressure rhombohedral phase Sb-I. As outlined in chapter 3, the number of k-points within the Brillouin Zone must be optimised to obtain accurate energies at all volumes. This process for Sb-I led to the conclusion that over 1000 k-points were needed to supply accurate enough energies. This is a large calculation when compared to the full-potential calculations performed on CuCl in chapter 5, which required a maximum of 64 k-points.

This large number of k-points was required because Sb-I is a semi-metal, hence a great number of k-points are needed to sample the valence band accurately. To complete calculations of this size for all the relevant phases of Sb would have required several months, since the number of k-points needed for the metallic higher pressure structures would have been even greater. As this sort of time was not available, these results were not obtained, but they would have given an insight into the degree of metalisation undergone in Sb under pressure, as well as showing the stability of the tetragonal and monoclinic structures for Sb-III. They may also have proven the instability of Sb-II, reinforcing previous experiments which could not verify the existence of the simple-cubic phase. Even though the monoclinic distortion of the ten atom tetragonal structure is small, there may still be a noticeable difference between the equilibrium total energies of each arrangement of atoms, if there is a kinetic barrier to one of the structures. For this reason alone, a study of the electronic properties of all possible phases of Sb would be very interesting.

Although the MC method is a unique computational method to deal with high pressure powder diffraction patterns suffering from preferred orientation problems, the results obtained from it in this study can only be taken as estimates of the actual atomic positions. However, the MC calculation can be tailored to reduce the statistical error, by concentrating the searching procedure around the best solutions. This could be accomplished by reducing the step size between atomic translation in each random

cycle, or by decreasing the scale factor S, equivalent to quenching the system by reducing "temperature" in an energy based MC calculation. However, introducing any additional constraints to a random process inevitably increases the number of cycles required to find the global minimum. Computing power and available time are, once again, limiting factors.

Chapter 7

High pressure forms of group IV-VI compounds

The high pressure phases of PbS, PbSe and PbTe are investigated here, using angle-dispersive x-ray powder diffraction with image plate area detectors. These materials change phase from the ambient pressure face-centred cubic structure to the high pressure body-centred cubic structure, via an intermediate phase, the crystal structure of which has not previously been solved. The structure of the intermediate phase for PbSe was shown to be orthorhombic, with four formula units, but the structure of both PbS-II and PbTe-II was not solved exactly. However, a monoclinic or possibly a triclinic structure must be adopted, due to the complexity of the collected diffraction patterns. Evidence supporting this conclusion is given, as well as possible future work required to solve each structure.

My contribution to this work was the collection and analysis of all the x-ray diffraction patterns for each material, the results of which are given in this chapter.

7.1 Background

The primary goal of high pressure study is to deduce possible transition routes between different structure types and to understand the factors governing structural adoption. By far the most common transition is from the face-centred cubic NaCl-type structure to the body-centred cubic CsCl-type structure. This transition is observed in many semiconductors and metals under pressure, with metalisation normally being the result due to the increased co-ordination number afforded by the closely-packed arrangement in the CsCl-type structure.

Most of the alkali-halides go straight from the ambient pressure NaCl-type structure to the high pressure CsCl-type structure, without any intermediate phase to show different stages in the overall transition. This hinders the chances of observing the actual route taken by the atomic arrangements of each material through the transition. However, NaI and NaBr exist in an orthorhombic structure, similar to that adopted by GeS at ambient pressure, between the low and high pressure cubic phases. This situation is thought to occur because of the increased ionic sizes in these compounds, making the NaCl-type structure less stable at ambient pressure, as compared to the CsCl-type structure.

A similar pressure transition route has also been observed in the heavy IV-VI compounds PbTe, PbSe and PbS. Between the ambient pressure NaCl-type structure and the high pressure CsCl-type structure, intermediate phases are observed. These intermediate structures were initially indexed to be the same for all three of the lead-chalcogenides, having a structure similar to that of GeS [114, 115], but this structure was later only proposed for PbTe and PbS [116]. A similar orthorhombic structure with slightly higher symmetry (adopted by TlI) was proposed for the intermediate phase of PbSe [117]. However, the most recent of these studies were performed using energy-dispersive techniques [116, 117], making any attempts to refine the structures difficult, due to unreliable intensities.

Experiments involving laser-assisted deposition of thin films of PbTe on a KCl substrate [1, 118, 119, 120] have shown that the high pressure phases can be obtained at ambient pressure. This is due to the strain imposed on the NaCl-type structure of PbTe by the mismatch between the lattice parameter of the ambient pressure PbTe phase and the KCl substrate layer. This mismatch (about 3%) corresponds to the relative rate of change of the lattice parameters of PbTe-II in the orthorhombic structure proposed by [116] at the phase transition. Using both x-ray and optical experiments, it was shown [1] that PbTe-II forms at the substrate layer, which then becomes the CsCl-type structure (PbTe-III), followed by the NaCl-type structure (PbTe-I) at about 0.5μm from the KCl substrate. This has great implications for the semiconductor industry, as the lead chalcogenides (including PbTe) are used extensively as IR sensors. The different structures adopted by PbTe under pressure will exhibit different optical and electrical properties, thus altering the performance of an IR sensor fabricated by similar techniques as described above.

A more accurate study of the high pressure phases in PbTe, PbS and PbSe was thus warranted, especially with the parallels observed with high pressure phases seen in Sb and Bi. These elements show evidence of monoclinic distortions under pressure between a distorted face-centred cubic ambient pressure structure and a high pressure body-centred cubic structure. To investigate the similarity between phase transitions in the group V elements and the lead chalcogenides, high pressure x-ray powder diffraction experiments were performed on the PbX (X=S,Se,Te) compounds.

7.2 Experimental details

The experimental arrangement is the same as that used in chapters 4 and 6. Angle-dispersive x-ray powder diffraction data was collected using the methods described in sections 2.1 and 2.2 at the Daresbury Synchrotron Radiation source. A Si(111) monochromator was used to select a wavelength of between 0.4Å and 0.5Å which was

calibrated using a gold foil. A pinhole of $50\mu m$ was used to collimate the monochromatic beam, and the two-dimensional diffraction patterns recorded on the image plates were scanned by a Molecular Dynamics 400A PhosphorImager. The computer program PLATYPUS was used to analyse the resulting Debye-Scherrer rings, as mentioned in section 2.1.2.

The powdered samples were loaded in tungsten gaskets with a 4:1 mixture of methanol and ethanol, to create near hydrostatic pressure conditions within the diamond anvil cell (DAC). A ruby chip was included in the gasket to measure pressure inside the DAC both before and after each set of image plate exposures.

7.3 Structural details

7.3.1 NaCl-type structure

At ambient pressure, all three lead-chalcogenides adopt the NaCl-type structure. This close-packed arrangement of atoms has already been described in detail in chapter 5, but the structure may be viewed in a different manner when the conventional face and body-centred atoms are placed in the centre of a six-fold array of atoms, as shown in figure 7.1. This view is chosen to enable the similarity between the NaCl-type and CsCl-type structure to be seen, as well as between other possible high pressure structures [115]. This arrangement of atoms has a high packing ratio, especially when the two different atom species have different effective* atomic radii. The packing fraction starts at about 74% for atoms of the same type, and increases to around 80% for atoms with

---

*The term "effective" is used to indicate the fact that atomic radii are difficult to quantify exactly. Ionic radii are the most reliable source, but most compounds exhibit some degree of covalency, which tends to *blur* the edge of the well defined ionic spheres.
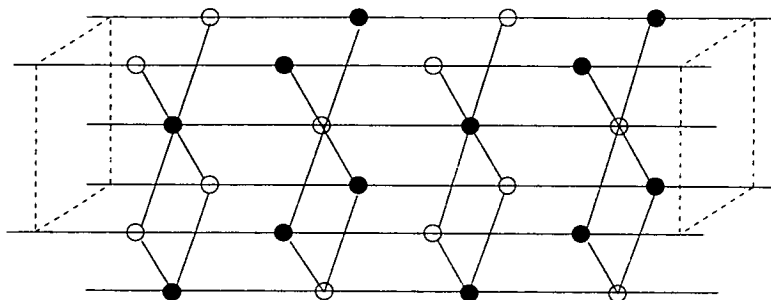
a radius ratio of about 2.4:1.

Figure 7.1. The NaCl-type structure is shown here with the (100) crystallographic direction going into the page.

7.3.2 CsCl-type structure

The structure that all three lead chalcogenides adopt at the highest pressures is the CsCl-type structure. The phase transition to this structure occurs at about 240kbar for PbS, 160kbar for PbSe and about 130kbar for PbTe. This cubic structure has eight-fold co-ordination, and is the binary analogue of the body-centred cubic structure adopted by Sb-IV and Bi-V.

Although the CsCl-type structure has a body-centred arrangement of atoms, the lattice is actually simple-cubic, since the atom located at the centre of the cell is of a different species to those occupying the corner sites. The spacegroup is $Pm\bar{3}m$, with a two atom basis, one on the $1(a)$, $(0,0,0)$ site, and the other on the $1(b)$, $(\frac{1}{2},\frac{1}{2},\frac{1}{2})$ site. This structure is shown in figure 7.2 in an unconventional setting, emphasising

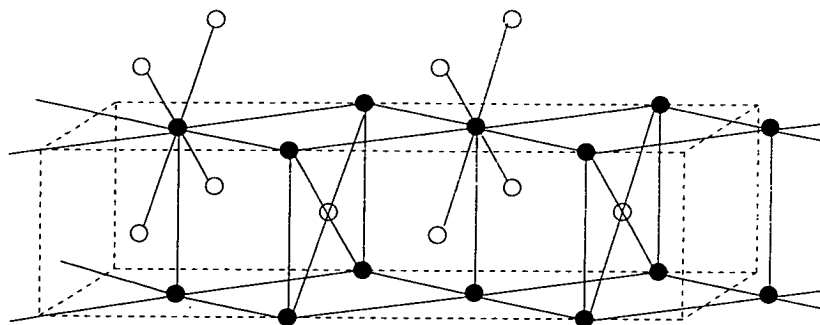the structural relationship to the NaCl-type structure.

Figure 7.2. The simple cubic CsCl-type structure is shown with the (110) crystallographic direction going into the page.

Examining figure 7.2 shows the relation between the CsCl and NaCl-type structure clearly. The view of the NaCl and CsCl-type structures in figures 7.1 and 7.2 shows the relationship between the (100) direction in NaCl and the (110) direction in CsCl. These two common planes of atoms have been suggested as being a possible transition route between the two cubic structures in CsCl, while undergoing a temperature induced phase transformation [121]. Another possible route has also been suggested [122], in which the common direction to both structures is the (111) direction. This transition involves a contraction along this direction in the NaCl-type structure, which eventually leads to the CsCl-type structure. This transition route has also been studied theoretically [123] for alkali halides under pressure.

The actual route taken by the lead chalcogenides may be either one of those already mentioned, or a combination of both, or a completely different method altogether. In the alkali halide and actinide compounds, the NaCl→CsCl transition is accompanied by a large volume collapse (approximately 10%), as well as a large amount of hysteresis. Previously, this phase transition was thought to be completed via a massive re-organisation of atoms, with the NaCl-type phase becoming almost amorphous (*i.e.*

losing all long-range order), followed by a re-crystallisation into the CsCl-type structure. However, with the discovery of an intermediate phase in the lead chalcogenides, the transition between NaCl-type and CsCl-type structures may be possible with a smaller amount of bond-breaking and re-formation.

7.3.3 GeS-type and TlI-type structures

At pressures of around 24, 45 and 60kbar, an intermediate phase between the two cubic phases is adopted by PbS, PbSe and PbTe, respectively. The intermediate structure adopted by all three of the lead chalcogenides has been proposed to be an orthorhombic structure [114, 115, 117], similar either to that adopted by GeS or TlI. These two structures are very similar, although different spacegroup symmetries alter the bonding configuration and co-ordination number.

The orthorhombic GeS structure is the more stable structure for the lighter IV-VI semiconductors GeS, GeSe, SnS and SnSe. This structure is also the binary analogue of black phosphorous, and can be thought of as being a distorted NaCl-type structure. With spacegroup *Pbnm* and eight atoms in the unit cell, 6-fold co-ordination is found in the lighter IV-VI compounds. However, as atomic size is increased, the atomic co-ordination becomes a 6-fold and 7-fold mixture, which is to be expected between the lower pressure 6-fold co-ordinated NaCl-type structure and higher pressure 8-fold co-ordinated CsCl-type phase. Columns of atoms form buckled chains, which do not exhibit bonding between layers of chains. Within each layer of chains, the inter-bond separation is relatively short compared to the overall dimensions of the lattice, but the
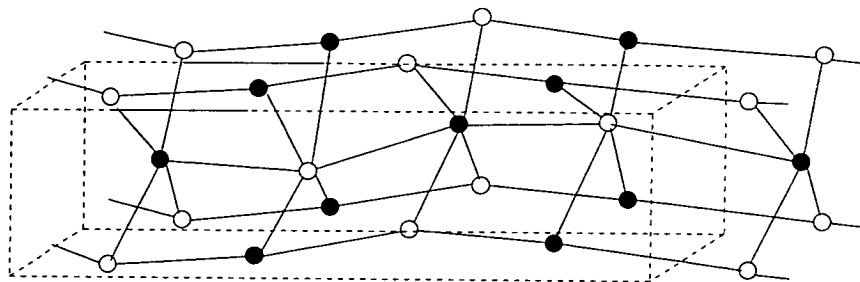
intra-layer separation is relatively large.

Figure 7.3. The GeS-type structure is orthorhombic, spacegroup *Pbnm*, containing 8 atoms in the unit cell.
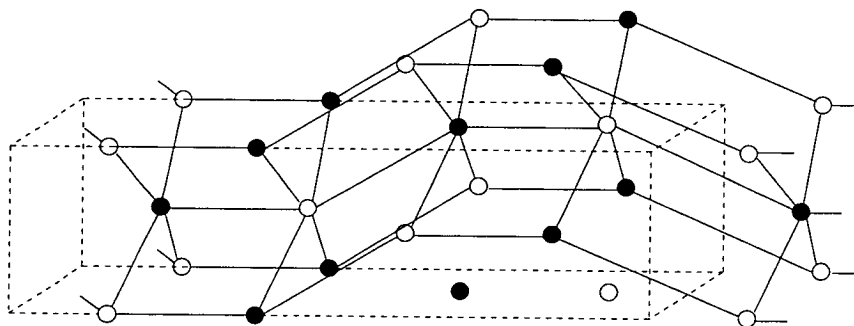

Figure 7.4. The TlI-type structure is more rigid due to the higher symmetry, but still contains eight atoms.

These buckled layers are also seen in the TlI-type structure, spacegroup *Cmcm*, and $Z=4$. However, the increased symmetry (base-centred as opposed to the primitive setting in the GeS-type structure) makes the structure more rigid, with less degrees of freedom. The amount of inter-layer buckling is also greater, and 7-fold co-ordination is observed as a result.

7.4 Analysis and results

7.4.1 The structure of PbSe-II

As pressure was increased on the powdered sample of PbSe, the first signs of the intermediate phase were observed at 46(2)kbar. However, the previous diffraction pattern showing no signs of the phase was taken at 39(2)kbar, so the actual transition occurred somewhere between these two pressures, giving an approximate pressure of about 43(3)kbar for the transition. This estimate agrees well with the previously reported observations of the transition at 42kbar [114] and 45kbar [117], giving an average transition pressure of about 43(2)kbar.

Previous reports on the structure of PbSe-II have indicated that an orthorhombic structure similar to that of TlI is adopted [117], while others indicate a GeS-type structure [114]. To test these assignments, known structural parameters for the TlI structure were used to initially assign (h, k, l) reflections to the strongest peaks in the diffraction pattern. This was then used to start a Rietveld refinement, by first optimising the lattice parameters, holding the atomic positions fixed, and then relaxing all the structural degrees of freedom. The results for PbSe-II at 51(2)kbar are shown in figure 7.5. The structural parameters obtained from this refinement are given in Table 7.1.

	$a(\text{Å})$	$b(\text{Å})$	$c(\text{Å})$	$u_{Tl,Pb}$	$u_{I,Se}$
TlI	4.582	12.92	5.251	0.392	0.1333
PbSe as TlI	4.254	11.602	4.424	0.1228	0.3633

Table 7.1. Structural parameters for TlI and from the refinement of PbSe-II in the TlI structure. The symmetry was $Cmcm$ with Pb and Se atoms on the $4(c)$, $(0, u, \frac{1}{4})$, sites.

As can be seen, the fit to the experimental pattern is good, although there are a few discrepancies. The most noticeable difference is the shoulder to the left of the main peak at a 2θ of about $9°$. The shoulder clearly indicates that another peak is

present, but under the spacegroup of TlI ($Cmcm$), a reflection is not allowed in this position. By dropping the symmetry from a face-centred lattice to a primitive setting, a reflection *is* allowed in this position, corresponding to the (101) crystallographic direction. This reflection is absent in the $Cmcm$ spacegroup, as are all the ($h0l$) reflections with $h, l \neq 2n$. These reflections are allowed in the GeS-type structure, which has spacegroup $Pbnm$. For this reason, a refinement was started with this structure type as a starting model.
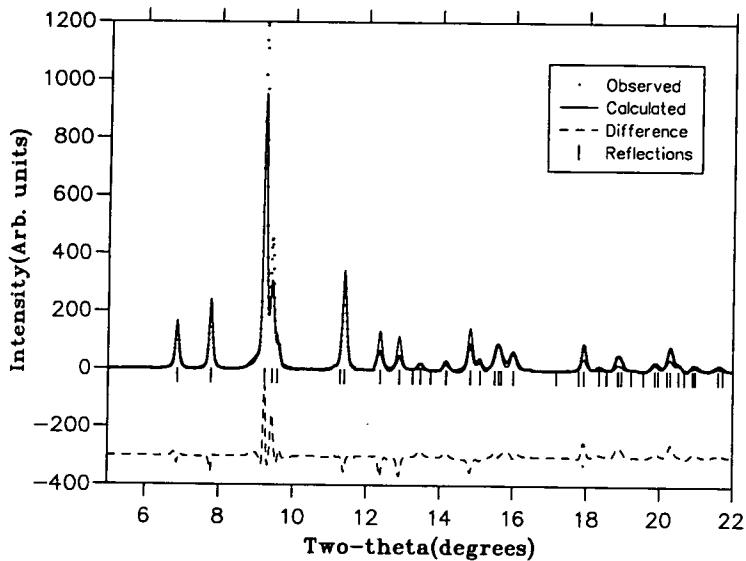

Figure 7.5. The intermediate phase of PbSe-II refined in the TlI structure is shown here at 51(2)kbar. The dotted line is the experimental diffraction pattern, with the solid line of the calculated pattern overlaying this. Under these two patterns, the difference is shown as a dashed line, and the positions of reflections are indicated by tick marks.

Using lattice parameters from GeS (see Table 7.2) a list of reflection positions and intensities was obtained. The main peaks observed in PbSe were matched to those in the GeS structure, giving initial lattice parameters for PbSe in the intermediate phase. These were then used, together with atomic positions for GeS to produce a Rietveld

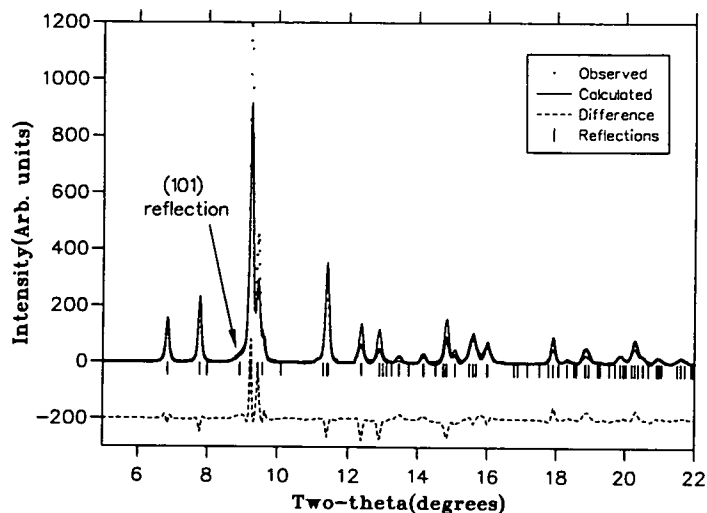refinement of PbSe in the GeS-type structure (see figure 7.6).

Figure 7.6. The intermediate phase of PbSe-II refined in the GeS-type structure is shown here. The dotted line is the experimental diffraction pattern, with the solid line of the calculated pattern overlaying this. Under these two patterns, the difference is shown as a dashed line, and the positions of reflections are indicated by tick marks.

	$a(\text{Å})$	$b(\text{Å})$	$b(\text{Å})$	$u_{Ge,Pb}$	$v_{Ge,Pb}$	$u_{S,Se}$	$v_{S,Se}$
GeS	4.3	10.44	3.65	0.106	0.121	0.503	-0.148
PbSe as GeS	4.147	11.314	4.318	0.4875	0.6272	0.0176	0.3711

Table 7.2. Structural parameters for GeS and from the refinement of PbSe-II in the GeS-type structure. The symmetry used was *Pbnm* with Pb and Se atoms on the $4(c)$, $(u, v, \frac{1}{4})$, sites.

As can be seen in figure 7.6, the fit to the experimentally observed data is slightly better than that obtained with PbSe-II adopting the TlI-type structure. The shoulder on the main peak has now been accounted for by the (101) reflection, which was completely missed by the TlI-type structure assignment. This level of resolution would not have been possible without the increased amount of data collected by the image-plate.

Preferred orientation was a problem, with the main peak at about 9° showing the effects most strongly. This preferred orientation can also be seen in the 2D image-plate

pattern collected for this sample in figure 7.7. The cutoff limits of intensity have been altered to highlight the variation of intensity around the affected rings. These intensity variations may be used to evaluate the preferred orientation direction [38], but this analysis was not performed due to lack of time.
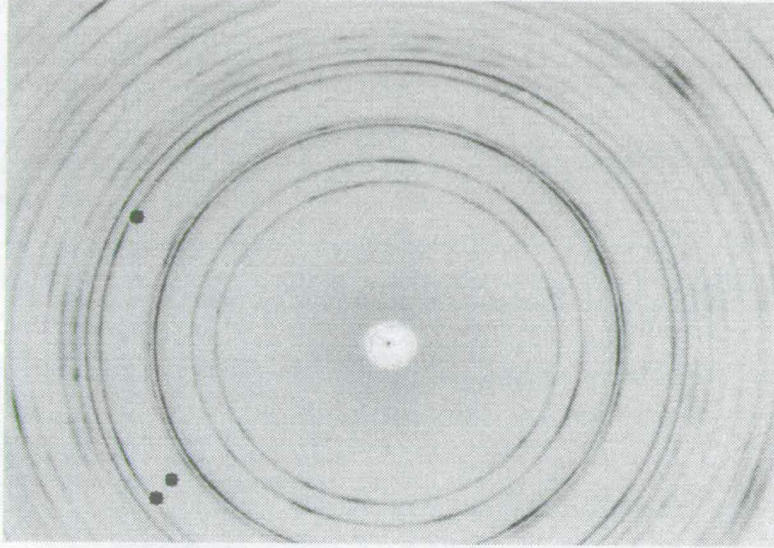

Figure 7.7. The preferred orientation effects in PbSe-II at 77(2)kbar can be seen clearly when the limits of maximum and minimum displayed intensity are altered.

7.4.2 Structural modifications in PbS and PbTe

The structure of PbS-II and PbTe-II has previously been proposed to be the orthorhombic GeS-type structure [114, 115], for both compounds. However, inspection of any high pressure pattern of either material shows that this is not the case. There appear to be many more reflections present than are predicted for the orthorhombic lattice. To illustrate this, the strongest reflections in the diffraction pattern for PbS-II, collected at 33(1)kbar were used to compute approximate lattice parameters within the GeS-type structure. As can be seen from figure 7.8, the positions of these calculated reflections do not match the number or positions of some collected maxima. The same conclusion may be drawn for the structure of PbTe-II. This diffraction pattern is so unlike GeS, it is difficult to even approximate initial trial lattice parameters, so the experimental

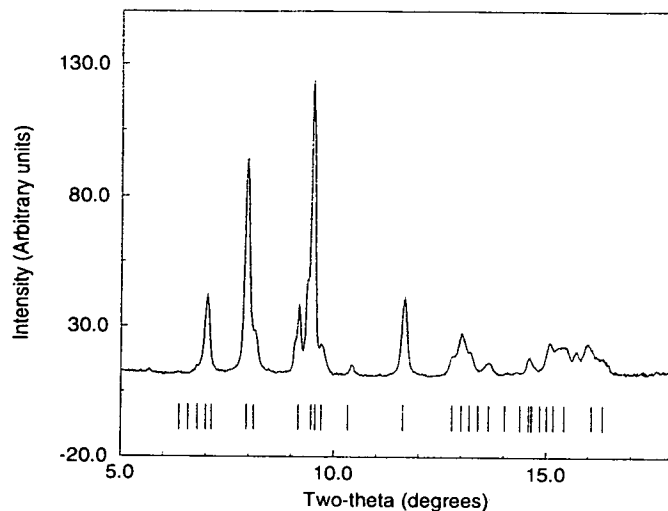diffraction pattern is just shown at 107(5)kbar in figure 7.9.

Figure 7.8. The intermediate phase of PbS shown here does not exhibit all of the characteristics of the orthorhombic GeS-type structure, indicated by the position of reflections calculated using the strongest peaks in PbS.

Doubling of the GeS-type structure in one of the three possible directions was first assumed for PbS-II and PbTe-II, but this did not account for the extinction of peaks below about 5°. Both diffraction patterns exhibit similar aspects, such as the grouping of three reflections at about 9° (also seen in PbSe-II) and the two peaks at about 10.5° and 12° in PbS-II, and 10° and 11° in PbTe-II. This suggests that the structures contain similar inter-planar spacings, but does not necessarily imply that the structures are isomorphic.

By computing equal contact distance in the orthorhombic GeS-type structure, a primitive monoclinic cell was found with spacegroup $P2_1m$ and Z=2. The approximate lattice parameters of this cell were $a \approx 8.5$Å $b \approx 6$Å $c \approx 4.3$Å and $\gamma \approx 27°$. The position of reflections generated by this structure were mapped to the experimentally observed peaks in diffraction patterns of both PbS-II and PbTe-II, but again, not all observed

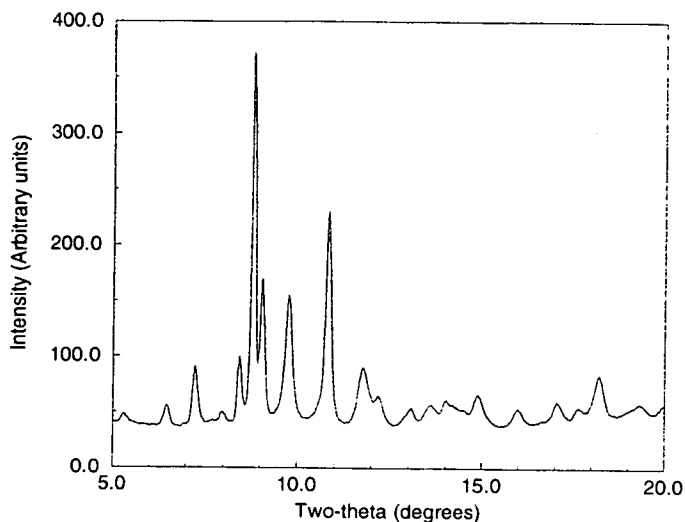reflections were accounted for by this monoclinic cell.

Figure 7.9. The diffraction pattern of PbTe-II, shown here at 107(5)kbar, is very complex, showing signs of severe peak overlap, indicating a structure with low symmetry.

Since modifying the orthorhombic GeS-type structure for both PbSe-II and PbTe-II did not generate reflections at the experimentally observed positions, DICVOL was used to index possible trial lattice parameters. The results obtained from DICVOL were first tested against a diffraction pattern obtained for PbSe-II at 53(3)kbar. This pattern refined well as the GeS-type structure, with lattice parameters a=4.14(1)Å, b=11.31(1)Å, and c=4.32(1)Å. Indexing the first 17 peaks from this pattern using DICVOL produced lattice parameters a=4.15Å b=4.32Å and c=11.31Å. From these corresponding results, DICVOL was shown to be a reliable indexing method.

Diffraction patterns for PbS-II and PbTe-II to use in the structural analysis were then chosen. The "cleanest"[†] diffraction pattern of PbS-II was taken at 68(3)kbar, and for PbTe-II at 72(4)kbar. Positions of the first 20 diffraction peaks in each pattern were located, using a peak-fitting algorithm within the PLATYPUS program, detailed

---

[†]Due to difficulty in accurately aligning the sample along the boresight of the pinhole, the gasket holding the sample occasionally contributed to the diffraction pattern. These reflections may have obscured small reflections from the sample diffraction pattern, so it was imperative to only use diffraction patterns with the minimum amount of gasket lines present for structural analysis.

in section 2.1.2.

Starting DICVOL with only the strongest peaks, and then adding in the weaker peaks (as well as reflections on the side of main peaks) on successive computational runs, trial structures which were not consistently generated could be eliminated, leaving only the most stable trial structures. Lattice parameters for some promising trial structures are given for PbS-II in Table 7.3. Many monoclinic cells were also indexed for PbTe-II using DICVOL, but due to the increased grouping of reflections, the accuracy and reliability of the results obtained was reduced. The diffraction pattern of PbTe-II was actually so complex, that all individual reflections could not be resolved. Since the diffraction patterns of PbS-II appeared to be less complex, most effort was given to the analysis of this structure. From the fact that similar inter-planar separations are indicated in the diffraction patterns of PbS-II and PbTe-II, solving the structure for one may speed the solution of the other.

$a(\text{Å})$	$b(\text{Å})$	$c(\text{Å})$	$\alpha(°)$	$\beta(°)$	$\gamma(°)$	Z
8.97	4.62	7.05	90	91.53	90	6
7.16	8.80	6.24	90	91.74	90	8
6.83	6.44	5.55	90	110.5	90	8

Table 7.3. The most promising trial structures generated from DICVOL are given here. The number of formula units, Z, for each trial cell was determined from an approximate density given in the input file, and the computed unit cell volume.

Trial cells were eliminated without going through the full Rietveld refinement methods (which are unstable for initial trial models) by employing the Monte-Carlo technique, as outlined in section 3.1.3. Indexed cells and approximate numbers of constituent atoms (calculated from the volume of the cells and assumed atomic radii for Pb, S and Te) were used, together with P2 symmetry (to allow the maximum number of degrees of freedom to be explored) in the Monte-Carlo program. The program was then set in operation for several thousand MC cycles for each initially indexed structure. However, no trial cells produced stable atomic locations, indicating that the

wrong lattices were being used. One fact obtained from the failed indexing result was that only monoclinic or triclinic cells were favoured, indicating that the structures for PbSe-II and PbTe-II are indeed complex.

7.5 Conclusions

Despite inconclusive results on the structures of PbS-II and PbTe-II, the present series of experiments has supplied some answers to old questions. The structure of PbSe-II has been shown to be similar to that of the GeS-type structure and not the TlI-type structure, from the observation of reflections which are systematically absent in the TlI-type structure. This calls into question results of previous studies [117], which proposed the TlI-type structure for PbSe-II.

After lengthy analysis, the structures of both PbS-II and PbTe-II were both found not to be the GeS-type structure. Although no firm structural refinement was possible with the data collected here, it is obvious that a more complex structure type is adopted by both materials. Severe overlapping of reflections will hinder any efforts to correctly index structural parameters, which is the main reason why all attempts to index both PbS-II and PbTe-II under pressure have failed. However, diffraction patterns displaying this degree of complexity imply either a monoclinic or triclinic structure is adopted, which has been verified by the results of the indexing package DICVOL. Using the group V elements Sb and Bi as a source of reference, it has been shown that both these elements may adopt a monoclinic distortion of a previously assumed tetragonal structure under high pressure. Also, under conditions of high pressure and high temperature, Sb has been indexed to adopt a monoclinic cell, which has lattice parameters similar to those of a monoclinic distortion of the GeS-type structure[‡]. This elemental monoclinic indexing may prove to be a possible model for a more detailed

---

[‡]Ref. [112] has indexed lattice parameters $a = 11.503$Å $b = 3.914$Å $c = 4.452$Å and $\beta = 85.35°$ for Sb at 115kbar and 150°C. This corresponds to the equivalent spacegroup setting of *Pnma* for the GeS-type structure, with a monoclinic distortion.

study of the structures of both PbS-II and PbTe-II.

In order to improve the chance of correctly indexing and refining a structure for the intermediate phases of PbS and PbTe, x-ray powder diffraction experiments will need to be performed with a longer wavelength. This will have the effect of separating closely spaced reflections, allowing more accurate indexing. This would be most ideally done on a lab source, as available time on central facilities such as the Daresbury synchrotron source, is under great demand.

An understanding of the structures which each of these three group IV-VI compounds adopt has been studied [5] at ambient pressure and temperature. In this study, the degree of ionicity (r_σ) present in the bonding configuration for each compound was computed from the difference in energy of the p orbitals on each atom type, and the degree of covalency (r_π) from the average $s - p$ splitting for each atomic species. The position of each IV-VI compound was then plotted on a graph with r_π^{-1} and r_σ as axes, which allowed clear stability boundaries separating the three structures that the (Ge,Sn,Pb)(S,Se,Te) compounds adopt[§] at room temperature and ambient pressure to be defined. From this analysis, the degree of covalency in the atomic bonds appears to be the influencing factor between the relative stability of the NaCl-type and GeS-type structures. By assuming a single critical value of r_π ($r_{\pi c} \approx 0.49$) which separates the NaCl-type and GeS-type structures, a relation was shown to exist between r_π and pressure [5], which allows a critical pressure, p_c, to be computed

$$p_c = - \left(\frac{3}{3.5} \right) B \frac{(r_\pi - r_{\pi c})}{r_\pi}, \tag{7.1}$$

where B is the bulk modulus. The critical pressures for the lead chalcogenides are compared against the experimentally observed transition pressures in Table 7.4.

As can be seen, the observed transition pressure for PbSe agrees very well with the

---

[§]SnTe and GeTe adopt a rhombohedral structure similar to Sb, Bi and As. PbS, PbSe, and PbTe adopt the NaCl-type structure, and GeS, GeSe, SnS and SnSe all adopt the same orthorhombic structure.

Compound	r_π	Critical pressure p_c	Experimentally observed P_T
PbS	0.5	11	26(3)
PbSe	0.56	42	40(4)
PbTe	0.59	49	58(6)

Table 7.4. The critical pressure separating the NaCl-type phase and GeS-type structure at room temperature is compared against the transition pressure experimentally observed to occur for PbX,(X=S,Se,Te).

theoretical critical pressure which separates the stability between the NaCl-type and GeS-type structures. However, for both PbS and PbTe, the experimentally observed transition pressure occurs beyond the computed critical pressure, even after experimental errors are accounted for. This simple comparison indicates that the phase transition from the NaCl-type structure occurring in PbS and PbTe may not lead to the GeS-type structure, which agrees with the present experimental observations. Unfortunately, this analysis does not give any clues as to the type of structure adopted by either PbS-II or PbTe-II. Since the degree of covalency was shown to drive the transition from the NaCl-type structure to the GeS-type structure, this suggests that the relative amount of ionicity present in the PbS and PbTe compounds is an important factor. Some interesting further work on these two compounds would be to study the electronic properties of the NaCl-type structure under decreasing lattice parameter. From the distribution of charge density in the unit cell, ionicity and covalency effects could be studied, perhaps supplying information on the type of structure adopted by PbS-II and PbTe-II beyond the first solid-solid structural transition.

Chapter 8

Discussion

The complexity of structures adopted (even by elemental substances) when placed under extreme pressures is proving to generally become greater, with the advent of increased imaging resolution afforded by image-plate techniques. Powder diffraction profiles showing small distortions from previously proposed high symmetry structures are becoming more obvious. This upturns the conventional school of thought that predicts atomic arrangements to become more ordered under high hydrostatic pressure, like conditions such as those created within diamond anvil cells.

Silicon, one of the most studied materials, is still showing remarkably intricate atomic arrangements under non-ambient conditions. The R8 phase, shown to exist upon depressurisation from the metallic β-tin phase in chapter 4, is the most complex structure adopted by a tetrahedral network of atoms. Five-fold ring formations are rarely seen in many materials, but it is most unusual to find a group IV element existing in such an arrangement. By following the structural changes under pressure, it has been possible to show likely transition routes from the high symmetry, body-centred cubic BC8 phase to the low symmetry, primitive rhombohedral R8 phase. This degree of resolution would not have been possible less than 10 years ago, and offers convincing reasons for re-examining presently accepted high pressure structures.

The computational work carried out in chapter 5 on the stability of high pressure

structures adopted by CuCl, represents the biggest full-potential computation ever undertaken. By confirming the stability of the SC16 phase between the ZnS-type and NaCl-type structures, the experimental work carried out by Hull and Keen [71] has been confirmed theoretically, and earlier speculation about the superconductivity of CuCl [81] has been put under question.

Despite the difficulties faced when analysing the high pressure diffraction patterns obtained from the group V elements and group IV-VI compounds, positive results can still be drawn. Enough experimental evidence was collected to show that the tetragonal structure assumed by both Sb and Bi under pressure is subject to a monoclinic-like distortion. The same can be said for the high pressure phase occurring between the NaCl-type and CsCl-type phases in the lead chalcogenides. The structure of PbSe-II was refined to be similar to that of the orthorhombic GeS-type structure, not the previously accepted TlI-type structure, and the structures of PbS-II and PbTe-II were shown to exhibit a much more complex atomic arrangement than those speculated by other research groups.

Although the work carried out in each preceding chapter may be taken separately, there is an underlying theme which binds each of them together, *viz* the commonality of structural adoption by elements and iso-electronic compounds under high pressure.

In chapters 4 and 5 the high pressure phases adopted by Si (group IV) and CuCl (group I-VII) were investigated. Here, there is an obvious link between the BC8 phase of Si and the binary-analogue SC16 phase of CuCl, as well as the face-centred cubic symmetry existing in the low pressure phases of each material. This structural symmetry can also be seen in chapters 6 and 7, between *all* the phases occurring in the group V elements Sb and Bi, and the group IV-VI compounds PbX, (X=Se,S,Te).

These similarities are predominantly due to the correspondence between electron valence states occurring in these iso-electronic materials. Physical limitations (*i.e.* altered packing densities caused by different atomic species in the unit-cell basis of a compound) will tend to distort the one-to-one equivalence between high pressure

structures, but the trend towards higher atomic co-ordination still follows the same symmetrical correspondence.

Due to the inevitable time constraints imposed on any course of postgraduate study, the work presented in this thesis has not been completed fully. Additional research is required in chapter 7 to solve the structures of PbS-II and PbTe-II, and further analysis on the effects of preferred orientation on diffraction patterns of Sb and Bi is needed.

The assignment of a monoclinic or triclinic Bravais lattice to PbS-II and PbTe-II is a valid statement, given the collected data, but this must be taken further by a full Rietveld refinement. Severe overlap of the reflections present in each phase was the dominant cause of the problems encountered. Preferred orientation effects were also found to be a problem. Although this makes the assignment of a structure more difficult, these effects will only affect the exact placement of atoms in the unit cell. The most important step in structure determination is finding the size and shape of the unit cell. From this, a possible spacegroup may be determined, reducing some of the effects of preferred orientation*.

One way to split the reflections in the diffraction patterns of PbS-II and PbTe-II would be to use a longer wavelength. This may lead to $\frac{\lambda}{3}$ scattering or x-ray absorption in the DAC using synchrotron radiation, but these problems would be overcome using a laboratory x-ray source. The scattered x-ray intensities from such a source may be reduced, but by using modern imaging and focusing techniques, diffraction patterns approaching the quality of those collected on synchrotron sources can be achieved. Lab sources also have the attraction of almost unlimited access, enabling large amounts of data to be collected and analysed.

Image-plate collection techniques can also be used to exploit the angular intensity variations seen on the 2D images to analyse preferred orientation effects in materials

---

*The two atomic species will impose maximum and minimum contact distances, making it easier to determine possible spacegroups. A knowledge of the structures either side of the intermediate phase may also help to place atoms, by requiring the intermediate phase to show some signs of distortion to either of the known structures.

such as the group V elements, Sb and Bi. Recent research [38] has shown that preferred orientation effects can be successfully accounted for by sampling the intensity distribution around the diffraction rings on the image-plates. One way to improve upon the results of structure analysis using the Rietveld method is to use the full 2D diffraction patterns obtainable from image-plate techniques, instead of the conventional 1D plots. Preferred orientation effects, anisotropic pressure variations within the sample, and even crystallite size would all fall out of such a calculation, from having this additional depth of information.

New analytical methods are helping to solve the crystalline arrangement of atoms from powder diffraction profiles. Among the most promising are those involving brute force to minimise the differences between computed and experimental diffraction patterns. With the advent of more powerful computers, such techniques as the Monte-Carlo method described in chapter 3, are proving to be very successful. Initial tests are very encouraging, but although these methods may allow a "run it and leave it" type of structure solution, this dangerous situation is to be discouraged. Although an automatic technique may present the most likely solution from a finite number of possibilities, this does not necessarily mean it is the *actual* structure adopted by the material. Similar methods are also being developed which minimise the inter-atomic potentials created by arrangements of atoms in a box. Energy minimisation techniques have proven successful for large organic structures, and may lead to more generic methods which can be applied to small scale inorganic materials.

Powder diffraction x-ray experimentation is enjoying an increase of interest from research groups in the high pressure field. For this reason, the results of all these studies must be linked to the electronic and physical properties of the bulk solid. Recent experiments [124] and analysis on the reliability of powder diffraction as a means to investigate the bulk properties of crystals is providing this missing link. By growing crystallites (nanostructures) of various sizes, the structural properties of Si, CdSe and InP were investigated, showing that elevated transformation pressures were obtained

when compared to experiments using bulk crystals of the same material. This has wide ranging implications on the increasingly expanding powder diffraction community.

Image-plate techniques for collecting x-ray powder diffraction data have so far proven to be very reliable and accurate, especially when used in conjunction with synchrotron radiation. The next step towards improvement will probably be in the form of x-ray sensitive CCD cameras. These arrays of detectors will not only allow 2D images to be collected, but may also be used in *real-time* experiments, offering direct observation of materials undergoing phase transitions, which is presently unobtainable.

Alongside advances in data collection techniques, improvements in sources of x-rays are being made. The new third generation synchrotron source at the ESRF combines specialised optics, such as adaptive mirrors and nitrogen cooled Si monochromators, with beam intensities of the order 200mA [125]. This performance has been made possible by using radiation emitted by wigglers and undulators, rather than just being radiated from the storage electron beam itself. Since the intensity of scattered x-rays is proportional to the square of the number of electrons, x-ray experiments involving materials with low atomic numbers suffer greatly from reduced intensities. This problem is only exaggerated by the necessarily small sample volumes ($\approx 100 \mu m^3$). The possible benefits from such a bright source as the ESRF, which can be focused into a small spot size for high pressure work using DAC's, are thus especially important for experiments studying materials such as hydrogen.

Bibliography

[1] M. Baleva, L. Bozukov, and M. Momtchilova. *J. Phys: Condens. Matter*, 4:4633, 1992.

[2] W. Kohn and L. J. Sham. *Phys. Rev. A*, 140:1133, 1965.

[3] J. C. Phillips. *Rev. Mod. Phys.*, 42:317, 1970.

[4] J. A. Van Vechten. *Phys. Rev. B*, 7:1479, 1973.

[5] P. B. Litlewood. *J. Phys. C*, 13:4855, 1980.

[6] D. M. Adams. *Inorganic Solids : An introduction to concept in solid state structural chemistry*. John Wiley and Sons., 1981.

[7] C. Kittel. *Introduction to Solid State Physics*. John Wiley and Sons, 1976.

[8] M. M. Woolfson. *Introduction to x-ray crystallography*. Cambridge University Press, 1970.

[9] D. McKie and C. McKie. *Essentials of crystallography*. Blackwell Scientific Publications, 1992.

[10] Y. Fujii, K. Hose, Y. Ohishi, H. Fujihisa, N. Hamaya, K. Takemura, O. Shimomura, T. Kikegawa, Y. Ameniya, and T. Matsushita. *Phys. Rev. Lett.*, 63:536, 1989.

[11] R. J. Nelmes, P. D. Hatton, M. I. McMahon, R. O. Piltz, J. Crain, R. J. Cernik, and G. Bushnell-Wye. *Rev. Sci. Instrum.*, 63:1039, 1992.

[12] R. O. Piltz, M. I. McMahon, J. Crain, P. D. Hatton, R. J. Nelmes, R. J. Cernik, and G. Bushnell-Wye. *Rev. Sci. Instrum.*, 63:700, 1992.

[13] R. J. Elliot and A. F. Gibson. *An Introduction to Solid State Physics*. MacMillan, 1974.

[14] A. Jayaraman. *Rev Modern Phys.*, 55:65, 1983.

[15] L. Merrill and W. A. Bassett. *Rev. Sci. Instrum.*, 45:290, 1974.

[16] D. Schiferl. *Rev. Sci. Instrum.*, 48:24, 1977.

[17] R. Keller and W. B. Holzapfel. *Rev. Sci. Instrum.*, 48:517, 1977.

[18] W. F. Sherman and A. A. Stadtmuller. *Experimental techniques in high-pressure research*. John Wiley & Sons ltd., 1989.

[19] G. J. Piermarini, S. Block, and J. S. Barnett. *J. Appl. Phys.*, 44:5377, 1973.

[20] I. Fujishiro, G. J. Piermarini, S. Block, and R. G. Munro. In C. M. Backman, T. Johannisson, and L. Tegner, editors, *High pressure in research and industry*, volume 63, page 700. 8th AIRAPT, (ISBN, Sweden), 1982.

[21] D. L. Decker. *J. Appl. Phys.*, 37:5012, 1966.

[22] D. L. Decker. *J. Appl. Phys.*, 42:3239, 1971.

[23] R. A. Noack and W. B. Holzapfel. page 748. 6th AIRAPT, Plenum Press, New York, 1978.

[24] D. Louer and M. Louer. *J. Appl. Cryst.*, 5:271, 1972.

[25] D. Louer and R. Vargas. *J. Appl. Cryst.*, 15:542, 1982.

[26] A. Boultif and D. Louer. *J. Appl. Cryst.*, 24:987, 1991.

[27] W. Paszkowicz. *Powder Diffr.*, 9:136–142, 1994.

[28] W. Paszkowicz. *EPDIC IV conference proceedings*, 1995.

[29] P.M. De Wolff. *J. Appl. Cryst.*, 1:108, 1968.

[30] G. S. Smith and R. L. Snyder. *J. Appl. Cryst.*, 12:60, 1979.

[31] H. M.. Rietveld. *J. Appl. Cryst.*, 2:65, 1969.

[32] G. Malmaros and J. O. Thomas. *J. Appl. Cryst.*, 10:7–11, 1977.

[33] D. B. Wiles and R. A. Young. *J. Appl. Cryst.*, 14:149, 1981.

[34] P. J. Bendall, A. N. Fitch, and B. E. F. Bender. *J. Appl. Cryst.*, 16:164, 1983.

[35] R. J. Hill. *J. Appl. Cryst.*, 25:589, 1992.

[36] A. Albinati and B. T. Willis. *J. Appl. Cryst.*, 15:361, 1982.

[37] E. R. Pike and J. Ladell. *Acta. Crysta.*, 14:53, 1961.

[38] N. Wright. PhD thesis, Edinburgh University, 1994.

[39] G. Cagliotti, A. Paoletti, and F. P. Ricci. *Nucl. Instrum.*, 3:223, 1958.

[40] H. Fichtner-Schmittler and M. L. Menz. *Krist. Tech.*, 13:569, 1978.

[41] C. P. Khattak and D. E. Cox. *J. Appl. Cryst.*, 10:405, 1977.

[42] N. Metropolis, A. W. Rosenbluth, M. N. Rosenbluth, A. H. Teller, and E. Teller. *J. Chem. Phys.*, 21:1087, 1953.

[43] M. W. Deem and J. M. Newsam. *Nature*, 342:260, 1989.

[44] K. D. M. Harris, M. J. Tremayne, P. Lightfoot, and P. G. Bruce. *J. Amer. Chem. Soc.*, 116:3545, 1994.

[45] P. P. Ewald. *Ann. Physik*, 64:253, 1921.

[46] J. C. Slater. *Insulators, semiconductors and metals.* McGraw-Hill, 1967.

[47] M. Gell-Mann and K. Brueckner. *Phys. Rev.*, 106:364, 1957.

[48] L. Hedin and B. Lundqvist. *J. Phys. C*, 4:2064, 1971.

[49] S. H. Vosko, L. Wilk, and M. Nusair. *Can. J. Phys.*, 58:1200, 1980.

[50] J. P. Perdew and A. Zunger. *Phys. Rev. B*, 23:5048, 1981.

[51] D. J. Chadi and M. L. Cohen. *Phys. Rev. B*, 8:5747, 1973.

[52] J. D. Joannopoulos and M. L. Cohen. *J. Phys. C*, 6:1572, 1973.

[53] H. J. Monkhorst and J. D. Pack. *Phys. Rev. B*, 13:5188, 1976.

[54] P. Blaha, K. Schwarz, and P. Sorantin. *Comp. Phys. Commun.*, 59:399, 1990.

[55] J. C. Slater. *Phys. Rev.*, 51:846, 1937.

[56] D. D. Koelling and G. O. Arbman. *J. Phys. C*, 5:2041, 1975.

[57] M. Weinert. *J. Math. Phys.*, 22:2433, 1981.

[58] J. C. Jamieson. *Science*, 139:762, 1963.

[59] H. Olijnyk, S. K. Sikka, and W. B. Holzapfel. *Phys. Lett.*, 103A:137, 1984.

[60] J. Z. Hu and I. L. Spain. *Solid State Commun.*, 51:263, 1984.

[61] R. H. Wentorf,Jr and J. S. Kaspar. *Science*, 139:338, 1963.

[62] J. S. Kaspar and S. M. Richards. *Acta Crystallogr.*, 17:752, 1964.

[63] R. Biswas, R. M. Martin, R. J. Needs, and O. H. Nielsen. *Phys. Rev. B*, 30:3210, 1984.

[64] A. Mujica and R. J. Needs. *Phys. Rev. B*, 48:17010, 1993.

[65] J. Crain, S. J. Clark, G. J. Ackland, M. C. Payne, V. Milman, P. D. Hatton, and B. J. Reid. *Phys. Rev. B*, 49:5329, 1994.

[66] R. O. Piltz, J. R. Maclean, S. J. Clark, G. J. Ackland, P. D. Hatton, and J. Crain. *Phys. Rev. B*, 52:4072, 1995.

[67] J. Crain, G. J. Ackland, J. R. Maclean, R. O. Piltz, P. D. Hatton, and G. S. Pawley. *Phys. Rev. B*, 50:13043, 1994.

[68] E. I. Tonkov. *High pressure phase transformations, v1 and v2.* Gordon and Breach Science Publishers, 1992.

[69] R. J. Nelmes, M. I. McMahon, N. G. Wright, D. R. Allan, and J. S. Loveday. *Phys. Rev. B*, 48:9883, 1993.

[70] J. Crain, R. O. Piltz, G. J. Ackland, S. J. Clark, M. C. Payne, V. Milman, J. S. Lin, P. D. Hatton, and Y. H. Nam. *Phys. Rev. B*, 50:8389, 1994.

[71] S. Hull and D. Keen. *Phys. Rev. B*, 50:5868, 1994.

[72] National Bureau of Standards. U.S. Department of commerce.

[73] J. Crain, R. O. Piltz, G. J. Ackland, S. J. Clark, M. C. Payne, V. Milman, J. S. Lin, P. D. Hatton, and Y. H Nam. *Phys. Rev. B*, 50:8389, 1994.

[74] J. Z. Hu, L. D. Merkel, C. S. Menomi, and I. L. Spain. *Phys. Rev. B*, 34:4679, 1986.

[75] J. Maclean, P. D. Hatton, J. Crain, R. O. Piltz, S. J. Clark, and R. J. Cernik. *Materials Science Forum*, 228-231:595-600, 1996.

[76] F. Birch. *Handbook of Physical constants, Geol. Soc. Am. Memoir*, 97:97-173, 1966.

[77] S. J. Clark, G. J. Ackland, and J. Crain. *Phys. Rev. B,* 52:15035, 1995.

[78] J. D. Joannopoulos and M. L. Cohen. In F. Sietz H. Ehrenreich and D. Turnbull, editors, *Solid State Physics: Advances in Research and Applications,* volume 31. (Academic, New York), 1976.

[79] R. Alben, D. Weaire, J. E. Smith, and M. H. Brodsky. *Phys. Rev. B,* 11:2271, 1975.

[80] S. Ves, D. Glötzel, M. Cardona, and H. Overhof. *Phys. Rev. B,* 24:3073, 1981.

[81] N. B. Brandt, S. V. Kuvshinnikov, H. P. Rusakov, and M. V. Semerov. *JETP Lett.,* 27:33, 1978.

[82] C. W. Chu, S. Early, T. H. Geballe, A. P. Rusakov, and R. E. Schwall. *J. Phys. C,* 8:L241, 1975.

[83] G. J. Piermarini, F. A. Mauer, S. Block, A. Jayaraman, T. H. Geballe, and G. W. Hull, Jr. *Solid State Comm.,* 32:275, 1979.

[84] H. C. Hsueh, J. R. Maclean, G. Y. Guo, M-H. Lee, S. J. Clark, G. J. Ackland, and J. Crain. *Phys. Rev. B,* 51:12216, 1995.

[85] G. Y. Guo, J. Crain, P. Blaha, and W. M. Temmerman. *Phys. Rev. B,* 47:4841, 1993.

[86] D. D. Koelling and B. N. Harmon. *J. Phys. c,* 10:3107, 1977.

[87] R. P. Feynman. *Phys. Rev.,* 56:340, 1939.

[88] F. D. Murnaghan. *Proc. Nat. Acad. Sci. USA,* 30:244, 1944.

[89] E. Rapoport and C. W. F. T. Pistorious. *Phys. Rev.,* 172:838, 1968.

[90] K. Reimann and St. Rübenacke. *Phys. Rev. B,* 40:11021, 1994.

[91] A. P. Rusakov, V. N. Kaukhin, and Yu. A. Lisovski. *Phys. Status Solidi B*, 71:K191, 1975.

[92] H. Müller, S. Ves, H. D. Hochheimer, and M. Cardona. *Phys. Rev. B*, 22:1052, 1980.

[93] B. Batlogg, J. P. Remeika, and R. G. Maines. *Solid State Commun.*, 38:83, 1980.

[94] S. S. Kabalkina, T. N. Kolobyanina, and L. F. Vereshchagin. *Zh. Eksper. i. Fiziki*, 58:486, 1970.

[95] T. N. Kobolyanina, S. S. Kabalkina, and L. F. Vereschchagin. *Zh. Eksper. i. Fiziki*, 55:164, 1968.

[96] L. F. Vereschchagin and S. S. Kabalkina. *High Temp.-High pressures*, 7:637, 1975.

[97] L. G. Khvostantsev and V. A. Sidorov. *Phys. Stat. Sol. a*, 32:389, 1984.

[98] D. Schiferl, D. T. Cromer, and J. C. Jamieson. *Acta Crystallogr.*, 37B:807, 1981.

[99] H. Iwasaki and T. Kikegawa. *Physica*, 139 and 140B:6259, 1986.

[100] T. N. Kobolyanina, S. S. Kabalkina, and L. F. Vereschchagin. *Zh. Eksper. i. Fiziki*, 59:1146, 1970.

[101] J. M. Duggan. *J. Phys. Chem. Solids*, 33:1267, 1972.

[102] K. Aoki, S. F. Ujiwara, and M. Kusakabe. *Solid State Commun.*, 45:161, 1983.

[103] R. M. Brugger, R. B. Bennion, and T. G. Worlton. *Phys. Lett*, 24A:714, 1967.

[104] J. H. Chen, H. Iwasaki, and T. Kikegawa. *High pressure research*, 15:143, 1996.

[105] A. Giardini and G. A. Samara. *J. Phys. Chem. Solids*, 26:1523, 1965.

[106] J. H. Chen, H. Iwasaki, and T. Kikegawa. *High Pressure Research*, 15:143, 1996.

[107] P. W. Bridgman. *Collected Experimental Papers*, volume V. Harvard University Press, 1964.

[108] S. S. Kabalkina, L. F. Vereshchagin, and V. P. Mylov. *Dokl. Akad. Nauk SSSR*, 152:585, 1963.

[109] R. M. Brugger, R. B. Bennion, and *et. al* T. G. Worlton. *Trans. Amer. Crystallogr. Assn.*, 5:141, 1969.

[110] V. K. Fedotov, V. A. Somenkov, and *et. al* S. Sh. Shil'shtein. *Fiz. Tverd. Tela*, 20:1088, 1978.

[111] J. Maclean, P. D. Hatton, R. O. Piltz, J. Crain, and R. J. Cernik. *Nucl. Instrum. Methods B*, 97:354–357, 1995.

[112] H. Iwasaki and T. Kikegawa. *Physica*, 139 and 140B:259, 1986.

[113] L. Klienman and D. M. Bylander. *Phys. Rev. Lett.*, 48:1425, 1982.

[114] A. N. Mariano and K. L. Chopra. *Appl. Phys. Lett.*, 10:282, 1967.

[115] Y. Fujii, K. Kitamura, A. Onodera, and Y. Yamada. *Solid State Communications*, 49:135, 1984.

[116] T. Chattopadhay, , A. Werner, and H. G. Von Schnering. *Mat. Res. Soc. Symp. Proc.*, 22:93, 1984.

[117] T. Chattopadhay, H. G. Von Schnering, W. A. Grosshaus, and W. B. Holzapfel. *Physica B+C*, 139:356, 1986.

[118] M. Baleva, I. Ivanov, and M. Momtchilova. *J. Phys: Condens. Matter*, 4:4645, 1992.

[119] M. Baleva, E. Mateeva, and M. Momtchilova. *J. Phys: Condens. Matter*, 4:8997, 1992.

[120] M. Baleva, E. Mateeva, M. Petrauskas, R. Tomasiunas, and R. Masteika. *J. Phys: Condens. Matter*, 4:9009, 1992.

[121] M. Wanatabe, M. Tokonami, and N. Morimoto. *Acta Crystallogr.*, A33:292, 1977.

[122] J. Buerger. In R. Smoluchowski, J. E. Meyers, and W. A. Weyl, editors, *Phase Transformation in solids*. Wiley, New York, 1951.

[123] A. Martín Pendás, V. Luaña, J. M. Recio, M. Flórez, E. Francisco, M. A. Blanco, and L. N. Kantorovich. *Phys. Rev. B*, 49:3066, 1994.

[124] S. H. Tolbert and A. P. Alvisatos. In J. F. Griffin, editor, *XVII Congress and General Assembly*, volume 1, pages C–542. International Union of Crystallography, IUCr, 1996.

[125] Y. Petroff. *Nucl. Instrum. Methods in Phys. Res.*, B97:505–508, 1995.